THE UNIVERSITY *of* EDINBURGH

Non-photochemical laser-induced nucleation (NPLIN): An experimental investigation of crystal nucleation.

Martin R. Ward

Doctor of Philosophy

University of Edinburgh

2014

Declaration

This thesis has been written entirely by me and has not previously been submitted in any previous application for a degree. The work detailed in this thesis is my own except where specific reference is made to the work of another.

Martin R. Ward

February 2014

Table of Contents

List of Figures vii
List of Tables x
Acknowledgements xi
Abstract xii
Lay summary xiv
List of acronyms and abbreviations xvi
List of publications xviii
Chapter 1: Introduction 1
1.1 The supersaturated state 2
1.1.1 Supersaturated solution 2
1.1.2 Metastability 3
1.1.3 Producing a supersaturated solution 4
1.2 Nucleation 5
1.2.1 Mechanisms of nucleation 5
1.3 Nucleation theories 6
1.3.1 Classical nucleation theory 6
1.3.2 Shortcomings of CNT 8
1.3.3 Improvements to CNT 9
1.3.4 The two-step model 10
1.3.5 Rayleigh laser scattering: evidence of solute clusters? 12
1.4 Non-photochemical laser-induced nucleation 16
1.4.1 Initial discovery 16
1.4.2 Polarization switching 20
1.4.3 Polarization switching for continuous-wave laser beam 24
1.4.4 Solution cluster structure 28
1.4.5 Simulations of NPLIN 29
1.4.6 Nucleation of bubbles 30
1.4.7 Polarization of pre-nucleated clusters 32
1.5 NPLIN in single component systems 36
1.5.1 Glacial acetic acid 37
1.5.2 Molten sodium chlorate 38
1.6 Thesis structure 41

Chapter 2: Non-photochemical laser-induced nucleation of potassium halides: effects of wavelength and temperature 43
2.1 Introduction 43
2.2 Experimental 44
2.3 Results 45
2.4 Discussion 49
2.4.1 Possible effect of sample heating 49
2.4.2 Effects of ion concentration 50
2.4.3 Model of experimental results 51
2.4.4 Mechanism for NPLIN 54
2.5 Conclusions 57
Chapter 3: Non-photochemical nucleation of potassium chloride induced by an evanescent wave 58
3.1 Introduction 58
3.2 Experimental 60
3.3 Results 62
3.4 Discussion 65
3.4.1 Sedimentation 65
3.4.2 Physical and surface effects 66
3.4.3 Effect of volume probed 68
3.5 Conclusions 69
Chapter 4: Rayleigh scattering in concentrated salt solutions: An investigation of solution structure 71
4.1 Introduction 71
4.2 Experimental 72
4.3 Results and Discussion 74
4.3.1 Sample screening 74
4.3.2 Qualitative estimation of particle size 77
4.3.3 Quantitative estimation of particle size 78
4.3.4 Nanosight™ analysis 86
4.3.5 What are the scattering objects? 88
4.3.6 Structure of the particles 89
4.3.7 Nanobubbles 92
4.3.8 Impurities 95
4.4 Conclusions 97

Chapter 5: Second-harmonic scattering in aqueous urea solutions: evidence for solute clusters? 99
5.1 Introduction 99
5.2 Experimental 100
5.3 Results 102
5.3.1 Concentration dependence 106
5.3.2 Source of SHS signal 108
5.4 Discussion 113
5.4.1 Solute clustering 113
5.4.2 Mechanism for SHS and particle structure 113
5.4.3 Possible role of impurity particles 115
5.4.4 Concentration dependence 116
5.5 Conclusions 117
Chapter 6: Final conclusions 118
References 122
Appendix A: Details of IP model 133
Appendix B: Calculation of image spatial resolution 135
Appendix C: Nanoparticle tracking analysis 136
C.1 Initialization 136
C.2 Results 137

List of Figures

Figure 1.1: Example solubility–supersolubility diagram

Figure 1.2: Illustration of different types of nucleation

Figure 1.3: Plot showing the classical free-energy barrier to nucleation

Figure 1.4: Comparison of the classical and two-step models of nucleation

Figure 1.5: Rayleigh scattering in solutions of KCl, sugar and ultrapure water

Figure 1.6: (a) Molecule of urea showing its most polarizable axis; and (b) Illustration of crystal habit of urea with crystallographic faces identified

Figure 1.7: Intensity, wavelength and polarization dependence of NPLIN in supersaturated aqueous urea solution

Figure 1.8: Illustration of the molecular packing in (a) α- and (b) γ-glycine polymorphs

Figure 1.9: Schematic diagram illustrating the principal of polarization switching for solutes of distinct polarizabilities

Figure 1.10: Summary of the effect of polarization on the outcome of nucleation of glycine reported by Sugiyama and co-workers

Figure 1.11: The probability of forming γ-glycine using linearly polarized light from under and supersaturated solution reported by Sugiyama and co-workers

Figure 1.12: Graphic summarizing the experimental observations of Sugiyama and co-workers explaining the polarization dependence of the crystal polymorph formed

Figure 1.13: Threshold laser pulse energy dependence on supersaturation for laser-induced bubble formation in carbonated water reported by Knott et al.

Figure 1.14: Experimental data from Alexander and Camp for NPLIN of KCl from supersaturated solution

Figure 1.15: Schematic representation of the classical free energy change a dielectric cluster would experience in an electric field

Figure 1.16: Experimental data of Alexander and Camp fitted using their polarization model of NPLIN

Figure 1.17: Peak power dependence of NPLIN of glacial acetic acid

Figure 1.18: Peak power dependence of nucleation reported for $NaClO_3$ from the supercooled melt

Figure 2.1: Plots of the NPLIN peak power density dependence of the fraction of samples nucleated from supersaturated aqueous solutions of KCl and KBr using (a) 532 nm and (b) 1064 nm laser pulses

Figure 2.2: Plot of the peak power dependence of NPLIN in supersaturated aqueous solutions of KCl at 23 and 33 °C

Figure 2.3: Schematic showing the hypothesized scheme for NPLIN for KCl and KBr

Figure 3.1: Diagram showing the evanescent wave generated by total internal reflection and the associated intensity profile

Figure 3.2: Schematic of (a) the dove prism cell used in experiment and (b) a photograph showing the elliptical profile of the field penetrating an aqueous droplet of rhodamine 610 dye

Figure 3.3: Cumulative fraction of KCl samples nucleated by ew-NPLIN

Figure 3.4: Examples of the location of crystals produced by ew-NPLIN in relation to the elliptical evanescent profile

Figure 4.1: Photograph of the general Rayleigh scattering experimental setup

Figure 4.2: Comparison of the scattering observed in (a) nearly saturated aqueous solutions of KCl and (b) NH_4NO_3

Figure 4.3: Plot of the time-lag dependence of the mean-squared displacement of a single particle in samples of 100 nm polystyrene beads and near saturated ($S = 0.95$) aqueous solutions of urea and glycine

Figure 4.4: Histogram plot of particle hydrodynamic diameter obtained by NTA in nearly saturated aqueous glycine solution

Figure 4.5: Histogram plot of particle hydrodynamic diameter obtained by NTA in nearly saturated aqueous urea solution

Figure 4.6: Histogram plot of particle hydrodynamic diameter obtained by NTA in nearly saturated aqueous NH_4NO_3 solution

Figure 4.7: Series of still tracking a flashing particle as it passes the laser beam in ammonium chloride solution

Figure 4.8: Comparison of the scattering pattern noted for some particles in (a) sample salt solutions and (b) an aqueous dispersion of polystyrene spheres

Figure 4.9: Schematic demonstrating the ion partitioning expected by Craig et al. acting to inhibit bubble coalescence in solution

Figure 5.1: Schematic showing the path used when scanning the sample cell through the focal volume in scanning microscopy experiments

Figure 5.2: Time-dependent photon count for second harmonic generation from crystalline potassium dihydrogen phosphate

Figure 5.3: Time-dependent photon counts for near saturated aqueous urea solutions and water

Figure 5.4: Time-dependent photon count for near saturated aqueous glycine solution

Figure 5.5: Concentration dependence of second harmonic scattering intensity from aqueous urea solutions

Figure 5.6: Image showing population of particles identified by Rayleigh scattering measurements in near saturated aqueous urea solution

Figure 5.7: (a) Integrated peak photon counts from series of consecutive traces whilst scanning solution droplet through the laser focal volume; and (b) trace obtained by summing all individual traces in (a)

Figure 5.8: (a) Comparison of SHS measured from urea solution and from a dispersion of $BaTiO_3$ particles. (b) shows two individual time-dependent traces identified in (a)

List of Tables

Table 1.1: Summary of the effects of different polarizations of light in polarization switching NPLIN in supersaturated aqueous glycine solution

Table 2.1: Sample labilities and threshold peak power densities obtained for NPLIN of KCl and KBr

Table 2.2: List of parameters used in evaluation of the modified classical nucleation model for the KCl and KBr NPLIN experimental data

Table 2.3: Comparison of experimental and model predicted values of sample lability and crystal–solution interfacial tension for KBr and KCl NPLIN

Table 3.1: Comparison of the sample lability and threshold power density values obtained for ew-NPLIN and regular NPLIN in supersaturated aqueous KCl solution

Table 4.1: Summary of the solute systems in which laser scattering experiments were performed

Table 4.2: Results of particle tracking analysis of simulated data

Table 4.3: Results of particle tracking analysis of dispersions of polystyrene spheres using different optical setups

Table 4.4: Results of particle tracking analysis of near saturated solutions of urea, glycine and ammonium nitrate using a ×50 magnification objective

Table 4.5: Summary of performance of Nanosight NTA compared to the present analysis in near saturated solutions of urea, glycine and ammonium nitrate

Table 4.6: Estimates of the rotational diffusion coefficient for a spherical particle in water

Table 4.7: Summary of the anion and cation combinations relevant to the systems investigated in the present work showing the combinations which inhibit or have no effect on bubble coalescence; based on the work of Craig et al.

Table 4.8: List of the sample solutions used in laser scattering experiments and whether or not they should inhibit bubble coalescence

Acknowledgements

Firstly, I would like to thank my supervisor Dr Andy Alexander for all of his help and advice over the last four years and for giving me the opportunity to work on this project in the first place. His enthusiasm for the project, and research in general, certainly rubbed off on me which provided additional motivation during the project. I would also like to thank my second supervisor Dr Philip Camp for the help and advice he has provided.

I would also like to take this chance to thank Dr Andy Ward and Dr Stan Botchway for their help and advice during experiments carried out at the Central Laser Facility at Harwell. Without their help the work discussed in Chapter 5 certainly could not have been carried out, and so I am very grateful to them.

Lastly, but in no ways least, I would also like to extend a huge thank you to three important ladies; Carol, Lynsey and Adele. Each of you has given me so much support and encouragement over the past 4 years and an increasing amount over the past few months. Without this support I would not have been in a position to undertake my PhD studies, let alone produce this thesis. Thank you very much.

Abstract

NPLIN was studied in supersaturated solutions ($S = 1.06$) of potassium chloride (KCl) and bromide (KBr). The fraction of samples nucleated (f) follows a nonlinear dependence on peak power density that approaches $f = 1$ at higher incident powers. It is shown that a lower threshold power is required for nucleation using 532 nm laser pulses than at 1064 nm, and that a higher fraction of samples nucleate when exposed to 532 nm pulses at a given laser power. Comparison with KCl shows higher fractions of KBr samples nucleate with lower threshold values at both wavelengths. Samples of KCl of equal supersaturation at two different temperatures (23 and 33 °C) exposed to 1064 nm pulses show that those at 33 °C are significantly more labile to nucleation. The ratio of samples nucleated at 33 °C compared to those at 23 °C was 2.11 ± 0.47. A classical nucleation model based on activation of subcritical solute clusters accounts remarkably well for the experimental data and provides phenomological values of the crystal–solution interfacial tension (γ) at 23 °C for KCl and KBr of 5.283 and 4.817 mJ m^{-2}. At 33 °C, the model yields a best-fit value of $\gamma = 5.429$ mJ m^{-2} for KCl. As an extension of this work the use of an evanescent wave (ew) generated by total internal reflection was investigated as a method to cause nucleation in supersaturated KCl solution. Evanescent wave NPLIN (ew-NPLIN) was shown to cause nucleation. The results showed a higher laser-power threshold required for nucleation and sample lability greater than that of bulk NPLIN.

In a second approach to understanding NPLIN, the structures of concentrated solutions were probed by a series of laser scattering experiments. Evidence showing populations of particles in solution was provided by Rayleigh laser scattering (RLS) experiments. Scattering in solutions prepared to be nearly saturated ($S = 0.95$) was observed using a low magnification (×10) microscope objective; almost all solutions showed the presence of scattering objects moving freely in solution. For those that showed no particles, it was noted that the solutions were typically of higher solute concentration (> 11 mol% solute). Ammonium nitrate solution showed no particles using ×10 magnification, however particles were identified when higher magnification was used (×50 and ×100). Video footage of the Rayleigh scattering observed in aqueous solutions of glycine, urea and ammonium nitrate obtained using

×50 magnification were analysed using a custom nanoparticle tracking software. The results showed a population of particles in aqueous urea and glycine solutions with particle concentrations of the order 10^8 particles cm^{-3} and mean hydrodynamic diameter of approximately 267 ± 1 and 173 ± 2 nm respectively. Not enough particles were identified in ammonium nitrate solution to complete the tracking analysis; however a fluctuating background scatter suggested a population of particles with sizes below the limit of resolution of the optical system.

Using aqueous urea solution as a model system the structure of the particles identified in solution was investigated using scanning microscopy. The second-harmonic scattering (SHS) signal measured in concentrated aqueous urea solution was measured as a function of solution concentration (C) over a range of saturation conditions from undersaturated (S = 0.15) to supersaturated (S = 1.86). The results show a non-linear increase in SHS signal with local maxima near S = 0.95 and 1.75 suggesting a change in solution structure near these points. Rayleigh scattering images indicate the presence of particles in nearly saturated (S = 0.95) urea solutions. Time-dependent SHS measurements indicate that signals originate from individual events encountered during scanning of the sample through the focal volume of the probe laser, consistent with second harmonic generation (SHG) from particles. SHG from aqueous dispersions of barium titanate ($BaTiO_3$) nanoparticles with diameters < 200 nm, showed signals ~20 times larger than urea solutions. The results suggest the existence of a population of semi-ordered clusters of urea that changes with solution concentration.

Lay summary

Although the use of crystals and the process of crystallization are ubiquitous in daily life, the events leading up to the formation of a solid from the solution phase, i.e., crystal nucleation remain a mystery. The lack of details surrounding nucleation is due to the very nature of nucleation itself; it occurs randomly in time and position. If nucleation could be localised to occur at a certain location at a certain time this would then allow the event to be studied directly.

In this Thesis a technique called non-photochemical laser-induced nucleation (NPLIN) has been used to localise nucleation to occur within a small volume of sample solution (~0.1 cm^3) and a short window of time (~10^{-9} seconds). NPLIN uses low power laser pulses to cause nucleation in highly concentrated solutions. NPLIN was studied in aqueous solutions of potassium chloride (KCl) and potassium bromide (KBr) using different wavelengths of laser light. The results show that samples are more easily nucleated using 532 nm laser pulses compared to 1064 nm pulses. In addition, under identical conditions KBr samples were always more likely to nucleate than KCl samples. The effect of temperature was also investigated with samples at 33 °C were found to be significantly more likely to nucleate than those at 23 °C. A model has been formulated that has been shown to account incredibly well for the experimental observations.

Although the typical NPLIN method localises nucleation to a small volume of solution, the expected length scales involved in nucleation are magnitudes of order smaller (~ nanoscale), therefore it would be beneficial to impose a finer degree of spatial control over nucleation. This was investigated by using an evanescent wave to initiate nucleation via NPLIN. The evanescent wave can be thought of as a tunnelling wave that penetrates the surface a short distance ($\lesssim$100 nm) on which it reflects. Evanescent wave NPLIN (ew-NPLIN) was successfully demonstrated and the laser power dependence studied.

Current theory in the area supports the idea that nucleation occurs within randomly arranged solute clusters in solution; however, experimental evidence supporting this idea is limited in the literature. A range of sample solution types were tested using a Rayleigh laser scattering (RLS) experiment that clearly showed populations of particles that move freely through solution. The recorded scattering

was analysed from which estimates of the particle concentration (~10^8 cm^{-3}) and particle diameter in urea (~267 nm) and glycine (~173 nm) solutions were made.

A limitation of RLS is that although particles are identified, it provides no information of the particle composition or structure. Assuming that the particles are solute clusters, a key question is to establish whether they have any internal structure. Taking urea as a model system it is known that only one solid form exists, therefore if the particles found in urea solution are crystalline then the structure should be that of the known crystal form. Crystalline urea is in a special group of crystals that undergo second harmonic generation (SHG), this is a process that doubles the frequency of incident light. A series of aqueous urea solutions were tested for SHG as a function of concentration. The results show a non-linear increase in second harmonic scattering (SHS) signal with concentration with local maxima near the point of saturation and in the supersaturated region which suggest a change in solution structure near these points. It was then established that the signal measured in urea solutions is consistent with SHG from particles encountered during scanning of the sample through the laser beam. The results suggest a population of semi-ordered clusters of urea that changes with concentration.

List of acronyms and abbreviations

RLS	Rayleigh laser scattering
CNT	Classical nucleation theory
2SM	Two-step nucleation model
SPC	Surface property corrected model
MD	Molecular dynamics
DIT	Diffuse interface theory
EMLD-DNT	Extended modified liquid drop-dynamical nucleation theory
SGT	Square gradient theory
DFT	Density functional theory
DLS	Dynamic light scattering
NTA	Nanoparticle tracking analysis
SAXS	Small-angle X-ray scattering
NPLIN	Non-photochemical laser-induced nucleation
HEWL	Hen egg-white lysozyme
CPL	Circularly polarized light
LPL	Linearly polarized light
CW	Continuous-wave
SANS	Small-angle neutron scattering
OKE	Optical Kerr effect mechanism
IP	Isotropic polarization mechanism
FWHM	Full-width at half maximum
GAA	Glacial acetic acid
TIR	Total internal reflection
ew-NPLIN	Evanescent wave-NPLIN
Nd^{3+}:YAG	Neodymium yttrium aluminium garnet (laser)
NA	Numerical aperture
CCD	Charge-coupled device (camera)
MSD	Mean squared displacement (2-dimensions)
SPM	Solute partitioning model
PTFE	Poly(tetrafluoroethylene)

HPLC	High-performance liquid chromatography
SEM	Scanning electron microscopy
XRF	X-ray fluorescence spectroscopy
SHG	Second harmonic generation
SHS	Second harmonic scattering
HRS	Hyper-Rayleigh scattering
TCSPC	Time-correlated single photon counting
SERS	Surface-enhanced Raman scattering

List of publications

This list contains the peer-reviewed publications produced during my PhD. I highlight the two papers at the end of the list; *Nonphotochemical laser-induced nucleation of potassium halides: Effects of wavelength and temperature*; and *Second-harmonic scattering in aqueous urea solutions: evidence for solute clusters?* These publications form the basis of Chapters 2 and 5, respectively in this Thesis. A PDF version of the papers listed here are attached electronically (CD-ROM).

Ward, M. R.; Copeland, G. W.; Alexander, A. J. *Chemical Communications* **2010**, *46*, 7634. Enantiomorphic symmetry breaking in crystallization of molten sodium chlorate. doi:10.1039/c0cc02563a

Ward, M. R.; Copeland, G. W.; Alexander, A. J. *Journal of Chemical Physics* **2011**, *135*, 114508. Chiral hide-and-seek: Retention of enantiomorphism in laser-induced nucleation of molten sodium chlorate. doi:10.1063/1.3637946

Ward, M. R.; McHugh, S.; Alexander, A. J. *Physical Chemistry Chemical Physics* **2012**, *14*, 90. Non-photochemical laser-induced nucleation of supercooled glacial acetic acid. doi:10.1039/c1cp22774b

Ward, M.R.; Alexander, A. J. *Crystal Growth & Design* **2012**, *12*, 4554. Nonphotochemical laser-induced nucleation of potassium halides: effects of wavelength and temperature. doi:10.1021/cg300750c

Ward, M. R.; Botchway, S. W.; Ward, A. D.; Alexander, A. J. *Faraday Discussions* **2013**, *167*, 441. Second-harmonic scattering in aqueous urea solutions: evidence for solute clusters? doi:10.1039/c3fd00089c

Chapter 1: Introduction

Crystallization is a process that is exploited daily on a huge scale in research, i.e. the preparation of single crystals for structural analysis and in industry as an efficient means of product separation and purification. In contrast to its significance, a full understanding of the mechanism of crystallization is yet to be achieved. The complex process of crystallization can be considered the result of 2 distinct events; crystal nucleation proceeded by crystal growth. Of these two steps, much less is known about nucleation i.e., the step that sees the first formation of a crystalline nucleus from the parent phase. The nucleation step is thought to be particularly significant for the case of crystallization of polymorphic materials.

Methods of crystallization employed to this day are often based on empirical observations and a certain degree of trial and error. A greater understanding of nucleation, and crystallization in general, would allow the design of improved and specific methodologies for crystallization of desired materials and crystal forms. This notion has particular relevance to the crystallization of pharmaceutical materials, which typically are polymorphic (e.g., acetaminophen) and where a specific crystal form is required. Furthermore, a complete understanding of the mechanism behind crystal nucleation may allow routine crystallization of materials that are difficult to crystallize using current methodologies.

Currently, the only theoretical description of crystal nucleation is provided by classical nucleation theory (CNT). CNT has been shown to be unreliable at best in its description of this phase transition. Recently the two-step nucleation mechanism (2SM) has been suggested as a more realistic description of crystal nucleation; however, a lack of direct experimental evidence has hindered the development of a formal theory of 2SM. Crystal nucleation is extremely challenging to study directly due to the stochastic nature of the process. The recent discovery of non-photochemical laser-induced nucleation (NPLIN) has been shown to exert an unprecedented degree of spatial and temporal control over nucleation and has been identified as an ideal tool for direct and *in situ* studies of crystal nucleation. It is

hoped that such studies will provide data that will in turn be used to provide a full theoretical description of crystal nucleation.

The following Sections in this Chapter will introduce background contextual information on nucleation theory, the use of laser scattering techniques to investigate solution structure and non-photochemical laser-induced nucleation (NPLIN). More specific introductory information is provided at the start of Chapters 2 to 5.

1.1 The supersaturated state

1.1.1 Supersaturated solution

Solutions can be classed as undersaturated, saturated or supersaturated depending on the amount of dissolved solute in the solution. At a given temperature, there is a maximum amount of solute that will freely dissolve into solution; this concentration is equal to the solubility of the solute and produces a saturated solution at that temperature. In other words, for a saturated solution, the solid is in thermodynamic equilibrium with the solution at a given temperature.

It is known that the driving force for crystallization processes from solution is the degree of supersaturation, *S*.[1] For this reason it is important to be able to quantify how supersaturated a solution of interest is. This can be quantified in terms of the absolute solute concentration (c) and the saturation concentration (c_0). There are several definitions that may be used, including the concentration driving force (Δc), the supersaturation ratio (S), and the relative supersaturation (σ). Expressions for these quantities are shown below[2]

$$\Delta c = c - c_0, \tag{1.1}$$

$$S = \frac{c}{c_0}, \tag{1.2}$$

$$\sigma = \frac{\Delta c}{c_0} = S - 1. \tag{1.3}$$

In this thesis the supersaturation ratio, S, is the favoured definition. In order to facilitate straightforward comparison between the works of others, the unit of concentration used here is grams of solute (anhydrous) per gram of solvent. Using conventional units such as molarity, M, can be problematic when it comes to

comparing data with other sources as this quantity relies upon accurate and common values of solution density.

1.1.2 Metastability

Undersaturated and saturated solutions are stable and can be stored indefinitely. In contrast, supersaturated solutions contain more solute than is thermodynamically favourable; however, an unperturbed supersaturated solution may not crystallize spontaneously for a period of days, months or even years in some cases.[3] This peculiar behaviour is observed due to the metastable nature of supersaturated solutions. Ostwald first investigated this behaviour, the outcome of which was the observation that some supersaturated solutions would either nucleate spontaneously or remain in solution for a significant period; these solutions were termed labile and metastable, respectively. These different states of a concentrated solution can be represented schematically using a solubility-supersolubility diagram, first proposed by Miers and Isaac[4] following their studies of crystallization from supersaturated solution. An example solubility-supersolubility diagram[2] is shown in Figure 1.1.

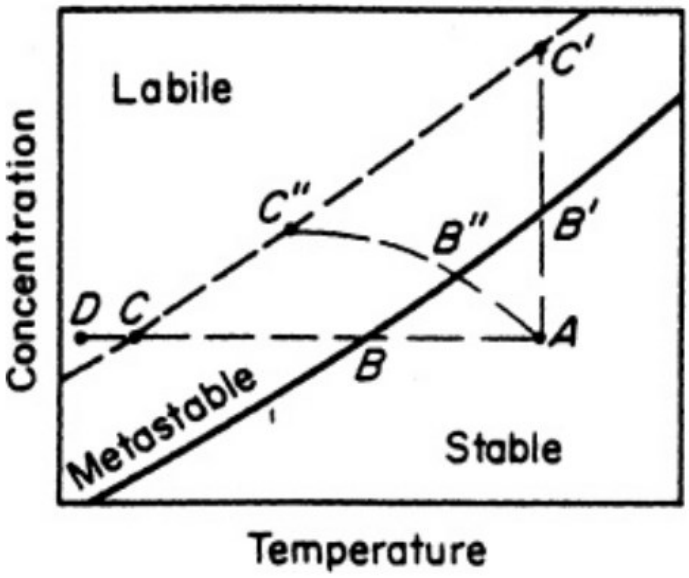

Figure 1.1 An example solubility–supersolubility diagram showing the stable, metastable and labile states of a concentrated solution. The solid line separating the stable and metastable regions (B–B') represents the solubility curve. The dashed curve separating the labile and metastable regions (C–C′) represents the supersolubility limit beyond which nucleation will proceed rapidly. The lines A–C and A–C′ represent two of the typical routes to achieve supersaturation; cooling a sample of fixed solute concentration and removal of solvent (evaporation) to increase solute concentration at fixed temperature. The line A–C″ represents a combination of these two methods. Figure reproduced from ref. 2.

1.1.3 Producing a supersaturated solution

For nucleation to occur, the solution must become supersaturated, or in other words enter the metastable region. There are several methods that can be employed to achieve this state including;

I. Modification of the solute solubility
II. Chemical reaction
III. Composition

Method (I) involves the addition of another substance that lowers the solubility of the solute in the system. The substance used can be a co-solute, however more commonly a secondary solvent is introduced called the anti-solvent or precipitant. Alternatively, if the result of a chemical reaction yields a product in a concentration greater than its solubility, then the state of supersaturation for the product is achieved; this method is most likely to be encountered in the crystallization of sparingly soluble salts. Methods (I) and (II) introduce additional components to the sample solution, so tend to be used only in certain circumstances. The state of supersaturation is more typically created by modifying the composition of a starting solution which can be prepared easily. The solubility of most salts increases with temperature, therefore by producing a solution at an elevated temperature the solution can transition from undersaturated to supersaturated during cooling to the desired temperature; this process is shown in Figure 1.1 by line A–C and can be used to provide solutions of a desired supersaturation with a high degree of accuracy. On the other hand, an undersaturated solution may be concentrated by evaporation of the solvent until the solution becomes supersaturated as shown by line A–C′. The level of supersaturation achieved by this method is difficult to control accurately, and

therefore tends to be used when exceeding the supersolubility limit is not a concern, e.g., during recrystallization.

1.2 Nucleation

Crystal nucleation is the process that sees the formation of a crystal nucleus in solution; the nucleus is the smallest crystalline particle that can persist and grow in solution. It is believed that nucleation is responsible for many of the key properties following crystallization such as particle size, morphology and crystal structure.[2,5] Although nucleation is of major significance in industry and research, a full description of the process has yet to be obtained. The lack of understanding in the area is due, primarily, to the difficulty associated with its study. Nucleation is not only a stochastic process, but the extremely small length scales (sub-nanometre) involved are extremely challenging to study.

1.2.1 Mechanisms of nucleation

Nucleation can occur via several different mechanisms, each of which requires specific considerations to be made, see Figure 1.2. Nucleation is typically classified as a homogeneous or heterogeneous process.[2]

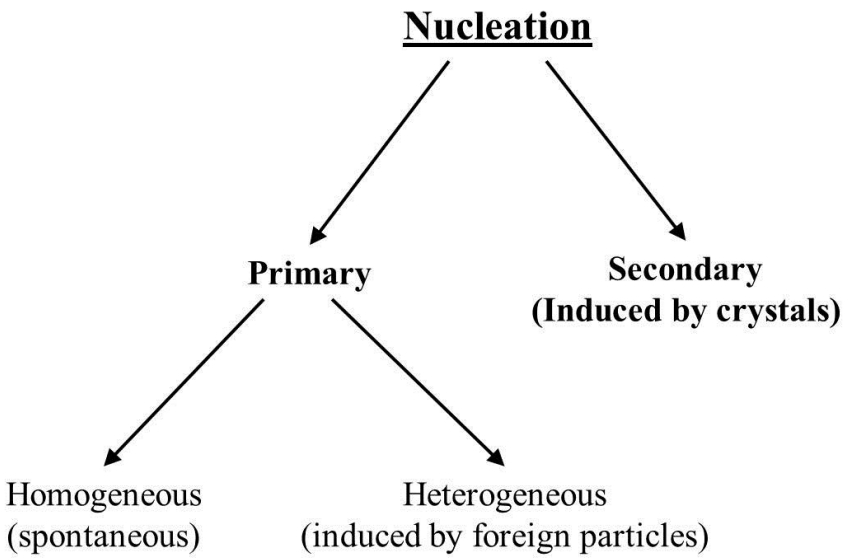

Figure 1.2 Schematic taken from Mullin identifying the different types of nucleation that can occur.[2]

Homogeneous nucleation is where a crystalline nucleus forms natively in a homogeneous solution or liquid. Heterogeneous nucleation occurs at an interface, i.e., at a solid surface such as an impurity particle or at a phase boundary. This mechanism of nucleation is more prevalent than others due to the fact that at an interface the free energy barrier to nucleation is lowered in comparison to the homogeneous case. Both homogeneous and heterogeneous nucleation are examples of primary nucleation; nucleation that occurs without contact with existing crystalline material. The alternative case of secondary nucleation can occur when the system already contains crystalline material, termed the mother crystal. The mother crystal can fragment during growth to produce small shards of crystalline material that continue to grow in the surrounding metastable solution/liquid to produce additional points of nucleation. Similarly, secondary nucleation can occur on the surface of the mother crystal.

1.3 Nucleation theories

Crystallization and nucleation have been studied for many years with the aim of providing a model that can account for the experimental observations. The long-standing description of nucleation is classical nucleation theory (CNT);[2,6] however, recent circumstantial evidence supporting solute clustering and the formation of dense liquid-like phases in solution have brought in to question the basis of CNT which has led to the formulation of other theories. The alternative theory that shows the most promise to describe the nucleation process is called the two-step nucleation model (2SM).[5,7-10] In the following sections both CNT and the 2SM will be outlined and discussed.

1.3.1 Classical nucleation theory

CNT is a theory based upon the early work of Gibbs,[11] Volmer,[12] Becker and Döring[13] and others who provided a theoretical account of condensation of water vapour to form liquid droplets. Soon after, the theory was extended to provide a description of the formation of crystalline nuclei. For homogeneous crystal nucleation, CNT describes the free energy change required to form a spherical crystalline nucleus of radius *r* from supersaturated solution. The total free energy

change (ΔG) is the sum of two components; the surface free energy (ΔG_s) and volume free energy (ΔG_v). The surface term describes the energy penalty associated with formation of a surface of a new phase in solution and the volume term accounts for the favourable contribution due to the formation of a solid particle of the new phase. An equation describing this process is given by,

$$\Delta G = \Delta G_s + \Delta G_v = 4\pi r^2\gamma - \frac{4}{3}\pi r^3 A \ln S \tag{1.4}$$

where r is the cluster radius, γ is the cluster–solution interfacial tension, $A = \rho RT/M$, where ρ is the mass density, M is the molar mass of the solid and S is the supersaturation. Competition between the two terms provides a prediction of a free energy barrier to nucleation. This maximum value (ΔG_c) corresponds to a critical nucleus size (r_c), the size that a nucleus must reach for nucleation to occur.

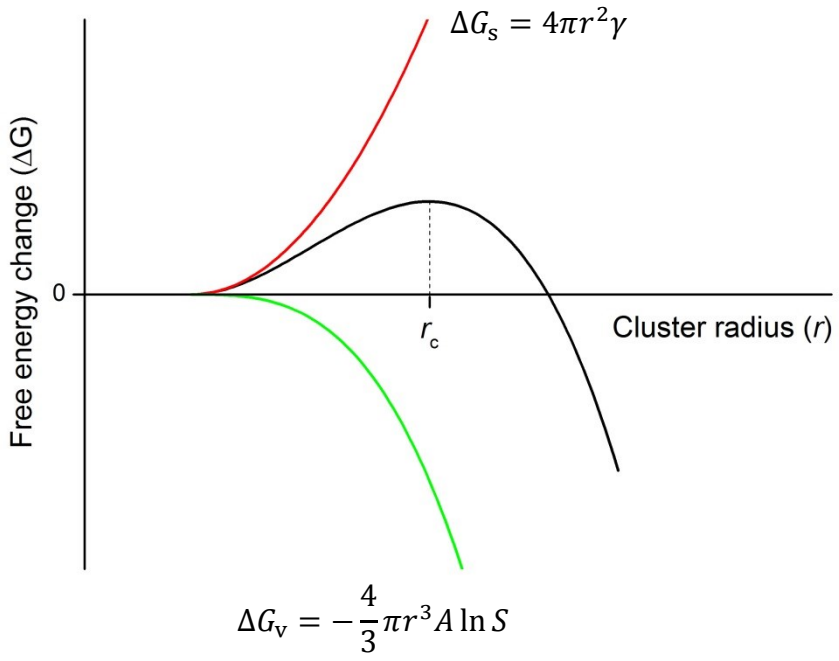

Figure 1.3 Schematic diagram showing the free energy barrier to nucleation obtained from classical nucleation theory (CNT). The green curve (bottom) represents the volume free energy (ΔG_v) and the red curve (top) represents the surface free energy (ΔG_s). The black curve (middle) is the resultant free energy profile (ΔG). The position r_c indicated on the x-axis indicates the critical cluster radius; the size that a cluster must reach to nucleate.

If a nucleus forms which is smaller than r_c, even if crystalline in structure, it will simply redissolve to reduce its free energy. Similarly, nuclei larger than r_c will continue to grow until all excess solute in the system has been consumed. The critical nucleus size can be calculated using Equation 1.5.

$$r_c = \frac{2\gamma}{A \ln S} \tag{1.5}$$

In order for a nucleus or cluster to attain critical dimensions it must gain additional solute and develop a crystalline arrangement while avoiding decomposition. In the classical picture, clusters are assumed to form via a series of bimolecular[2] additions until the critical dimensions are reached as demonstrated in the following sequence:

$$A + A \rightleftharpoons A_2$$

$$A_2 + A \rightleftharpoons A_3$$

$$A_{n-1} + A \rightleftharpoons A_n$$

where A_n represents a critical cluster. Critical clusters are assumed to be highly ordered in structure and spherical in shape. For this to be the case, it is assumed that the building blocks of the critical nuclei (monomers, dimers etc.) also share a complementary order to the critical nucleus, and therefore of the resulting macroscopic crystal form. Another significant feature of CNT is the treatment of the cluster–solution interfacial tension.[2,6,14-16] This parameter is approximated to be that of an infinite plane of macroscopic solid in contact with solution; the capillarity approximation. The value of γ is assumed to be constant for a given system, ignoring the expected curvature (size) and temperature dependencies.

1.3.2 Shortcomings of CNT

CNT is an attractive model to work with as it is computationally straight-forward to use, however, it is widely accepted that the simple CNT model cannot provide an accurate description of the nucleation process.[16-18] The use of bulk parameters in the description of pre-nucleation processes is considered to be inadequate, with large errors expected especially when small (nanometre) pre-nucleated clusters are considered. Even for the simpler case of droplet formation of a single component from the vapour (where all input parameters are known with a high accuracy), the predicted nucleation rate and that obtained by experiment differ

by many orders of magnitude.[18] CNT has been shown to provide a qualitatively reasonable account of the nucleation process but one that fails on a quantitative level in a range of situations.[15-22] The assumptions of CNT are in contrast with the results of simulation and experiment that imply the cluster–liquid interface is not a well-defined boundary and that the cluster need not be spherical in shape.[18,23,24]

1.3.3 Improvements to CNT

In order to obtain a model better able to provide physically realistic predictions, several modifications to CNT have been applied that have been found to improve the performance of the model. Since the early work of Tolman[25] it has been considered that a size-dependence of the interfacial tension should exist, with the value tending to that of a planar surface as the particle size increases. The corrected value, γ_n, can be approximated by the following Equation,

$$\gamma_n = \frac{\gamma_\infty}{1 + 2\delta/R} \tag{1.6}$$

where γ_∞ is the classical interfacial tension, R is the radius of the cluster/nucleus and δ is the Tolman length. The value of Tolman length (δ) describes the extent by which the surface tension of a small spherical object differs from its bulk (planar) value. By definition δ can be thought of as the linear coefficient in a Taylor expansion of the surface tension (γ) as a function of its curvature. Jayaraman et al.[26] have investigated the use of such a simple correction and applied it to the analysis of the data obtained from expansion cloud-chamber experiments.[27] Data was collated for condensation of a range of systems from supersaturated vapour and it was found that the modified CNT model was able to more closely reproduce the experimental observations. More recently, Horsch et al.[19] developed a more complex modification to account for the cluster size dependence of the interfacial tension, and also the expected non-sphericity of the clusters. This cluster size correction was based on the Tolman approximation (Equation 1.6). A size-dependent steric coefficient was employed to account for the non-sphericity of small clusters. The resulting surface property corrected (SPC) model and CNT were used to analyse molecular dynamics (MD) simulations obtained for homogeneous nucleation of a Lennard–Jones liquid from supersaturated vapour. It was found that CNT significantly underestimated the

nucleation rate and critical cluster size. Conversely, the SPC model was shown to reproduce simulation data over a wide range of temperature and supersaturation.

A thorough evaluation of nucleation theories that consider a diffuse droplet–vapour interface has been carried out by Napari, Julin and Vehkamäki.[28] The theories tested were diffuse interface theory (DIT), extended modified liquid drop-dynamical nucleation theory (EMLD-DNT), square gradient theory (SGT) and density functional theory (DFT); all of which were shown to outperform CNT in description of the nucleation rate and critical cluster size. The theories were used to analyse MD simulations of nucleation from Lennard–Jones vapours. DFT was found to be the best model to use, however the authors highlight the limitations of each model and the specific setting to which they would most reliably be used.

The nature of the modifications discussed here is directly related to the use of the droplet description of clusters. The improvements afforded by the modifications to CNT generally demonstrate a notable improvement of the theory in comparison to experimental data. However, it is important to highlight that these modifications are mostly *ad hoc* and not easily implemented to provide a general description of nucleation. Although this does not necessarily provide evidence in support of the CNT description, it is clear that the improvement is due to a more realistic treatment of the key component in nucleation: that is the fundamental nature of a pre-nucleated cluster. Rather than implementing modifications to the classical theory though, there is growing opinion that an entirely new theoretical model is required to describe the nucleation process.

1.3.4 The two-step model

The two-step model (2SM) postulates the formation of dense, liquid-like clusters of solute molecules, metastable with respect to the crystalline state, followed by a structural rearrangement to form a crystalline nucleus.

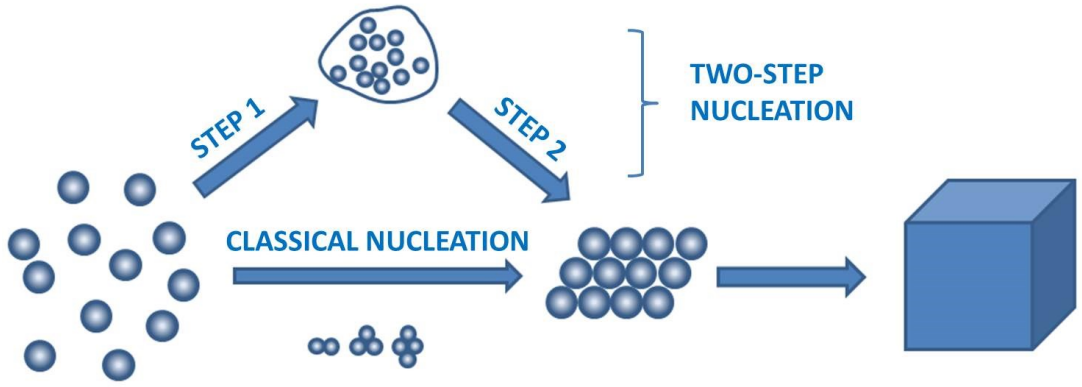

Figure 1.4 **A** schematic representation of the two-step nucleation process based on ref. 5. Step 1 sees the formation of dense regions of solute which are metastable with respect to the crystalline form. Step 2 involves a structural rearrangement within the amorphous cluster to produce a crystalline (or near crystalline) arrangement. If the resulting nucleus is large enough to survive in bulk solution conditions it will continue to grow to form a macroscopic crystal. In the classical description solute monomers add together one at a time in crystalline arrangement, until critical dimensions are reached.

The resulting nucleus will grow to consume the excess solute available in the dense cluster and will then only survive in solution if it has reached a size sufficient to avoid dissolving in the surrounding solution of lower solute concentration. This is similar to the concept of a critical cluster size described by CNT. In contrast to CNT, the 2SM makes no assumption regarding the shape of a solute cluster or its internal structure. The 2SM was initially based on the observations made during studies of protein crystal nucleation;[10,29,30] however, recent experimental and computational work suggests that the two-step mechanism may be a more universal route to nucleation.[31,32]

Prior to the suggestion of a 2SM of nucleation, it was proposed that solute clustering occurred in supersaturated solutions;[33-38] however, the role of clusters in the nucleation process was unknown, or at best unclear. Simulations of crystal nucleation of a model globular protein performed by ten Wolde and Frenkel provided one of the first reports of a two-step nucleation scheme where solute clustering was key to the nucleation process.[10] Around the critical point, the lowest energy route to the critical nucleus involves the evolution of regions of increased solute density. In other words, the first step to nucleation was formation of localized regions of a dense liquid phase, followed by formation of a crystalline nucleus within that region. It

was also shown that the free energy barrier to nucleation was significantly lowered near the critical point, increasing the nucleation rate by many orders of magnitude. Following this report, particular attention was paid to the application of the two-step model to nucleation in colloids[39-42] as well as continued investigation of protein systems.[29,30,40,43]

Simulation has also been applied to the case of nucleation of a simple salt from solution. Shore and Perchak investigated the nucleation of silver bromide (AgBr) from aqueous solution reporting that, from a homogeneous starting solution, disordered solute clusters formed and grew with time.[32] Comparison to the clustering observed *in vacuo*, where clusters as small as Ag_4Br_4 have crystalline arrangement, suggest that solvent plays an important role in the structure of solute clusters in solution. The disordered nature of AgBr(aq) clusters supports the idea that the formation of disordered clusters precedes the process of nucleation.

Recent theoretical work reported by Lutsko and Nicolis also suggests that the two-step nucleation mechanism can be applied to systems other than proteins and colloids.[44] Density functional calculations of the free-energy landscape for a model protein and a simple Lennard-Jones liquid showed that the nucleation of both systems proceed through a metastable disordered state. Experimental evidence in support of the disordered dense phase for non-protein systems is limited; however, the authors highlight that due to the short lifetime expected for the metastable phase of the simple liquid, it may be experimentally challenging to observe. This has been disputed by more recent studies in which localised regions of dense metastable phase have been observed with long lifetimes.[23,24,45,46]

1.3.5 Rayleigh laser scattering: evidence of solute clusters?

Direct experimental evidence to suggest that the two-step mechanism occurs in other systems such as nucleation of smaller, simpler molecules is limited. For the case of small-molecule and ionic systems, the majority of evidence supporting the two-step mechanism is suggested from other measurements such diffusivity,[33-35,47] dynamic light scattering[48] (DLS) and Rayleigh scattering.[23,24]

A series of simple laser scattering experiments were carried out by Lian et al.,[49-51] the results of which identified long-lived particles moving freely through

solution in a range of different aqueous solutions including supersaturated potassium dihydrogen phosphate (KDP), saturated solutions of potassium chloride (KCl), and undersaturated solutions of sucrose.

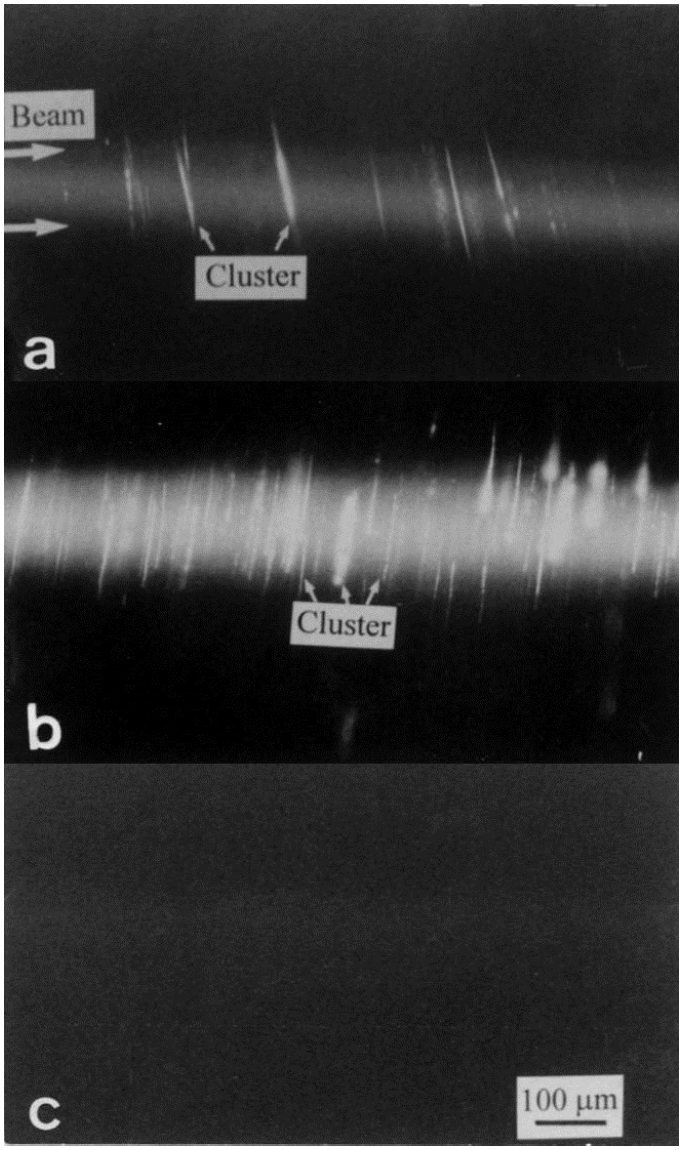

Figure 1.5 Pictures taken from Lian et al.[49] showing the scattering observed in (a) supersaturated KCl solution; (b) sugar solution; (c) ultrapure water. The photographs shown were acquired using a long exposure (180 s). The incident laser beam (λ = 488 nm, P = 100 mW) was focussed to form a waist of ~100 μm. The streaks crossing the laser beam show the trajectories of particles moving through solution during the exposure period. It is clear that no particles are identified in the ultrapure water sample while particles can be seen in KCl solution; more, and larger, particles are present in the sugar solution.

The KDP system was investigated as a function of supersaturation where the number density of particles was seen to increase monotonically with supersaturation.[50,51]

The scattering experiments were repeated with a growing seed crystal in solution, it was seen that the number of particles in the diffusion boundary layer of the growing crystal also increased with supersaturation.

In a later set of experiments the group observed scattering objects in aqueous solutions of KCl, KDP and sucrose.[49] The size of the particles was estimated using a laser scanning particle counter which showed the majority of particles to be below 100 nm in diameter. Comparing the sucrose and KCl samples (see Figure 1.5) many more and larger objects are seen in the sucrose sample; this possibly reflects the higher solubility of the sugar and the larger monomer size. The scattering objects are thought to be long-lived solute clusters, the numerical density of which is dependent on degree of supersaturation.

Of particular significance was that these particles were clearly seen to interact with the growing crystal. In bulk solution, the particles were seen to move around freely due to Brownian and thermal effects; however at a certain distance from the crystal, they would begin to migrate towards the crystal increasing in velocity until they were on the crystal surface. The particles would then move around on the surface, typically moving to edges and corners, before the observed scattered signal would disappear. Due to the high solute flux that is expected towards a growing crystal, it is possible that any particle, i.e., impurity particles, would be transported along with solute monomers, however the fact that these scattering objects apparently disappear while in contact with the crystal at the regions of high growth is a strong indication that the objects in question are directly involved in the growth process.

A recent report by Jawor-Baczynska et al.[24] has provided valuable evidence to support the notion of solute clustering in supersaturated aqueous glycine solution. The dissolution of glycine to form a slightly supersaturated (S = 1.1, T = 25 °C) solution was found to cause the formation of solute-rich nanodroplets. The population of nanodroplets was characterised by dynamic light scattering (DLS), nanoparticle tracking analysis (NTA) and small-angle x-ray scattering (SAXS) obtaining mean particle diameter of ~250 nm and a concentration of approximately

10^9 per mL. The nanodroplets were present indefinitely in solution and were observed during sample cooling from the undersaturated region to the final supersaturated state. Filtration using a hydrophilic membrane was required to reduce the number of nanodroplets in solution; however, this was found to have no effect on the time taken for spontaneous nucleation to occur, suggesting the concentration of 250 nm nanodroplets was not directly related to nucleation. When samples were tumbled with a stir bar, the time for nucleation was reduced from a period of days to only a few hours. The authors took great care to eliminate factors such as secondary nucleation, bubbles or mechanical damage as the source of nucleation. Samples analysed after tumbling, but prior to nucleation, showed the presence of a subset of larger nanodroplets with mean diameter > 750 nm. It was suggested that the action of tumbling was sufficient to induce coalescence of nanodroplets to form the larger (> 750 nm) species, which are required for nucleation to occur. It was proposed that the larger nanodroplets are of sufficient dimension to produce a crystal nucleus large enough to survive and grow in bulk conditions. These findings are in good agreement with the two-step model of nucleation.

Jawor-Baczynska et al.[23] later extended their work to investigate solute clustering in the supersaturated (S = 1.4) aqueous DL-alanine system in which solute clustering was found to be prevalent as in aqueous glycine solution. The populations of particles found in glycine and DL-alanine solution were investigated as a function of supersaturation. Experiments were carried out at a fixed temperature of 25 °C and supersaturation was controlled by varying solute concentration. It was shown that the number density of clusters found in solution decreases with supersaturation; however, mean cluster size appears relatively constant. As in their initial work, it was shown that clusters could be removed by filtration and then regenerated by a period (120 hours) of gentle mechanical action (inversion of sample). The regenerated particle population is almost identical to that measured before filtration, suggesting that the presence of clusters represents an equilibrium position in solution where a population of stable solute clusters can persist.

Although the amount of evidence from simulation and experiment in support of a two-step nucleation process is growing, much of it is based on the identification of populations of particles in solution. In such reports the particles have been

reported as evidence of the existence of solute clusters in solution; however, the evidence provided to-date is far from conclusive and could be interpreted as identification of impurities rather than solute clusters. The work of Jawor-Baczynska et al. is the first that has provided strong evidence that the particle populations are not due to impurities; the ability to remove and regenerate populations of particles is very difficult to explain in terms of solution impurities. It is important that future work in this area is directed towards establishing the nature of the particles identified in experiments.

1.4 Non-photochemical laser-induced nucleation

Study of the nucleation process has been advanced in recent years following the discovery of non-photochemical laser-induced nucleation (NPLIN).[52] This technique allows the researcher to exert a unique degree of control over the stochastic nucleation process by localizing the nucleation to occur within the volume of solution illuminated by the incident laser beam and to occur within the duration of the laser pulse(s).[53-55] Nucleation is caused by exposing a metastable sample to low-power laser pulses (~10–100 MW cm^{-2}). The mechanism at work is thought to closely resemble that of native homogeneous nucleation, with sample solutions transparent to the incident wavelengths, and powers insufficient to cause photomechanical effects. All reports of NPLIN to date have used the two-step model as the basis for explanation of the experimental findings and provide compelling evidence in support of the non-classical description. NPLIN has been demonstrated in a number of systems ranging from simple ionic salts such as potassium chloride (KCl),[53] to proteins such as hen egg-white lysozyme (HEWL).[56] Although the methods employed in experiments are very similar, features of the solute used and the resulting crystal form have led to the formation of different models to account for the experimental observations. The relevant literature will be reviewed in the following Sections.

1.4.1 Initial discovery

The first account of non-photochemical laser-induced nucleation was documented by Garetz et al., where the effect was first observed during the course of

an experiment designed to look for second harmonic generation from concentrated, aqueous urea solutions.[52] Supersaturated solutions (S = 1.10–1.29) were exposed to trains of intense (50–250 MW cm^{-2}) near infra-red (λ = 1064 nm) laser pulses and it was noted that this caused some samples to nucleate within 10–20 seconds of exposure to the beam. Curiously, it was found that in order to see this effect, samples were required to be *aged* for a period of days prior to experiment. Sample ageing was said to allow solute clusters of critical dimension to form in the solution which are a pre-requisite of NPLIN.

This hypothesis is in-line with the proposed two-step mechanism of nucleation with ageing expected to increase the mean size of dense, liquid-like solute clusters to critical dimensions required for nucleation. Samples of varying concentration were shot at different laser powers and it was seen that there was a minimum sample concentration (12.0 M, S = 1.15) needed for NPLIN to occur. Similarly, there was a minimum, threshold power required for NPLIN; no nucleation was noted for 50 MW cm^{-2} pulses, and however 250 MW cm^{-2} pulses readily caused nucleation. More interestingly, the incident polarization was flipped between vertical and horizontal with the observation made that the initial crystallite needle that formed appeared to be approximately aligned with the angle of polarization.

A photochemical mechanism was ruled out for this process after considering the transparency of the sample solution and solute at the incident wavelength. The photon energy associated with 1064 nm pulses was considered too low to induce photochemistry; typically associated with ultraviolet (UV) irradiation. Furthermore multiphoton absorption was ruled out due to the low laser power and the use of an unfocussed beam. To explain these results, Garetz proposed a mechanism based on the alignment of urea molecules with the direction of the incident electric-field vector.

The urea molecule possesses a permanent dipole moment along the direction of C_2 rotation axis (see Fig. 1.6), however, it is highlighted that the optical frequency of 1064 nm light is too great to cause any alignment of the molecule with the field. Conversely a mechanism based on the optical Kerr effect (OKE) was proposed in which the electric field acts on the urea molecules in two discrete ways simultaneously. Firstly, the field induces an anisotropic polarization in the

molecule(s), the field then acts on this induced dipole moment to align the most polarizable axis of the molecule with the electric field. This alignment, or increased ordering, of the solute molecules was thought to increase the chance of nucleation occurring, presumably due to a lowering of the free energy barrier to nucleation.

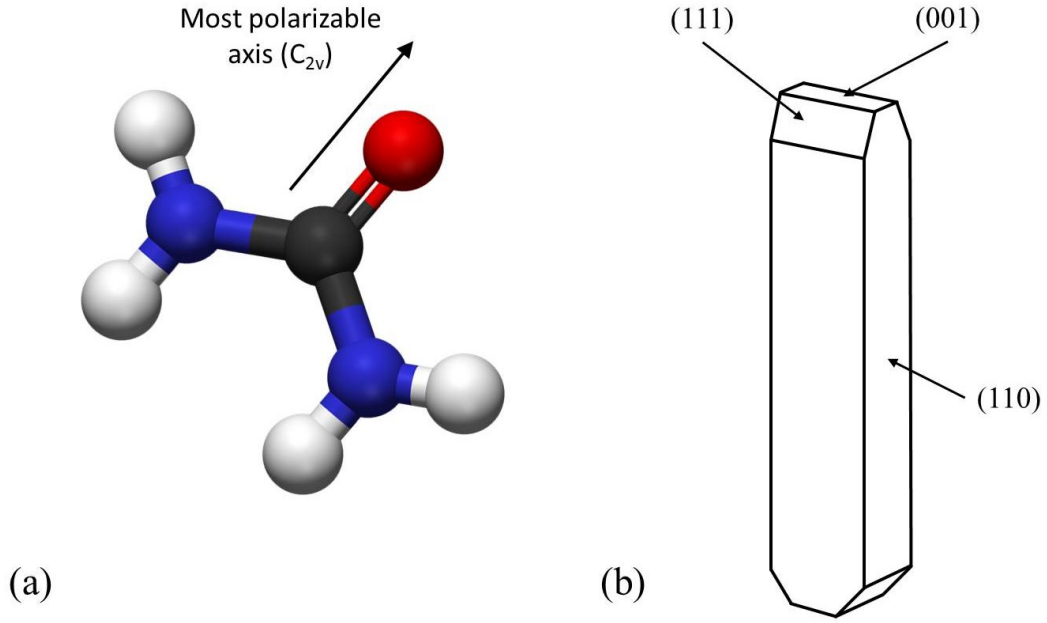

Figure 1.6 Schematic diagram adapted from ref. 52 showing (a) the molecular structure of urea and identifying the most polarizable axis of the molecule which is along the direction of the C=O double bond; and (b) an illustration of the crystal habit of a urea needle with the crystallographic faces indicated. The most polarizable axis identified in (a) coincides with the needle axis of the urea crystal.

Garetz et al. later re-investigated the aqueous urea system in more detail with circularly and linear polarized light (CPL and LPL), and found that wavelengths of 532 and 1064 nm caused NPLIN.[57] The data all show an apparent nonlinear dependence of nucleation probability with incident laser intensity; however there appears no general trend to the data points (see Fig. 1.7). The noisy data is attributed to a small number of samples used in experiment (approximately 6 per data point). In all cases, though, it could be argued that at low laser intensities the points follow a near-linear relationship: a feature that has since been observed in many reports of NPLIN. The results show that LPL is more effective at causing nucleation in the

11.9 M solution (~ $S = 1.45$), showing approximately double the fraction of samples to nucleate at a given laser power. This was explained by considering the known arrangements of urea monomers in solution, which form rod-like, *n*-mers with an enhanced polarizability in the stacking direction. It was proposed that LPL can align such structures more efficiently than CPL.

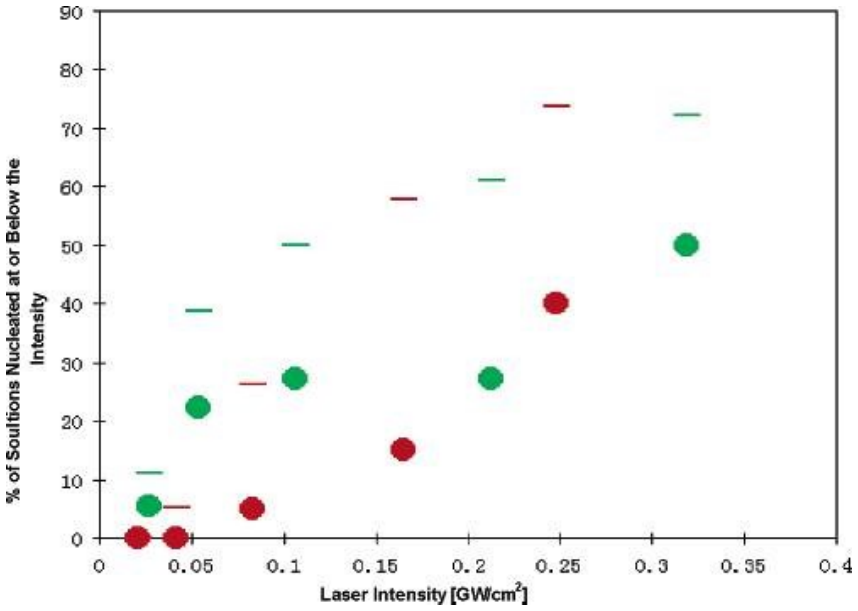

Figure 1.7 Plot taken from ref. 57 showing the laser intensity dependence of nucleation probability for supersaturated ($S = 1.44$) aqueous urea solutions using CPL and LPL. The points in green represent the fraction of samples nucleated using 532 nm light, and those in red represent the fraction of samples nucleated using 1064 nm pulses. The circles represent the fraction of samples nucleated using CPL and the straight line points represent the nucleation probability using LPL.

The effect of wavelength is more subtle, with 532 nm pulses providing a lower threshold power to NPLIN as well as being slightly more efficient at causing nucleation at a given laser power. This effect is demonstrated in Figure 1.7 for both LPL and CPL. The Kerr-effect model expects no wavelength dependence as it depends solely on the magnitude of the applied electric field. Garetz attributes the observed wavelength dependence on the differing degrees of sample heating that will occur in the sample when using 532 or 1064 nm light. In this study, Garetz highlights a significant problem with the hypothesised mechanism. At the electric field magnitudes achieved in these type of experiment, the calculated induced-dipole interaction energy, $\frac{1}{2}(\Delta\alpha)E^2 = 10^{-4}\, k_B T$, where E is the optical electric field, $\Delta\alpha$ is the

molecular polarizability anisotropy, k_B is the Boltzmann constant, and T is the absolute temperature. The estimated interaction energy for one molecule in an electric field is orders of magnitude too small to account for NPLIN. It was suggested that the interaction energy may scale with solute cluster size to a point where it becomes at least competitive with the random thermal energy of the system. Following from their initial work, Garetz et al. went on to demonstrate NPLIN in a range of systems including L-histidine,[58] hen egg white lysozyme[56] (HEWL) and glycine.[59-61]

1.4.2 Polarization switching

Of the several studies reported by Garetz et al., NPLIN in the aqueous glycine system is of particular significance. Glycine is the simplest of the amino acids, and in crystalline form, under ambient conditions, can assume one of three different polymorphs, α-, γ-, or β-glycine.[62] The γ- form is the thermodynamically stable form; however α-glycine is the polymorph that is seen to form spontaneously, at moderate supersaturations, as the kinetically favoured crystal product. The β-glycine polymorph is metastable and its transformation to α- or γ-glycine has been studied in great detail.[63,64] The metastable β-form can be obtained using certain experimental conditions such as crystallization from alcohol–water mixtures, or freeze drying. Comparing the structures of α- and γ- glycine, we see two very different arrangements. Formation of α-glycine can be thought of as the addition of dimers of zwitterionic glycine ($^{+}NH_3CH_2COO^{-}$) to form hydrogen-bonded double layers in a centrosymmetric arrangement.

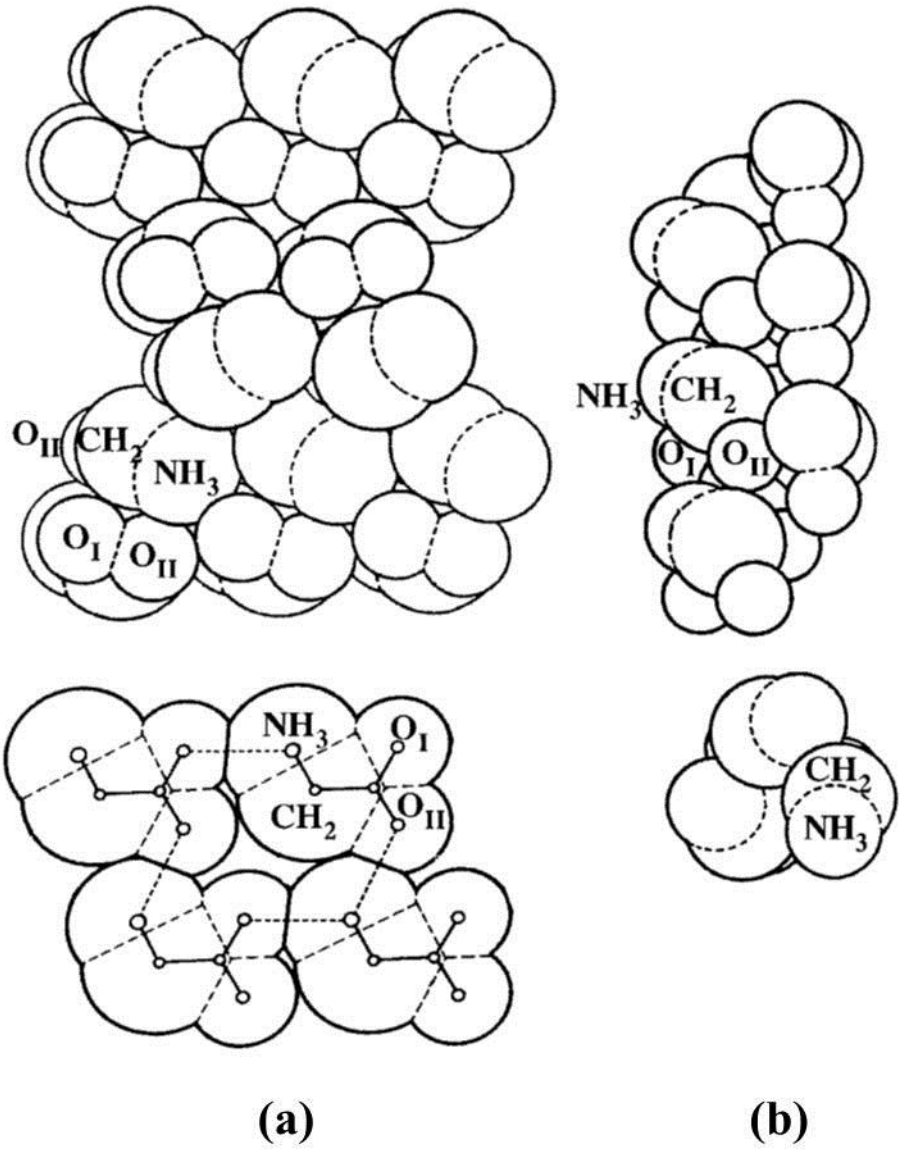

Figure 1.8 Diagram reproduced from ref. 59 showing the molecular units considered to be the building blocks of α- and γ- crystal polymorphs of glycine.[59] In α-glycine (a), cyclic dimers pack together to form hydrogen-bonded double layers; the planar arrangement is shown in (a, lower) and the stacking of layers is shown in (a, upper). In γ-glycine, helical chains with 3-fold axis are formed which pack together hexagonally in the crystal structure. The helical building block is shown in (b); a view along the chain length (upper) and the perpendicular view (lower).

In contrast, the crystalline structure of γ-glycine shows three-fold helical chains packed together hexagonally, through hydrogen bonding, in a non-centrosymmetric configuration.

In their studies,[61] Garetz et al. prepared solutions with concentrations 3.7–3.9 M (approximately S = 1.38–1.45) that were shot with trains of multiple pulses (10

pulse s^{-1}, for minutes) of 1064 nm light (FWHM 9 ns) with peak intensities of ~700 MW cm^{-2}. Following their initial work, sample solutions were aged for a period of 4 days before being used. For each sample exposed to the laser, an identical sample was removed as a control for spontaneous nucleation. Unlike the case of the urea system, if a sample nucleated following laser exposure, crystals could first be seen after 30 minutes. Nucleated samples were analysed using X-ray diffraction (XRD) with the results showing formation of the unexpected γ- polymorph, with the control samples producing, exclusively, α-glycine. Samples of aged solution were also exposed to laser pulses with peak intensity ~200 MW cm^{-2}; no samples were seen to nucleate. Similarly, un-aged samples were exposed at ~700 MW cm^{-2} and none of these samples were seen to nucleate.

Later studies compared the effect of LPL and CPL on the NPLIN of glycine.[59,60] The findings verified that pulses of LPL resulted in formation of γ-glycine. In contrast, it was shown that samples which nucleated due to CPL exclusively formed α-glycine. The efficiencies of both polarizations were shown to be almost identical, however many fewer samples were exposed to CPL. A summary of these results are shown in Table 1.1.

	Power Density (j) / GW cm^{-2}	Shot	Nucleated	Fraction (f)
CPL	0.7	18	8	0.44
LPL	0.7	46	22	0.48

Table 1.1 Summary of the effects of different polarizations of light on the efficiency of nucleation by NPLIN in supersaturated aqueous solutions of glycine.[59] Samples nucleated using circularly polarized light (CPL) exclusively formed the α-polymorph, while samples nucleated using linearly polarized light (LPL) exclusively formed the γ-polymorph.

Considering the expected polarizability anisotropy of the structural motifs of the two different polymorphs, these findings appear consistent with an optical Kerr effect-based mechanism. It can be shown that a molecular *n*-mer with a rod-like polarizability (γ-glycine, helical chains) is more easily aligned with LPL, and that an aggregate with disc-like polarizability is more easily aligned with CPL. It is thought that in solution, there exists a population of solute clusters some of which have more rod-like polarizability and others with more disc-like polarizability as a result of their

constituent *motifs*. When in the presence of the appropriate optical field (LPL or CPL), the constituent units of the clusters are in some way re-organized, and nucleation of the organized cluster can proceed. Within the window of solution conditions where polarization switching occurs it is noted that approximately equal fractions of α- and γ- samples are formed. This result is consistent with the idea that in a pre-nucleated solution, within the switching window, equal proportions of α- (44%) and γ- (48%) precursor clusters are present. This inference further highlights that significance that solution structuring has on NPLIN and likely nucleation in general.

Work on polarization switching was further developed, with a more comprehensive study over a wide range of solution conditions.[60] Samples of concentration 3.1–4.4 M were prepared and studied over a range of temperatures (15–25 °C); the resulting supersaturation of these samples were $S = 1.19–2.00$. Aged samples (1–4 days) were subjected to LPL and CPL pulses of light with wavelengths of 532 and 1064 nm. NPLIN was seen to occur at all supersaturations above 1.30. At low supersaturations, both CPL and LPL light generate α-glycine and at high supersaturations both polarizations act to produce γ-glycine. However, there exists a narrow window of temperature and supersaturation where LPL is exclusively seen to produce γ-glycine and CPL light yield α-glycine only. Garetz termed this effect "polarization switching", and it was seen for both 532 and 1064 nm laser light. The value of supersaturation at which polarization switching occurs is slightly higher for 1064 than for 532 nm pulses; this was attributed to a greater extent of sample heating at 1064 nm.

As a test for the notion of polarization switching, samples of $S = 1.40–1.60$, were exposed to different degrees of elliptically polarized light between LPL and CPL. Out with the established polarization switching window, the ellipticity of light had no bearing on the nucleated crystal form. However once in the switching window, it was seen that increasing ellipticity (more circular character) saw an increasing probability of forming α-glycine at a supersaturation that produced γ-glycine at lower ellipticity (more linear character). As the limits of supersaturation at which the window of polarization switching is active, the effect becomes more difficult to observe.

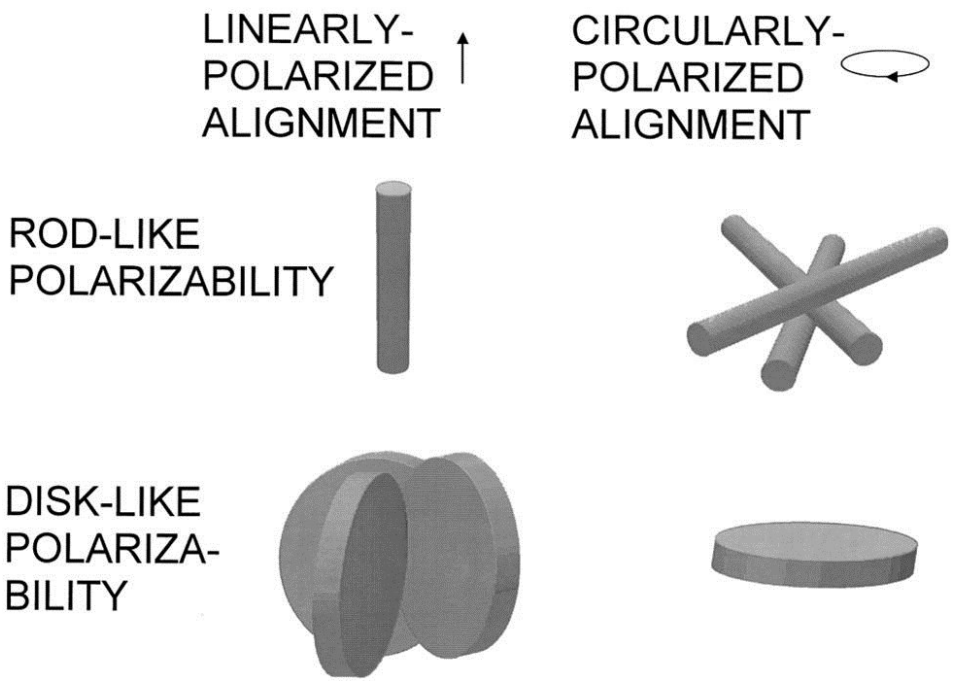

Figure 1.9. Schematic representation (from ref. 59) of the interaction of molecules with a rod-like polarizability (top row) and disc-like polarizability (bottom row) with the electric field associated with linearly (left column) and circularly (right column) polarized light. For the OKE, it is expected that a molecule with rod-like polarizability (i.e., helical chains of γ-glycine) would be effectively aligned with a linearly polarized field; and that a molecule with disc-like polarizability (i.e., circular dimers of α-glycine) would be effectively aligned with a circularly polarized field.

Following the report of polarization switching in supersaturated glycine solution, Garetz et al. then demonstrated the effect in aqueous solutions of the amino acid L-histidine, with similar observations reported.[58]

1.4.3 Polarization switching for continuous-wave laser beam

Polymorph control in the aqueous glycine system has also, more recently, been demonstrated by Rungsimanon et al. where it was found that use of intense CPL or LPL in an optical trap could bring about preferential nucleation of α- or γ-glycine, respectively.[65,66] In these experiments, a continuous wave (CW) laser producing 1064-nm light was passed through a microscope objective (×60 magnification, NA 0.90) to form an optical trap. In order to minimise sample heating, glycine samples were prepared in D_2O to be supersaturated (S = 1.36), saturated (S = 1.00) and undersaturated (S = 0.68). A small amount of the sample solution (15 μL) was

placed in the optical trap, such that the focus was incident at the air–solution interface, and samples were exposed to the trap for a period of 30 minutes. During the course of experiment, the mean power of the CW laser was varied between 0.8–1.4 W, achieving peak power densities in the range 0.28–0.49 GW cm^{-2}. Interestingly, the group notice two different behaviours; in the supersaturated and saturated solutions it is seen that α-glycine is typically formed, with the probability of γ- formation increasing with laser power for both CPL and LPL. A summary of the results are shown in Figures 1.10–1.12.

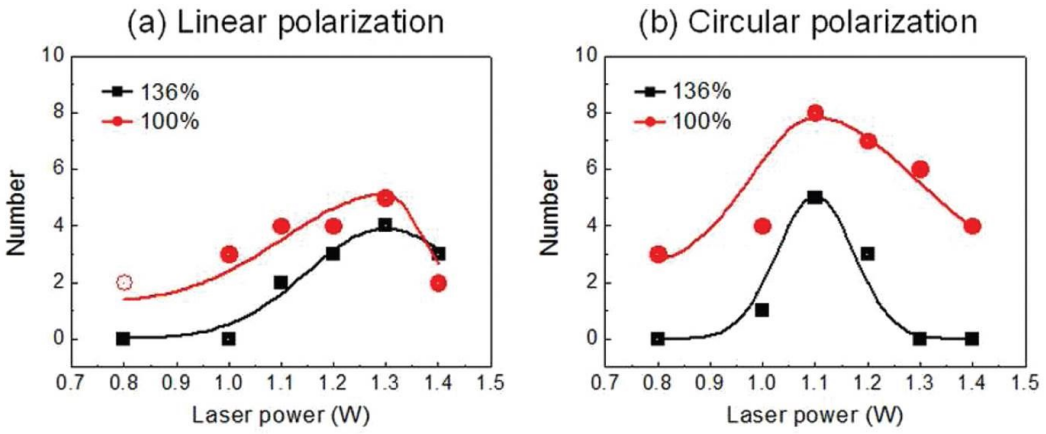

Figure 1.10 A summary of the effect of laser polarization, supersaturation (labelled as either 100 % or 136 %) and laser power of the resultant polymorph following nucleation.[65] The values shown on the *y*-axis show the number of samples (out of 10) that gave γ-glycine. Figure was reproduced from ref. 65.

In contrast to the work of Garetz et al., the results of Rungsimanon et al. show that CPL is more effective than LPL at causing formation of γ-glycine crystals from saturated/supersaturated solution. This is in contrast with the polarization dependence of nucleation probability recorded for undersaturated glycine solution (68 %) where it was seen that LPL almost exclusively (9/10 samples) formed γ-glycine: see Figure 1.11.

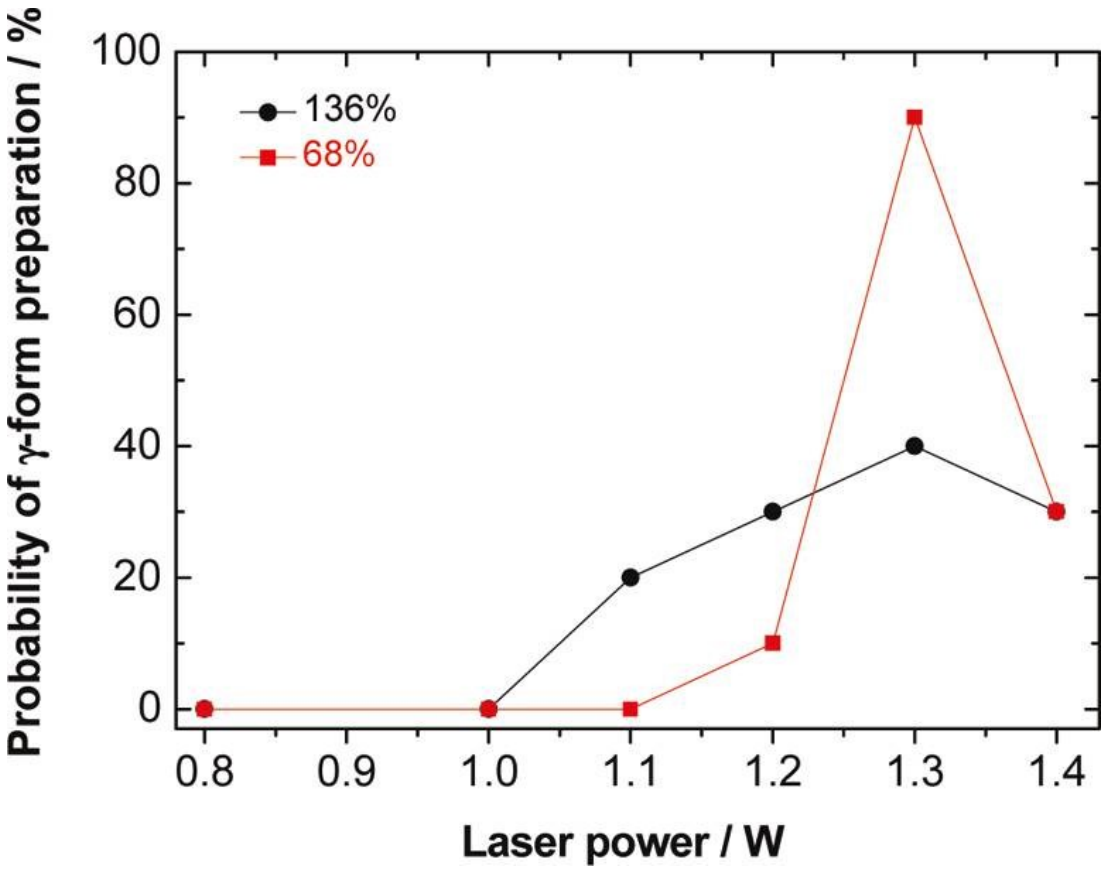

Figure 1.11 The probability of forming γ-glycine following exposure of 10 undersaturated (68 % red squares) and 10 supersaturated (136 %, black circles) glycine solutions to LPL laser light (λ = 1064 nm, CW). The results show that undersaturated solutions almost exclusively (9 from 10) form γ-glycine; however supersaturated solution is more likely to form α-glycine crystals. Figure reproduced from ref. 65.

In the trapping experiments, the optical trap is thought to gather solute clusters in the region of the focal spot due to radiation pressure. Presumably, the ability to trap these species is increased by focussing close to the liquid-air boundary, with the interface used to impede clusters from leaving the trap in the axial direction. In addition, the position at the droplet surface should limit localised heating due to cooling effects at the droplet surface. The capacity of the laser trapping crystallization to induce nucleation depends on the supersaturation increase in the region of the focal spot, the temperature increase in this region and also how effectively the trap can accumulate these species. The results show a complex relationship between polarization, supersaturation, local temperature and molecular rearrangement. Nonetheless, it is clear that varying the polarization of light has a

definite influence on the polymorph that is formed following nucleation. Prior to experiment, the glycine solutions are expected to contain a significant population of pre-existing solute clusters of the α-glycine type. Owing to their polarizability, these will be more effectively trapped in a field consisting of CPL. When the effective supersaturation at the focal spot of the trap exceeds that required for spontaneous conversion of α- to, the thermodynamically favoured, γ-glycine the result of crystallization will be γ-glycine. For LP irradiation, such high trapping powers are required to drive γ-glycine formation that sample heating in this region limits the efficiency of the process; this explanation is summarized in the graphic shown in Figure 1.12.

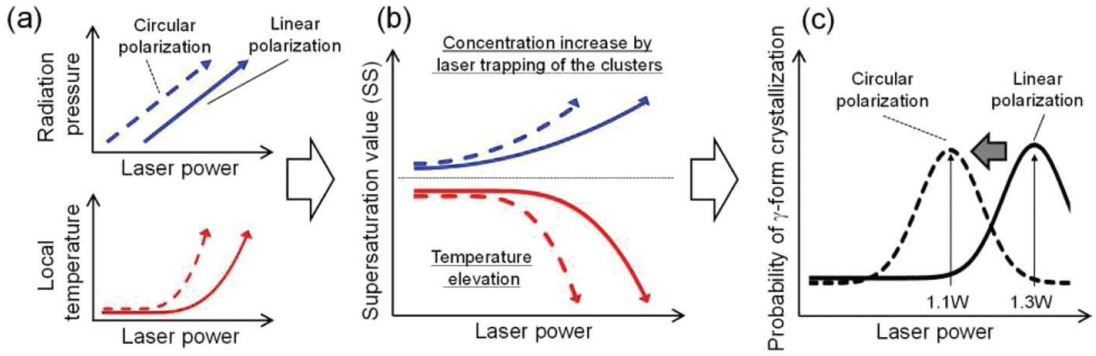

Figure 1.12 Graphic taken from Sugiyama and co-workers[65] that summarizes their account of the experimental observations. Assuming a pre-existing population of α-glycine precursors (cyclic dimers) it is expected that the clusters would be more effectively trapped by an optical trap formed by CPL. The lines shown in (a), (b) and (c) demonstrate the expected differences when using CPL (dashed lines) and LPL (solid lines). The scheme of plots demonstrates why CPL is more effective at producing γ-glycine than LPL in saturated and supersaturated solution.

In contrast, in the undersaturated samples, there is not expected to be a significant population of pre-existing solute clusters. In this case, the effect of polarization is thought to *template* the formation of solute aggregates in the system due to the polarization of the active field. The group explain that when CP light is used to form the optical trap, over time, this leads to the formation of clusters with polarizability concurrent with the present field, in this case clusters of glycine dimers. Similarly, that the use of LP light leads to the formation, and trapping, of clusters with rod-like polarizability *i.e.*, clusters with γ-glycine character. When the concentration of clusters reaches a critical point, nucleation proceeds, forming the

polymorph defined by the type of clusters formed in-field. Therefore, in the undersaturated case, the group see results of polarization parallel to those of Garetz in the pulsed laser study.

The study presented by Sugiyama differs to that of Garetz et al. as they do not use a pulsed laser to induce nucleation, rather the optical trap, locally, increases the level of supersaturation (cluster number density) to critical levels and nucleation proceeds. More importantly, however, is the inference that the γ- polymorph forms by spontaneous transformation of α- nuclei under high concentration conditions and that the results are not explained in terms of γ- type clusters native to the solution.

1.4.4 Solution cluster structure

The studies of NPLIN discussed so far have been explained by means of a mechanism based on the optical Kerr effect, as first proposed by Garetz et al. The evidence of polarization switching is, perhaps, the best evidence to date in support of this mechanism. However, this mechanism relies heavily on the idea that structural motifs, present in the crystalline solid, are prevalent in the supersaturated solution also. There has been evidence presented claiming that solute clusters in supersaturated solutions of aqueous glycine contain, mostly, hydrogen bonded dimers (which are thought to be the building block of α-glycine).[67] However, this has recently been disputed with evidence presented suggesting that glycine exists primarily of monomers in solution.[68,69] We are unaware of other studies that have presented data suggesting that solute clusters share structural features in common with the crystalline solid. Further study in this area, to help elucidate the structure of supersaturated solutions would be highly beneficial to further work in the field of NPLIN. Prospective techniques that show promise is small-angle neutron scattering (SANS)[70-72] and small-angle X-ray scattering (SAXS)[72-74] and related methods. These techniques have already been employed to investigate solution structure; however, studies to date have mainly focussed on dilute solutions. Furthermore, it may be advantageous to couple scattering studies with NPLIN in order to gain an insight to how the solution structure and dynamics change during the nucleation process.

1.4.5 Simulations of NPLIN

It is becoming evident that NPLIN is an area in which computational studies could be particularly valuable, with a particular focus on exploring the dynamics of such systems. The first study of its type was conducted by Knott et al., where the hypothesis of an optical Kerr effect mechanism for NPLIN was examined.[75] The group tested whether solute alignment by the optical Kerr effect was a likely cause of sample nucleation in NPLIN. Using a modified Potts lattice gas model of crystallization, it was shown that applying an orientational bias to solution can accelerate the nucleation rate by reducing the free energy barrier to nucleation. This enhancement of nucleation was demonstrated for both the classical and two-step nucleation mechanisms. However, when the simulation was performed using field strengths achieved in experiment (~10^7 V m^{-1}) the calculated reduction in free energy barrier is found to be completely negligible (<< $k_B T$). Electric field strengths several orders of magnitude greater than those achieved in experiment, would be required in order to account for experimental observations. These findings re-affirm estimates made by Garetz et al. More importantly though, the study by Knott et al. highlights the importance of computational work in this area as a means of testing hypotheses as well as obtaining information that would otherwise be challenging to obtain experimentally.

Nardone and Karpov have provided a theoretical model describing the formation of needle-shaped, metallic particles in strong electric fields.[76,77] In their analysis, the authors suggest that the nucleation of metallic particles in solution may be the origin of crystal nucleation in NPLIN experiments.[78] Unlike a dielectric, a metallic particle would experience a huge polarization in an applied field, the magnitude of which would be accentuated significantly for a needle-like shape. Such a polarization would result in a greater reduction in the free energy barrier to nucleation that would allow the nucleation of a metallic particle to be fully accounted for (energetically) in the classical picture. However, the origin of the metallic particles from the solution of a dielectric was not explained and remains a considerable problem for this mechanism. Furthermore, the role of these metallic particles in crystal nucleation is not explicitly discussed. The theory presented by Nardone and Karpov is highly speculative and as such would require a great deal of

experimental work in order to be considered as a feasible alternative to describe crystal formation in NPLIN experiments.

1.4.6 Nucleation of bubbles

Using low power laser pulses of comparable energies to those used in NPLIN experiments have been shown to cause bubble nucleation in carbonated water.[79] Knott et al. measured the laser power threshold for bubble nucleation which was recorded as a function of supersaturation: see Figure 1.13.

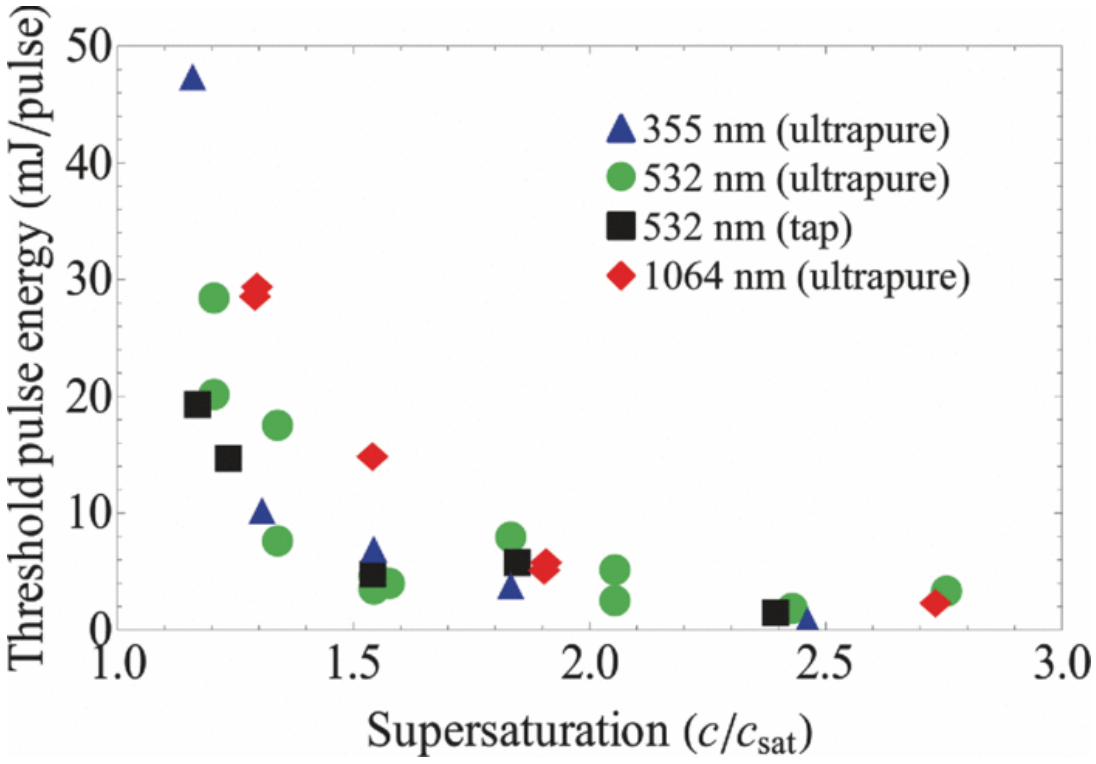

Figure 1.13 Plot taken from Knott et al. showing the supersaturation dependence of the observed threshold laser pulse energy required to cause bubble formation in samples of carbonated water.[79] The data shows the threshold pulse energy is wavelength dependent and that there appears to be no systematic difference in the threshold pulses energy required for samples prepared using ultrapure (green circles) or municipal tap water (black squares). Source of tap water was Santa Barbara, California.

The results indicate that there is a threshold laser power required for bubble formation as is seen for crystal nucleation in studies of NPLIN. Samples prepared at a given level of CO_2 supersaturation were shot ten times with the laser (355, 532 or

1064 nm), if no bubbles were produced, the laser power was increased and shot again, this process was repeated until at least one bubble was seen during the ten shots; the power at which this occurred was deemed the threshold power. NPLIN studies on halide salts (see Section 2.3) suggest that a common threshold power is obtained for a given system regardless of supersaturation; however the threshold obtained by Knott et al. is seen to vary with the level of supersaturation. Interestingly, (unsure if filtered or un-filtered); no significant difference was observed when samples of ultrapure water were directly compared to samples prepared using tap-water, suggesting that the threshold is not susceptible to levels of trace impurities.

In a second set of experiments, the water sample was co-supersaturated with glycine solute and argon gas resulting in a system estimated to have a glycine supersaturation of $S = 1.25$ and an argon supersaturation of $S = 4.5$. These samples were carefully vented to the atmosphere and resealed before shaking that resulted in many bubbles being produced. Shortly afterwards, glycine crystals were seen falling to the bottom of the sample vessel indicating that bubble formation in supersaturated solutions can result in crystal nucleation. Control experiments were also carried out;

I. Sample not vented to atmosphere before shaking (not supersaturated with respect to argon)
II. Sample prepared with no argon gas (glycine aqueous solution).

In both cases, no bubbles were produced by shaking the sample, and no crystallization was observed. The authors note that the number of bubbles produced increases with laser power above the threshold and suggest that bubble formation may be responsible for nucleation in NPLIN studies. The direct dissolution of co-solute gas used by Knott et al. clearly favours bubble formation; however, the mechanism for bubble formation in samples prepared in previous studies of NPLIN is not clear. The laser powers used in NPLIN experiments are not high enough to cause cavitation (~10^2 GW cm^{-2}, nanosecond pulse) of the solvent (water).[80] Transient heating of sample impurities by the laser might cause bubble formation. Comparison with tap water shows no change in the threshold power for laser-induced bubble formation; however, a more rigorous study involving contaminants of known composition and concentration would be required to provide a clearer picture of the

possible role that impurities play in laser-induced bubble formation and possibly in NPLIN.

1.4.7 Polarization of pre-nucleated clusters

Recently Alexander and co-workers have demonstrated NPLIN in a range of metastable systems, paying particular attention to the aqueous potassium chloride (KCl). Their initial work investigated the NPLIN of KCl from supersaturated solution (S = 1.05–1.10).[55] Contrary to the previous work of Garetz et al.[52,56-61,81,82] it was found that a single pulse of laser light (pulse width = 7 ns, 1064 nm) was sufficient to cause nucleation. For all supersaturations, a linear relationship between probability of nucleation and incident peak power density was found, along with a common threshold of ~6.4 MW cm^{-2}: significantly lower than the values reported for small organic molecules such as urea (40 MW cm^{-2}).[57]

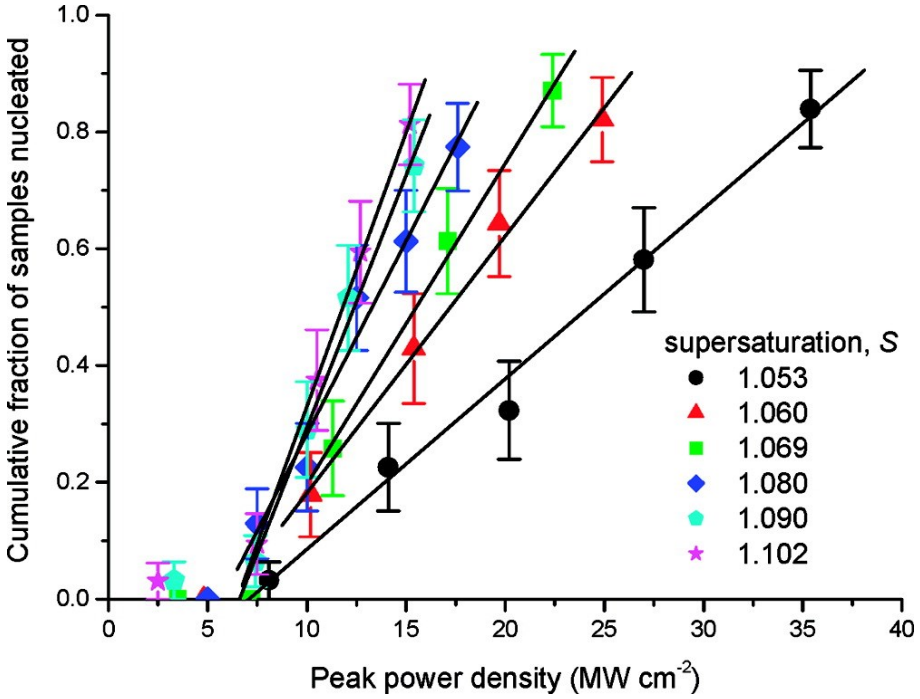

Figure 1.14 Plot taken from Alexander and Camp[55] showing the experimentally determined peak power density dependence of the fraction of samples nucleated in single-pulse NPLIN experiments. The different points (see key, above) represent solutions of differing supersaturation in the range (S = 1.053–1.102). The black lines represent least-squares linear fit of the data points which were used to extract a common threshold power density value of ~ 6.4 ± 0.5 MW cm^{-2}.

The effect of laser polarization was tested, with no difference on the probability of nucleation observed when using linearly or circularly polarized pulses. KCl crystallizes in a cubic space group, and therefore does not have a preferentially polarizable axis to be aligned with an applied electric-field as required for the OKE mechanism. Instead the authors proposed an alternative mechanism based on the isotropic electronic polarization of pre-nucleated clusters in solution. The isotropic polarization (IP) model relies upon the reduction in free energy that a dielectric particle experiences in the presence of an electric field. Considering pre-nucleated solute clusters as solid dielectric particles, the change in free energy of a cluster in presence of an applied electric field E can be calculated by Equation 1.7.[55]

$$\Delta W(E) = -aV_{\mathrm{p}}E^2 \tag{1.7}$$

where V_{p} is the volume of the dielectric particle and a is a parameter defined by the relative permittivities of the solid (ε_{S}) and liquid (ε_{L}) components and is given by Equation 1.8.[83]

$$a = \frac{3\varepsilon_0\varepsilon_{\mathrm{L}}}{2}\left(\frac{\varepsilon_{\mathrm{S}} - \varepsilon_{\mathrm{L}}}{\varepsilon_{\mathrm{S}} + 2\varepsilon_{\mathrm{L}}}\right) \tag{1.8}$$

In classical nucleation theory, the free energy change for formation of a spherical cluster of radius r in zero-field can be written as

$$\Delta G(r, 0) = 4\pi r^2\gamma - \frac{4}{3}\pi r^3 A \ln S \tag{1.9}$$

where γ is the crystal–solution interfacial tension; S is the supersaturation; and $A = \rho RT/M$, where ρ is the mass density and M is the molar mass of the solid. In the presence of an electric field, this expression is modified by an electrostatic contribution (Equation 1.7) to provide the following expression

$$\Delta G(r, E) = 4\pi r^2\gamma - \frac{4}{3}\pi r^3(A \ln S + aE^2) \tag{1.10}$$

This modification results in a lowering of the free energy barrier to nucleation, resulting in a critical cluster radius $r_{\mathrm{c}}(E)$ given by

$$r_c(E) = \frac{2\gamma}{(A \ln S + aE^2)} \tag{1.11}$$

It can be seen that the critical radius is reduced by the presence of the field, i.e., $r_{\mathrm{c}}(E) < r_{\mathrm{c}}(0)$. The outcome of the free energy reduction is shown schematically in

Figure 1.15. It can be seen that there is a population of sub-critical clusters in zero-field that would become critical in an applied field.

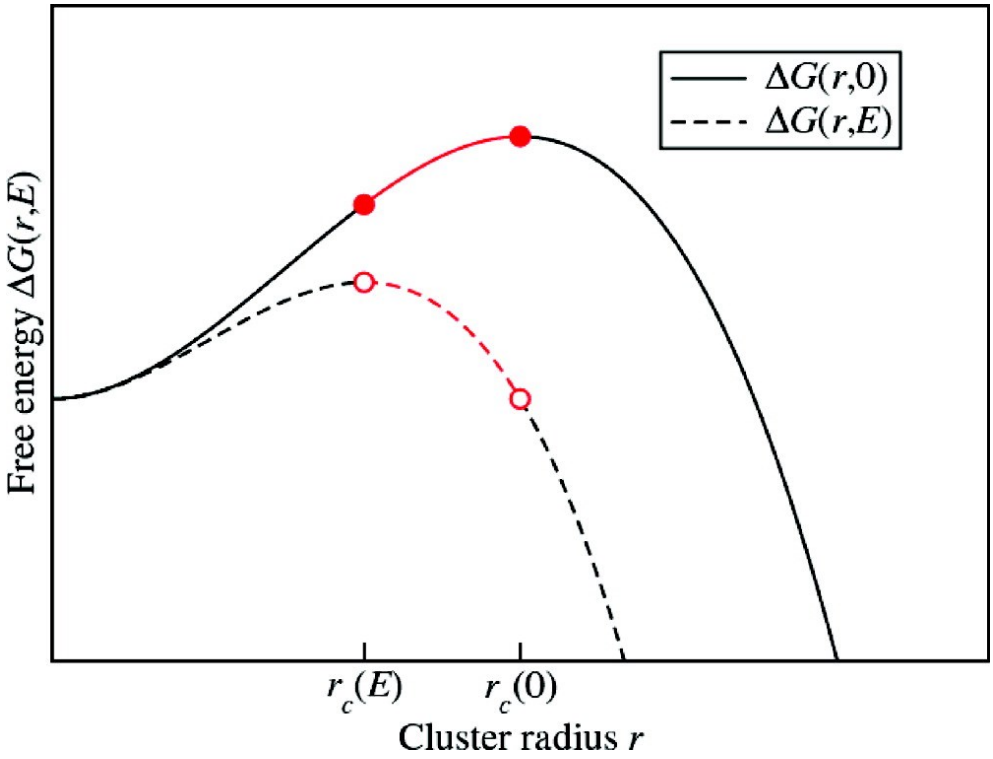

Figure 1.15 Schematic diagram from ref. 55 showing the effect of an applied electric field on the classical free energy barrier to nucleation.[55] The solid curve represents the free energy barrier to nucleation of a dielectric particle with permittivity greater than the surrounding medium in zero-field. The dashed line represents the free energy barrier to nucleation for the same particle in an electric field of magnitude *E*. The field acts to lower the classical barrier height and simultaneously reducing the critical cluster size. Highlighted in red is the population of clusters with radii in the range $r_c(E) \leq r \leq r_c(0)$ that are subcritical in zero-field which become supercritical in the applied field.

To model their data, Alexander and Camp calculated the fraction, f, of solute clusters that become critical in the applied field through the following expression,

$$f = \left\{ \int_{r_c(E)}^{r_c(0)} \exp[-\Delta G(r,0)/k_B T]\, dr \right\} \times \left\{ \int_{0}^{r_c(0)} \exp[-\Delta G(r,0)/k_B T]\, dr \right\}^{-1} \quad (1.12)$$

where the integral limits are those identified in Figure 1.15, and the function $\Delta G(r,0)$ is given by Equation 1.9.

The IP model of Alexander & Camp predicts a linearly increasing probability of nucleation with increasing electric field strength from $E = 0$, i.e., with no threshold

power. The experimental data do show a linear relationship with peak power density; however they also clearly show a non-zero threshold power. Alexander and Camp used the model to predict the slope of the power dependency of NPLIN; the modelled data was artificially shifted along the *x*-axis by the value of the experimentally obtained threshold power density value. As shown in Figure 1.16, their resulting model values are able to represent the experimental data reasonably well as a function of supersaturation and laser power. The resulting fit of the experimental data provided a phenomological value of $\gamma = 2.19 \pm 0.03$ mJ m^{-3}; in good agreement with literature values.

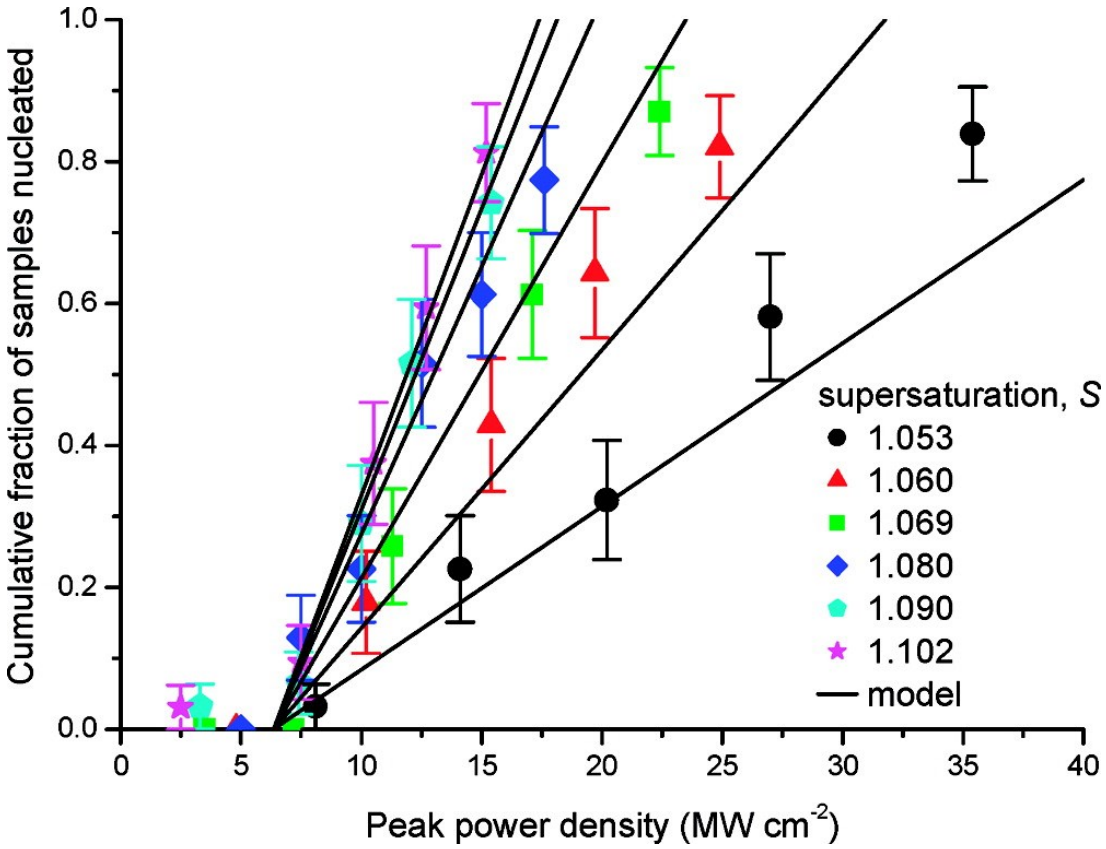

Figure 1.16 Results from Alexander and Camp[55] where the points represent the experimental data at different supersaturations, $S = 1.053$ (circles), 1.060 (triangles), 1.069 (squares), 1.080 (diamond), 1.090 (pentagons) and 1.102 (stars). The lines were obtained using the model predicted slope, but were shifted along the *x*-axis to match the experimentally determined mean threshold power density (6.4 MW cm^{-2}).

The IP model gives no insight as to why a non-zero threshold power is observed in experiment. It is expected that the apparent threshold value is a result of

the mechanism responsible for NPLIN. They consider internal structural rearrangement of the nucleus as a crucial feature of the mechanism, the exact details of which may lead to an explanation of the observed threshold. In addition, the authors highlight the fact that their model is classical and therefore is subject to the same shortcomings as CNT. It may be the case that future improvements to the model will provide a theoretical account of the threshold power for NPLIN.

Although the IP model does an excellent job of reproducing the experimental data, Alexander and Camp acknowledge that their model suffers from a similar problem to Garetz's OKE hypothesis: that is the electrostatic reduction in free energy in the applied field (Equation 1.7) is significantly lower than the classical barrier height. To account for this, the authors speculate NPLIN may be promoted by impurity particles, either through favourable interaction with solute clusters to increase the electrostatic contribution (ΔW) or by reducing the overall interfacial energy, which would see the classical barrier height reduced. Noting the differences between the characteristic laser powers required for NPLIN of different system types, i.e., small organic molecules and simple salt solutions, Alexander and Camp suggest that the OKE and IP mechanisms may complement one another by operating more effectively under different power regimes.

1.5 NPLIN in single component systems

A review of the available literature finds that accounts of NPLIN have almost exclusively been reported in 2-component solid–liquid systems, i.e., solute dissolved in solvent. It is becoming increasingly clear that a theoretical approach may help to elucidate the NPLIN mechanism and to provide an insight in to nucleation in general. Theoretical study of multi-component systems is complicated by the additional solvent–solvent and solute–solvent interactions that must be calculated. With the aim of providing experimental results to promote further theoretical study, Alexander and co-workers have demonstrated NPLIN in the single-component systems of glacial acetic acid (GAA) and molten sodium chlorate ($NaClO_3$). To achieve the metastable state, both samples were supercooled below their melting point (T_m) before exposing to the laser.

1.5.1 Glacial acetic acid

The NPLIN of GAA has recently been reported by Ward et al.[84] Samples of GAA cooled to –9 °C (T_m = 16.6 °C) were exposed to trains of 1064 nm pulses with pulse repetition rate of 10 Hz for a maximum of 10 seconds. In this case, nucleation was easily identified due to the rapid (< 1 s) solidification of the sample upon freezing. A plot of the power dependence of nucleation shows features common to others, namely a low power threshold (9.0 ± 4.2 MW cm^{-2}) and linear region at low power densities. However, the observed fraction of samples nucleated appears to reach an upper limit of $f = 0.74 \pm 0.24$, which is seen across a wide range of power density (~200–900 MW cm^{-2}).

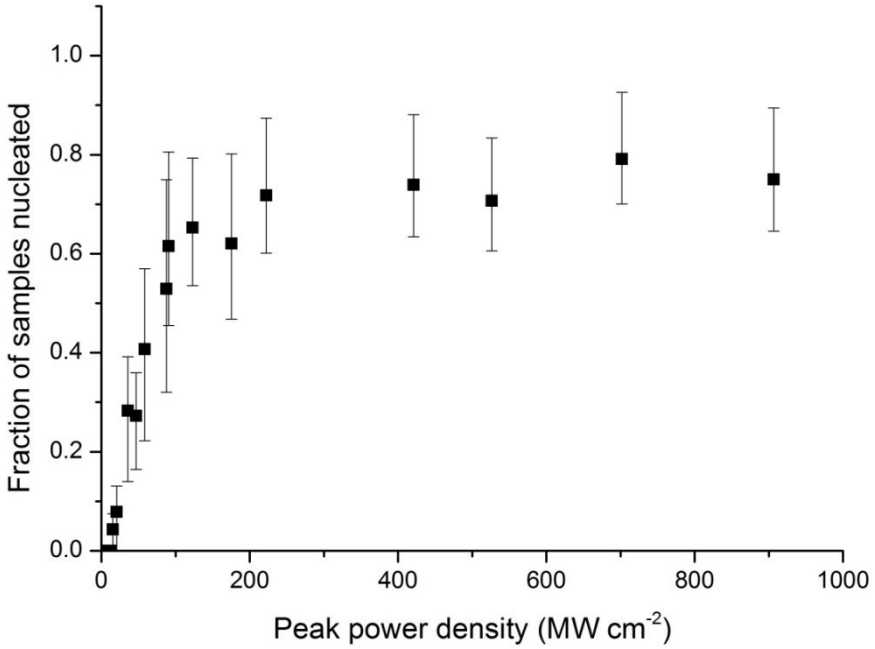

Figure 1.17 Plot of the fraction of samples nucleated *versus* peak laser power density obtained by Ward et al.[84] for NPLIN of supercooled glacial acetic acid (GAA). Confidence intervals were obtained using the Wilson method for binomial distributions.[85] At low power density the data points follow an approximately linear relationship providing a threshold power density of 9.4 ±4.2 MW cm^{-2}. At higher power density the data approach an upper limit of $f = 0.75 \pm 0.24$.

The upper limit was attributed to sample heating, which becomes a significant quantity at higher laser powers. When the crystal structure of GAA was considered, it was found that its symmetry was incommensurate with the OKE mechanism of

NPLIN; the most polarizable molecular axes are arranged orthogonally, thus there is no preferred axis to be aligned with an applied field.

Ward et al. obtained a value of the crystal–solution interfacial tension of $\gamma = 15.5$ mJ m^{-2} by analysing the data using their model based on the isotropic polarization of pre-nucleated clusters; this value is in good agreement with the value at –9 °C (γ = 32.5 mJ m^{-2}), estimated using Digilov's semi-empirical approach.[86] Gavezzotti et al. have carried out molecular dynamics simulations of melting GAA[87] and provide evidence for disordered, loosely associated clusters as precursors for nucleation. Ward et al. suggest that the stabilization afforded by the laser field allows the cluster(s) to find a lower energy configuration on the complex potential energy surface where activation occurs. Although the results are explained in terms of NPLIN by a homogeneous nucleation mechanism, the authors highlight the fact that impurity particles have been considered as a cause for this effect. It is suggested that NPLIN could occur at the surface of solid nanoimpurity particles with higher dielectric constant than the surrounding liquid; however, if this is the case it is unclear why some systems appear resistant to NPLIN, since impurities might be expected to be more prevalent.

1.5.2 Molten sodium chlorate

The potential role of impurity particles has been identified by Alexander and co-workers in their study of NPLIN in supercooled samples of molten $NaClO_3$.[88,89] In crystalline form, achiral $NaClO_3$ units are arranged in a chiral space group forming either left or right handed forms, termed *l*-$NaClO_3$ and *d*-$NaClO_3$ respectively. These different enantiomorphs are optically active; the crystals can be distinguished by the opposing directions that they rotate the angle of plane polarized light. The laser power dependence of NPLIN in the melt was investigated and revealed a threshold value of 0.161 GW cm^{-2}:[89] much greater than the thresholds observed for KCl and GAA. The data show a linear relationship at low power densities, however the point at the highest power density tested (~0.235 GW cm^{-2}) indicates a plateau around $f \approx 0.75$.

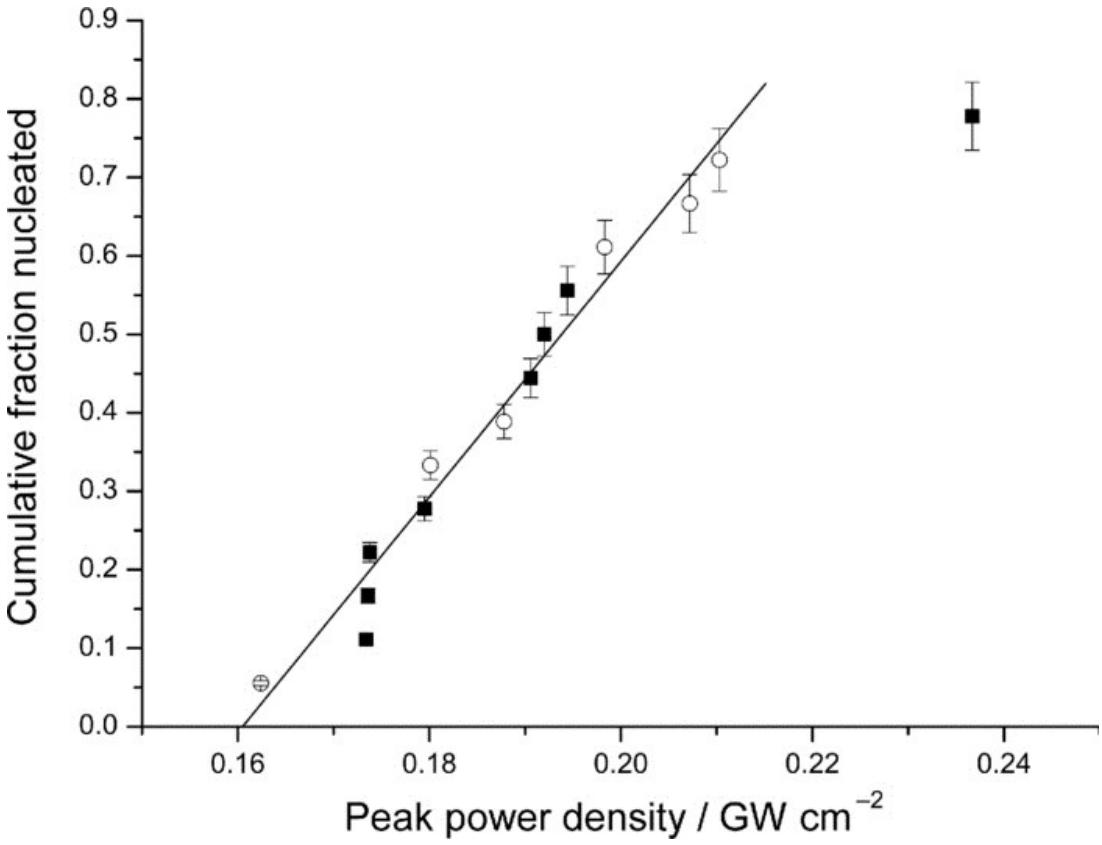

Figure 1.18 Plot showing the cumulative fraction of samples nucleated by NPLIN of molten sodium chlorate pulses of wavelength λ = 1064 nm.[89] Solid squares and open circles represent samples nucleated with linearly and circularly polarized light, respectively. The solid line represents a least-squares linear fit of the first 13 points to obtain the threshold value of 0.161 GW cm^{-2}. The final point near peak power density of 0.24 GW cm^{-2} suggests an upper limit of $f \approx 0.75$.

Initial experiments using single crystals, prepared in advance, of known chirality showed a remarkable memory of chirality with 20 of the 23 samples shot forming the same enantiomorph used to prepare the starting sample. This behaviour was initially thought to be due to contamination of the sample with airborne dust that allows some of the solid to resist melting. To explore this, 2 additional sets of experiments were carried out. Firstly samples were prepared using freshly recrystallized material of known chirality and shot as before; secondly, samples of freshly recrystallized material were crushed to provide an enantiopure powder. When samples of freshly prepared crystals were melted and exposed to the laser, no nucleation was seen. However, the crushed samples were readily nucleated and demonstrated a strong memory of chirality with 11 from the 14 samples shot

recrystallizing in the initial crystal form. Rather than implicating airborne dust as the cause of this effect, as expected, it was established that the act of crushing the solid promoted NPLIN. Begg et al., while investigating the thermal decomposition of $NaClO_3$, observed mass losses of 0.1%–1%; consistent with the loss of oxygen to form sodium chloride (NaCl).[90] Alexander and co-workers suggest that during the crushing, heating and ageing process involved in sample preparation, trace amounts of NaCl impurity are formed which would be able to survive the melting process for $NaClO_3$ (T_m = 262 °C) due to its higher melting point (T_m = 801 °C). These impurities may act as a substrate upon which some $NaClO_3$ solid could avoid melting, even at 20 °C above its melting point. To test this hypothesis, a final set of experiments were performed where samples were prepared using single crystals of one enantiomorph and crushed crystals of the other enantiomorph in a 1:1 ratio by mass. Of the 12 samples prepared, 10 nucleated by the laser to yield the same enantiomorph as the crushed component in the starting mixture. This finding is consistent with the hypothesis that NaCl particles can harbour $NaClO_3$ during the melting process.

Similar to the case of GAA, it was shown that the crystal structure of $NaClO_3$ is not compatible with the uniaxial alignment promoted by the OKE. In their discussion, Alexander and co-workers consider a heterogeneous model for NPLIN in which impurity particles (NaCl) provide sites where $NaClO_3$ can avoid melting. When subject to the laser pulse, these protected sites are activated (in a manner analogous to NPLIN of clusters in solution) and nucleation proceeds to produce the same enantiomer as the retained solid. In this case, the homogeneous formation of a spherical cluster of radius r in the presence of an electric field of magnitude E is described using Equation 1.13.

$$\Delta G_{\mathrm{hom}}(r, E) = 4\pi r^2\gamma - \frac{4}{3}\pi r^3(B\Delta T_{-} + aE^2). \qquad (1.13)$$

Here, γ is the crystal–melt interfacial tension, $\Delta T_{-} = T_m - T > 0$ is the degree of supercooling below the melting point T_m, and B is a parameter defined by physical properties of the material, such as the heat of fusion ΔH_{fus}. The free energy for formation of a cluster in contact with a surface (ΔG_{het}) is obtained by including a wetting factor $f(\theta)$, as first derived by Volmer.[91]

Then we have $\Delta G_{\text{het}} = f(\theta)\Delta G_{\text{hom}}$, where

$$f(\theta) = \frac{1}{4}(2 + \cos\theta)(1 - \cos\theta)^2 \quad (1.14)$$

and θ is the contact angle between the cluster and surface of the impurity particle. A substrate–cluster contact angle of $\theta = 5.98 \pm 0.01°$ obtained following analysis of the experimental data using this heterogeneous model of NPLIN. The result was found to be in excellent agreement with the value calculated using the Turnbull model of heterogeneous nucleation in cylindrical cavities, $\theta \approx 3.17°$.[92]

The studies of NPLIN in single component systems demonstrate that the model for NPLIN proposed by Alexander and Camp is capable of reproducing the experimental data for both homogeneous and heterogeneous nucleation. However, the possibility of impurity particles playing a role in NPLIN cannot yet be ruled in or out. Further work is required in order to probe this crucial question.

1.6 Thesis structure

The subsequent Chapters of this Thesis present different series of experimental work carried out during my PhD. A brief outline and the main objectives of these Chapters are listed below;

Chapter 2: *Non-photochemical laser-induced nucleation of potassium halides: effects of wavelength and temperature*.

Previous work in the area has highlighted the need for more experimental data in order to help develop and test models of NPLIN. With a view to providing such data, NPLIN of potassium chloride (KCl) and bromide (KBr) in supersaturated aqueous solution was studied and the effects of wavelength and temperature investigated. The results were analysed using the IP model of nucleation.

Chapter 3: *Non-photochemical nucleation of potassium chloride induced by an evanescent wave.*

NPLIN has provided a unique degree of spatial (within ~0.1 cm^3) and temporal (~10^{-9} s) control over crystal nucleation. However, in order to allow direct and *in situ* studies of nucleation an even greater level of spatial control is required.

With the aim of providing such a technique, the novel use of an evanescent wave as a means of causing nucleation in supersaturated aqueous potassium chloride solution was investigated. Due to the short penetration depth of the evanescent field, nucleation was successfully confined to a volume five orders of magnitude less than that of a typical NPLIN experiment.

Chapter 4: *Rayleigh scattering in concentrated salt solutions: An investigation of solution structure.*

Evidence in support of the two-step model (2SM) of nucleation is growing, though the majority of which is indirect. The most convincing evidence to date has been provided by laser scattering experiments, however, the nature of the identified particles has not been scrutinized. With a view to investigating the nature of the particles (i.e., impurities, nanobubbles or solute clusters) a wide range of aqueous solute systems were investigated using Rayleigh laser scattering. In addition to identifying particles in solution, estimates of the size distribution of the particle population in solution was made.

Chapter 5: *Second-harmonic scattering in aqueous urea solutions: evidence for solute clusters?*

It is becoming evident that in most solutions investigated by light scattering techniques that there exists a population of particles on the nano-scale; however, fundamental knowledge of the structure and composition of these particles remains unknown. Assuming that the particles in question are solute clusters, key questions raised are: what is the internal structure of a typical cluster? Are solute clusters completely disordered, or do they contain an ordered (e.g., crystalline) component? With the aim of investigating this, a series of second-harmonic scattering (SHS) experiments were performed in which aqueous urea solutions were subject to 800 nm laser light and any emitted light of 400 nm was detected. Experiments were carried out as a function of solute concentration with samples ranging from supersaturation of $S = 0.15–1.86$.

Chapter 2: Non-photochemical laser-induced nucleation of potassium halides: effects of wavelength and temperature

2.1 Introduction

Crystallization of a desired product from liquid solution is a ubiquitous phase transition which has been exploited in industry and the sciences primarily as an efficient means of product separation and purification. Although crystallization is a commonly used technique, we still know remarkably very little about how and why nucleation occurs. The limiting factor of our knowledge in this area is due, mostly, to the stochastic nature of the process and the associated difficulties in its study. Non-photochemical laser-induced nucleation (NPLIN) has been demonstrated recently as a technique capable of overcoming these significant difficulties. In NPLIN, the nucleation event has been demonstrated to occur within the pulse duration of the incident laser pulse, and is confined to within the irradiated volume.[55,52,54] This unique degree of control makes NPLIN the perfect technique to use in the study of the nucleation process.

To date, NPLIN studies have led to the proposal of two main mechanisms in order to explain the experimental observations; OKE and IP (see Section 1.4). Neither of these mechanisms can yet be confirmed or discounted. In order to expand our knowledge of nucleation in NPLIN it is evident that more data must be generated in order to test the current models and theories. Moreover, it is hoped that the provision of new studies will stimulate much-needed theoretical and computational interest in the area. With this aim in mind, the effects of temperature, laser intensity, wavelength and anion (Br^- versus Cl^-) on NPLIN were investigated; the findings have been published elsewhere,[93] and are reported and discussed in the remainder of this chapter.

2.2 Experimental

Supersaturated solutions were prepared by dissolution of KCl (puriss, >99%, Fluka) and KBr (puriss, Sigma) in deionized water (Chromanorm HPLC grade, VWR). The saturation concentrations (c_0) of KCl and KBr in aqueous solution at a temperature of 23 °C are 4.688 and 5.610 mol kg^{-1}, respectively.[94] Solutions were prepared to have a supersaturation of $S = c/c_0$ = 1.060. The stock solutions were syringe-filtered whilst warm (0.22 μm, Millex-GP) into clean cylindrical glass vials (20.3 mm diameter) with screw-caps. Each vial was filled with approximately 3.8 cm^3 of sample solution. The vials used were cleaned thoroughly using concentrated detergent and rinsed several times, with the final rinse carried out using syringe-filtered deionized water. In total approximately 20 sample vials were prepared for each sample solution.

All samples were intentionally crystallized prior to undergoing a heating, cooling, and irradiation cycle. Nucleated samples were regenerated by gentle heating on a hot plate (50 °C) with regular shaking followed by a brief ultrasonication in a water bath (40 °C). Dissolved samples were then cooled to the experimental temperature by placing in a temperature-controlled water bath (23.0 °C) for a period of 40 minutes. We have observed that samples that do not nucleate during the 40 minute cooling period are stable for days or weeks. Once cooled, samples were removed from the water bath and placed centrally in the beam path where the sample was exposed to a single pulse of laser light with wavelength of 532 or 1064 nm (Brilliant, Nd^{3+}:YAG, Quantel).

The linearly polarized laser light was passed through an iris (5.5 mm diameter) and then through a Glan-laser polarizer before reaching the sample. The polarizer provides a fine control over the pulse energy incident upon the sample and ensures purity of the final linear polarization. The mean laser power of the beam was measured with the laser running at 10 Hz after passing through the polarizer using a power meter (Nova, Ophir) and the value was converted to peak power density (j_{peak}) by taking in to account the duration of the laser pulse (5.3 ns at 532 nm and 6.3 ns at 1064 nm) and the area of the beam at the exit of the vial. The glass vial acts as a cylindrical lens, slightly focussing the beam in the horizontal direction. Optical ray-tracing methods were applied to calculate the beam area at the vial exit. The

resulting area of the pulse at the vial exit depends on the refractive index of the sample solution at the experimental temperature and the incident wavelength of light. With an input pulse area of 0.24 cm^2, for all samples, we calculate an approximate pulse area at the vial exit of ~0.11 cm^2. Samples were exposed to peak power densities in the range of 5–42 MW cm^{-2} (equal to approximately 3–30 mJ $pulse^{-1}$, depending on wavelength). Immediately after being shot with a single pulse, samples were returned to the temperature controlled water bath. After a period of 15 minutes, the samples were inspected and the number of vials showing crystals were counted (n); the fraction of samples nucleated ($f = n/N$) was calculated from the total number of samples shot (N).

In order to investigate the effects of temperature, the nucleation of samples of KCl prepared with $S = 1.060$ at 33 °C was compared directly to the nucleation of samples with equal S at 23 °C achieved using 1064 nm irradiation. Sample vials were prepared in the same way as outlined above, using the saturation concentration of aqueous KCl at 33 °C as 5.092 mol kg^{-1}.[94] In order to maintain the sample temperature at 33 °C during the shooting process, a custom brass heating block was manufactured. The block was maintained at the desired temperature using ceramic heating cartridges and a programmable heating controller (2132, Eurotherm). Each sample was seated in the block for 60 seconds prior to exposing to a single pulse of linearly polarized, 1064 nm light. After shooting, the sample was then immediately returned to the 33 °C water bath. The fraction of samples which nucleated, f, was counted 15 minutes after shooting. Samples were shot with different laser peak power densities in the range 9–20 MW cm^{-2}.

2.3 Results

Plots of the fractions of samples nucleated (f) versus peak power density (j_{peak}) for KCl and KBr solutions using 532 and 1064 nm wavelength laser light are shown in Figure (2.1a and 2.1b).

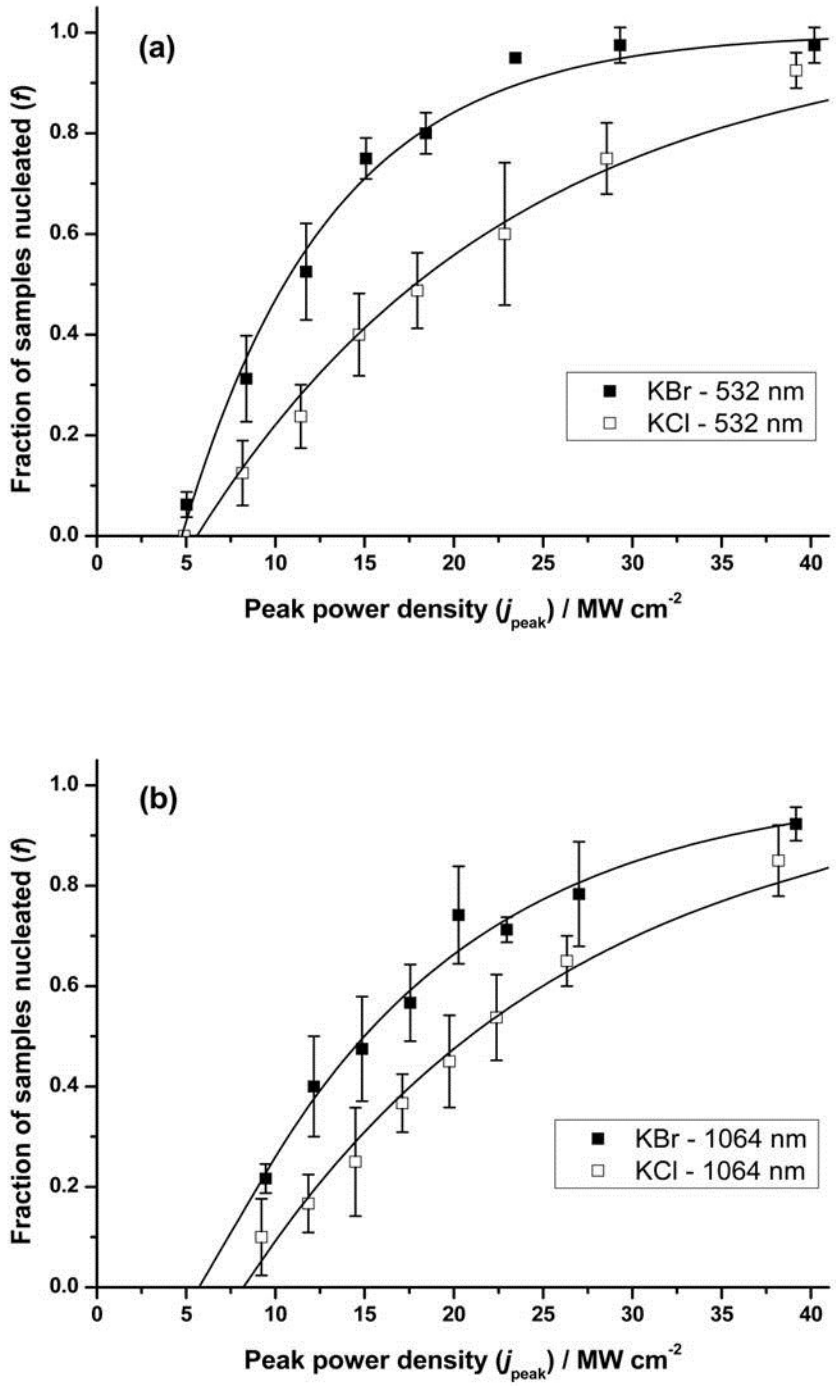

Figure 2.1 Plots of the peak power dependence of the fraction of samples nucleated measured for supersaturated solutions (S = 1.06) of KCl (open squares) and KBr (closed squares) when exposed to single pulses of (a) 532 nm and (b) 1064 nm pulses. Error bars represent single standard deviations from 4 repeat measurements on 20 samples. Poisson model fits to the data are shown by solid lines; sample labilities and thresholds obtained are shown in Table 2.1.

The obtained data display features common to other reports of NPLIN.[52,55-57] It can be seen that at low powers, the data follow an approximately linear relationship. The slope represents how labile a certain set of samples are to nucleation; we will from here on refer to the magnitude of this slope as the sample *lability*. All of the data sets show a low power threshold, below which no nucleation is seen. At higher incident power densities it can be seen that the data begin to approach a plateau near $f = 1$. This type of behaviour initially suggests a non-linear process that becomes apparent at higher power density. However, it must be noted that in these experiments *we count the number of samples nucleated, not the number of nuclei formed*. Consequently we are observing the probability of forming one or more nuclei after shooting. A linear fitting scheme is not appropriate here and in order to fit the data a Poisson function is used. The probability $p(n)$ of observing exactly n nuclei is given by the Poisson distribution, as shown by Equation 2.1,

$$p(n) = \frac{\lambda^n \mathrm{e}^{-\lambda}}{n!} \tag{2.1}$$

where λ is the mean number of nuclei expected at a given laser power density. Since the total probability sums to unity, the probability of obtaining *at least* 1 nucleus can be written as 1 minus the probability of obtaining *no* nuclei,

$$p(n \geq 1) = 1 - p(0) = 1 - \mathrm{e}^{-\lambda} \tag{2.2}$$

For the IP nucleation model of NPLIN, it has been shown that the mean number of nuclei depends linearly on peak laser power density, $\lambda = m(j_{\mathrm{peak}} - j_0)$, where j_0 is the threshold power and m is the sample lability.[93] The resulting function that is used to fit the experimental fraction of samples nucleated is shown by Equation 2.3.

$$f(j_{peak}) = 1 - \exp\left[-m(j_{peak} - j_0)\right] \tag{2.3}$$

The values of the parameters obtained through a least-squares fitting process using Equation 2.3 are summarized in Table 2.1.

Temp / °C	Wavelength (λ) / nm	Solute	Threshold peak power density (j_0) / MW cm^{-2}	Lability (m) / cm^2 MW^{-1}
23	532	KBr	4.8 ± 0.3	0.121 ± 0.009
23	532	KCl	5.6 ± 0.5	0.057 ± 0.004
23	1064	KBr	6.2 ± 0.7	0.079 ± 0.006
23	1064	KCl	8.2 ± 0.5	0.055 ± 0.003
33	1064	KCl	7.7 ± 1.1	0.115 ± 0.025

Table 2.1 Threshold peak power densities (j_0) and sample labilities (m) for NLIN of supersaturated (S = 1.06) aqueous KCl and KBr samples. The parameters were obtained by fitting the data shown in Figures 2.1 (a) and 2.1 (b) using Equation 2.3.

The results show that 532 nm pulses are more effective at inducing nucleation in both sets of samples compared to the use of 1064 nm light. This is reflected in the lower peak power density threshold and higher lability values obtained for both KCl and KBr solutions. In addition, the results show that it is easier to nucleate the solution of KBr than it is the solution of KCl under equivalent conditions. We find lower threshold values and higher labilities for KBr samples when shot with 532 and 1064 nm pulses. The value of threshold power reported here (8.2 ± 0.5 MW cm^{-2}) for KCl using single pulses of 1064 nm light is higher than that previously reported by Alexander and Camp (6.4 ± 0.5 MW cm^{-2}).[55] This difference can be attributed to the Poisson fitting procedure used in this work, compared to the linear fitting scheme employed in the previous work.

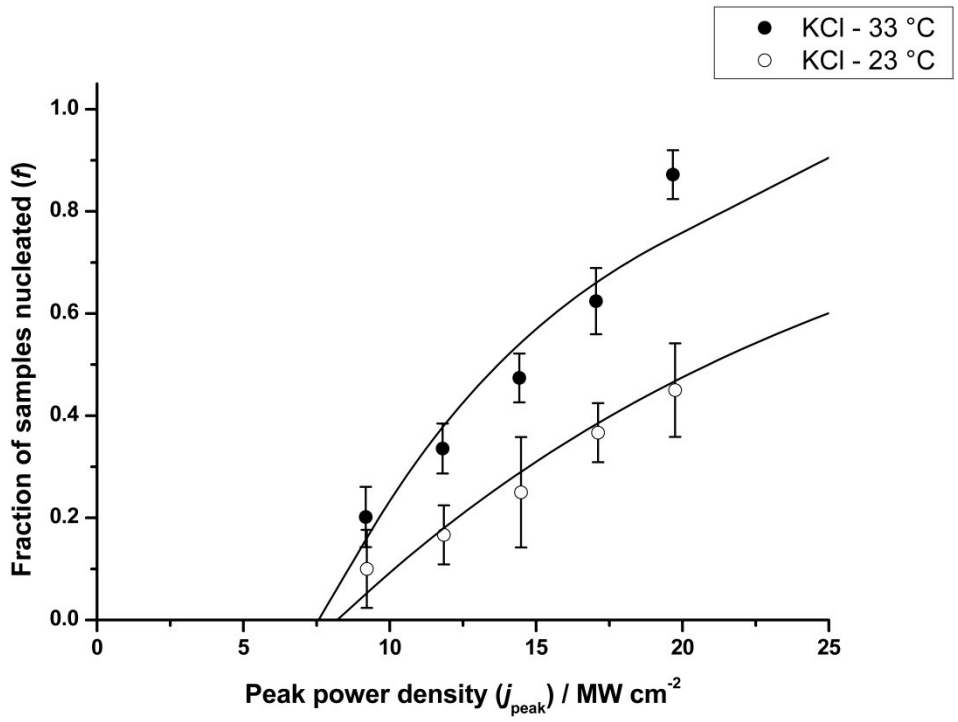

Figure 2.2 Plots of the peak power dependence of the fraction of samples nucleated versus peak power density for aqueous KCl at temperatures of (open circles) 23 °C and (closed circles) 33 °C. Both sets of samples were prepared to have identical supersaturation (S = 1.06) at the respective temperatures. Poisson function fits to the data are shown by solid lines; sample labilities and thresholds obtained are shown in Table 2.1.

Plots of the fraction of KCl samples nucleated versus peak power density for identical supersaturations (S = 1.060) at 23 and 33 °C are shown in Figure 2.2. The data show that the samples at 33 °C are significantly more labile to nucleation than those at 23 °C. Over the power range investigated, we see the ratio of the sample labilities obtained for samples nucleated at 33 °C to those at 23 °C is 2.11 ± 0.47. The fitted threshold values are very similar suggesting that both data sets may share a common threshold peak power density value.

2.4 Discussion

2.4.1 Possible effect of sample heating

The results demonstrate a greater likelihood of nucleation occurring in supersaturated solutions of potassium chloride and bromide when using 532 nm laser pulses than with 1064 nm pulses. This trend is demonstrated by a lower threshold

peak power density and a higher lability value when using 532 nm pulses. This wavelength dependence has been documented in previous studies of glycine and urea, with the observed differences in nucleation probability attributed to heating due to absorption of light by the sample.[57,60] In those studies, samples were exposed to trains of 10 s of pulses each; however in the present work, samples were exposed only to a single pulse. Using a method outlined in previous work the amount by which a bulk sample is heated by absorption of light can be estimated.[53] For KBr, heating within the illuminated volume is estimated to be ~ 6×10^{-5} °C at 532 nm and ~ 14×10^{-3} °C at 1064 nm; the values for KCl are slightly lower. These temperature increases are entirely negligible.[53] Unlike the OKE mechanism, the IP model does predict a dependence on the wavelength of light used to initiate nucleation. The free energy reduction of a pre-nucleated cluster in an applied field (E) is given by $\Delta W(E) = -aV_{\mathrm{p}}E^2$ where the factor a is a function of the relative permittivies of the cluster and the surrounding medium. The permittivities themselves are a function of the optical frequency which increases with increasing frequency. The IP model expects a greater lowering of free energy for 532 nm than 1064 nm light and therefore a greater probability of nucleation occurring; which is the trend observed experimentally.

2.4.2 Effects of ion concentration

During the course of experiments, it was consistently noted that KBr samples would produce more crystals than KCl samples at identical laser powers. At first, it was thought that this was due to the higher solute concentration in the KBr samples. At a supersaturation of $S = 1.060$, the solute concentrations were $C = 5.947$ mol kg^{-1} and 4.969 mol kg^{-1} for KBr and KCl solutions respectively. The KBr samples have 20% more solute ions than the KCl samples; however, experiment shows a far greater relative increase in sample lability between KBr and KCl samples (approximately a factor of 2 at 532 nm). As the crystalline forms of KCl and KBr share a similar, cubic rock-salt structure and ionic stoichiometry, it is unclear why we should observe such a notable difference in sample lability.

During experiments, the numbers of crystals produced per sample were counted for samples shot with mean laser power in the range 4–40 MW cm^{-2} for 532

and 1064 nm pulses. The counts showed that the mean ratios of the number of crystals produced for KBr relative to KCl were 1.30 at 1064 nm and 1.18 at 532 nm. These values are very close to the ratio of the salt concentrations used in experiment ($C_{\mathrm{KBr}}/C_{\mathrm{KCl}} = 1.20$) which suggest that the number of crystals produced is dependent on the absolute concentration of the solution.

The results of the temperature dependence show a disproportionate increase in sample lability with respect to the solute concentration. The solute concentrations used at 23 and 33 °C were 4.969 and 5.398 mol kg^{-1}, respectively. Experiments show that the solutions at 33 °C are twice as labile to nucleation as those at 23 °C, while the solute concentrations reflect only a 9% increase in the number of KCl ion pairs in solution. Although we expect the solute concentrations to have some influence on the resulting sample lability, these findings suggest that the observed lability is dependent on more than the solute concentration alone.

2.4.3 Model of experimental results

The results discussed here were analysed using an improved version of the IP model outlined in Section 1.4.7. In summary, the model is based upon the electrostatic reduction in free energy that a dielectric particle, with higher permittivity than surrounding medium, experiences in the presence of a homogeneous electric field. The free energy of such a particle (radius *r*) in an electric field of magnitude *E* can be described using Equation 2.4,

$$\Delta G(r, E) = 4\pi r^2\gamma - \frac{4}{3}\pi r^3(A \ln S + aE^2) \qquad (2.4)$$

S is the supersaturation, γ is the solute–solution interfacial tension and the parameters *A* and *a* depend on physical parameters of the solution, solution and the light used in the experiment. In the applied electric field of the laser pulse, we expect a population of clusters which are sub-critical in zero-field to become supercritical. These, now supercritical, clusters can be considered *activated* during high field as viable nuclei. This activation occurs through the isotropic electronic polarization of the clusters.

Parameter	KCl (23 °C)	KBr (23 °C)	KCl (33 °C)
Molar mass (M) 10^{-3} kg mol^{-1}	74.55	119.0	74.55
Molality (C), mol kg^{-1}	4.969	5.947	5.398
Solute mass fraction (w)	0.2703	0.4144	0.2869
Solution density (ρ_l), kg m^{-3}	1176	1375	1184
Solid density (ρ_s), kg m^{-3}	1984	2750	1984
Relative permittivity, solid (ε_s) at 532 nm	2.230	2.455	
Relative permittivity, solid (ε_s) at 1064 nm	2.189	2.384	2.188
Relative permittivity, water (ε_l) at 532 nm	1.783	1.783	
Relative permittivity, water (ε_l) at 1064 nm	1.754	1.754	1.751
Solution refractive index (n_l) at 532 nm	1.365	1.376	
Solution refractive index (n_l) at 1064 nm	1.352	1.363	1.351
Volume irradiated (V)/10^{-6} m^3 at 532 nm	0.3451	0.3424	
Volume irradiated (V)/10^{-6} m^3 at 1064 nm	0.3482	0.3455	0.3487

Table 2.2 List of parameters and their values used in the modified classical nucleation model of NPLIN used in this work. The volume of irradiated solution was calculated using a simple ray-tracing procedure to account for the slight focussing in the cylindrical sample vial; the volumes for each solution and laser wavelength differ due to differences in the solution refractive indicies.

The model used in the present work calculates the absolute number of nuclei formed in the *E*-field, in contrast to the original work of Alexander & Camp where a scaling factor was required. To calculate the number of activated nuclei, N_{nuc}, that are produced in high-field, within the irradiated volume, a Boltzmann distribution of cluster sizes is assumed (based on equation 2.4) with the model yielding the absolute number of activated nuclei produced. N_{nuc} is then used as the model value of the Poisson parameter, λ, from which model values of sample lability, m, are obtained, and the experimental data fitted. A full description of the model calculation(s) can be found in Appendix A1.

The key parameter to be determined through our model is the solute–solution interfacial tension, γ. Classically, γ is a constant whose value is dependent only upon the solute–solution system , regardless of the conditions under which the system is studied. It is expected that γ is a more complex variable that will depend on factors such as temperature and cluster size;[15,95-97] however γ ought to remain independent of

the wavelength of light used in NPLIN. The model was employed to find the value of γ that fits the experimental values of lability at 1064 nm, as shown in Table 2.3.

	Sample lability (m) / cm^2 MW^{-1}				Interfacial tension (γ) / mJ m^{-2}	
	experiment		model		model	theory
	532 nm	1064 nm	532 nm (predicted)	1064 nm (fitted)	1064 nm (fitted)	
KBr	0.121	0.079	0.083	0.079	4.817	19.52
KCl (23 °C)	0.057	0.055	0.056	0.055	5.283	24.99
KCl (33 °C)		0.115		0.115	5.429	24.90

Table 2.3 Experimental and model sample labilities of KCl and KBr for NPLIN at 532 and 1064 nm. The experimental results for 1064 nm were fitted to obtain the model value of the interfacial tension (γ) shown; the model value of γ was then used to predict the lability for 532 nm. Overall, the model is shown to correctly predict the trends with respect to wavelength and solute. Theoretical values of γ were obtained using the Mersmann equation (Equation 2.5).[98]

The strength of the model was then assessed by using the value of γ calculated for 1064 nm to calculate the lability for equivalent samples shot at 532 nm. As can be seen in Table 2.3, the model lability at 1064 nm is lower than that at 532 nm, which reproduces the experimental trend, but the model underestimates the magnitude of the difference in the case of KBr. For KCl, the model is in excellent agreement with the experimental data reproducing both the trend and the magnitude of the observed difference between samples shot with 1064 and 532 nm.

The values of interfacial tension provided by the model are 5.283 and 4.817 mJ m^{-2} at 23 °C for KCl and KBr respectively. For highly soluble salts, these values are of the expected magnitude.[99] A literature search yields a large spread of reported values (0.98–163 mJ m^{-2}) making a direct comparison difficult.[100] We can account for such a large spread due to the numerous methods employed and the diverse conditions under which these studies were carried out. However, in the studies where values for both KCl and KBr are available together, we find that γ(KCl) > γ(KBr),[99-101] in agreement with the trend we report here. For experiments carried out at 33 °C, we find γ = 5.429 mJ m^{-2} reproduces the experimental lability; this is 2.8%

greater than the value obtained at 23 °C and is similar to the ratio of the respective temperatures (306.15/296.15 = 1.034).

A theory developed by Mersmann[98] allows the calculation of γ with the knowledge of several physical parameters as shown in Equation 2.5. The expression we give here has been modified to account for a spherical clusters rather than cubic-shaped clusters discussed in the original work.[99,102]

$$\gamma = \frac{2}{6^{1/3}} k_B T \left(\frac{\rho_S N_A}{\pi M}\right)^{2/3} \ln \frac{\rho_S}{w \rho_L} \tag{2.5}$$

where k_B is the Boltzmann constant, T is temperature, ρ_S and ρ_L are the densities of the solid and solution, N_A is Avogadro's number, M is the molar mass of the solute and w is the mass fraction of the solute in the solution. Theoretical values of γ were calculated by evaluating Equation 2.5 using parameter values for a saturated solution, and are found to be a factor of 4–5 times larger than the IP model values, as shown in Table 2.3. Experimentally we find a higher value of solute–solution interfacial tension at 33 °C than at 23 °C, however this is not the trend expected from theory. Although Equation 2.5 explicitly shows $\gamma \propto T$, the relationship is more complex with other terms in the expression dependent on concentration and temperature. The current iteration of the model remains rather simple, relying on a series of physical parameters to provide its output. In spite of this, the model accounts incredibly well for the experimental data. Perhaps more significant is that the model relies heavily upon a single term, the solute–solution interfacial tension in calculations. As in the classical picture γ here is treated as a constant value for a given system, however, recent studies[15,95,96] indicate that the interfacial tension is dependent on factors such as cluster size and structure, parameters that the current model does not account for.

2.4.4 Mechanism for NPLIN

To explain NPLIN in the systems studied here we refer to the two-step nucleation mechanism and consider the following process (see Figure 2.3): (1) the supersaturated solution matures to form a population of solute clusters, with a distribution of sizes and structures; (2) while the electric field is present, a particular cluster can reorganize to become supercritical. It is thought that the native solute clusters are amorphous aggregates, which are dense and liquid-like in structure.[5,7,8]

Evidence of such species has come from the study of protein nucleation;[10,30] however *in silico* studies suggest that the 2-step mechanism of crystallization could be more generally applied to most systems.[8,32,103-105]

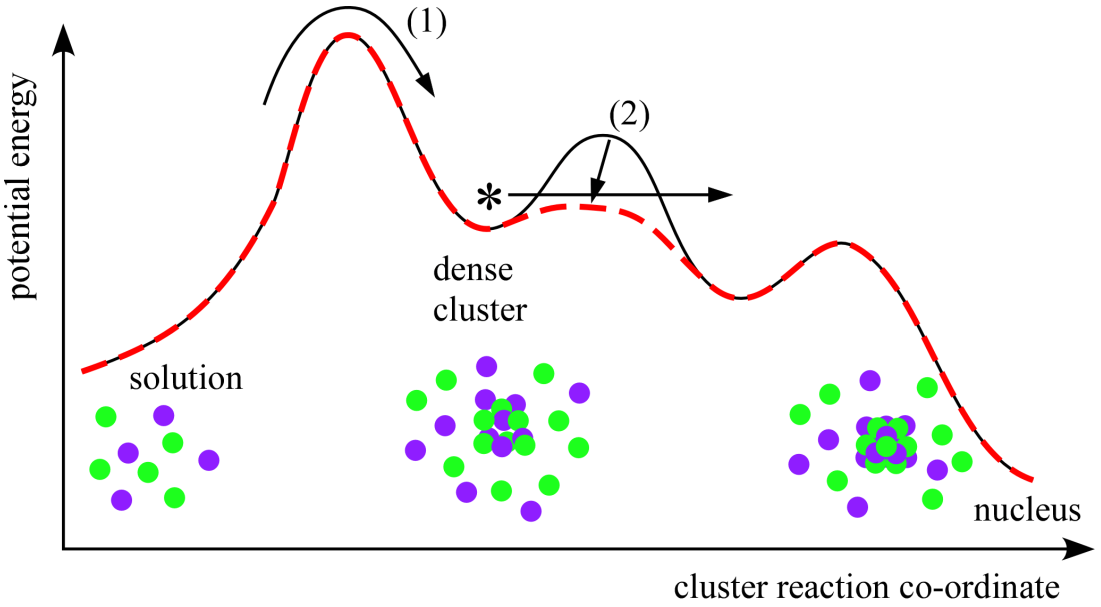

Figure 2.3 Schematic showing the transition (1) of a solute cluster from being loosely associated in solution to forming a dense cluster (*), and its internal rearrangement to form a crystalline nucleus due to the electric field (E) of the laser pulse (2). The curves represent the potential energy of a candidate cluster in zero-field ($E = 0$, black solid line) and high-field ($E > 0$, red dashed line). The dense cluster (*) is assumed to be non-crystalline or glass-like in structure and may contain solvent molecules. Green circles represent chloride anions, and purple circles represent sodium cations; water molecules have been omitted for clarity.

In the aqueous potassium halide systems, molecular dynamics calculations suggest that the clusters would be highly disordered and contain one or more solvent molecules within the cluster, or associated to its surface $\left[K_x^+X_y^-\right]^{x-y}(H_2O)_z$.[106] With reference to Figure 2.3, the disordered solute cluster can be pictured on a multidimensional potential surface, where the number of degrees of freedom (such as bond lengths and angles) is ~ $3N$ (where N is the total number of ions and solvent molecules). In zero-field, the cluster is essentially trapped at a local minimum on the potential energy surface. With a suitable electric field present, the potential energy associated with a particular exit channel from the local minima would be lowered, allowing the cluster to become supercritical and nucleate. The sketch shown in

Figure 2.3 shows a simplified version of what is expected. In reality, there may be multiple energy barriers in different directions from the local minima, however only one reaction coordinate that is more susceptible to the electric field is required for nucleation to proceed. After exiting the initial local minima, the cluster may possess sufficient kinetic energy to allow it to pass further local minima and potential energy barriers.

In the mechanism of nucleation in NPLIN discussed here, the role of the electric field is to drive the reorganization step where the cluster 'clicks' into crystalline form. In the densely packed pre-nucleated cluster, only relatively small changes in ion coordinates would be required to achieve criticality. During the typical duration of laser pulse used in these experiments (~5 ns) many periods of motion of the constituent ion pairs can occur.[107] The estimated period of ion pair motion is estimated to be ~1 ps, the motion of larger aggregates can be expected to 1 or 2 order of magnitude greater, ~100 ps.

The idea of a rapid transformation from disordered cluster to crystalline nucleus has been proposed before. During their investigation of crystalloluminescence (emission of light due to crystallization) of NaCl, Garten and Head observed point flashes of light that correlated quantitatively with the number of nuclei formed.[108,109] After considering the photon energies, and solution concentrations involved, they concluded "...that the primary excitation energy is derived from a phase change, indicating that critical nucleus which forms by diffusion as a disordered quasi-liquid or glass-like aggregate eventually 'clicks' into crystalline form in less than 8×10^{-8} sec.". The quoted time scale was limited by the photodetector used; later investigation saw the value revised to < 5 ns.

In the current analysis, the model used is based on classical nucleation theory. Although the model has been shown to do an excellent job of replicating the experimental data, there is scope to refine the model further. Perhaps the most obvious starting point for this would be to base the isotropic electronic polarization scheme solely within a 2-step nucleation mechanism. In order to pursue this direction, more work must be carried out to elucidate the structure of a supersaturated solution, that is, knowledge of the dense-cluster phase and the associated cluster populations and distributions in the system. Therefore, further

experimental and theoretical work is needed to elucidate these key, and currently unknown, factors.

2.5 Conclusions

In conclusion, the effects of temperature and wavelength have been investigated in the NPLIN of KCl and KBr from supersaturated aqueous solution. It was observed that samples exposed to 532 nm pulses were nucleated more efficiently than those exposed to 1064 nm pulses. Further experiments were carried out in which KCl samples of equal supersaturation (S = 1.060) at two different temperatures (23 and 33 °C) were shot with single pulses of 1064 nm light. The results suggest that both sample sets share a common threshold power density, with the samples prepared for 33 °C showing significantly higher sample lability than those at 23 °C.

NPLIN results were analysed using a model based on the polarization of subcritical clusters in solution, which provides a remarkably good description of the probability of nucleation occurring as a function of incident peak power density and solute used. It is hoped that the work discussed here will stimulate further experimental and theoretical work that is required in order to achieve a better understanding of the underlying processes and dynamics that take place in NPLIN and crystal nucleation in general.

Chapter 3: Non-photochemical nucleation of potassium chloride induced by an evanescent wave

3.1 Introduction

The discovery of NPLIN has, undoubtedly, provided experimenters with an unprecedented control over the nucleation process;[54] however, the technique still probes a relatively large volume of solution (~1 cm^3). In order to study the finer details of the nucleation mechanism, it would be highly advantageous to localize the nucleation event within a volume more commensurate with the magnitude of the expected dynamics. There have been reports in which nucleation has been induced by use of a focussed beam, with the nucleation event observed around the region of the focal volume.[110,111] In such studies, due to the focussing, the peak power densities achieved are extremely high and reach values at which photochemical nucleation schemes operate. In addition such high laser intensities can cause physical shock and damage to the sample vessel that may lead to nucleation: this is termed photomechanical damage. With the aim of improving the spatial control of nucleation, the use of NPLIN by an evanescent wave has been investigated.

An evanescent wave occurs at the point of total internal reflection (TIR)[112] where an electromagnetic wave in a dielectric medium with index of refraction n_2 is reflected at an interface of lower optical density, n_1, and the angle of incidence θ_i is greater than the critical angle θ_c, given by Equation 3.1.[113]

$$\theta_c = \sin^{-1}\left(\frac{n_2}{n_1}\right) \tag{3.1}$$

For any angle of incidence less than θ_c, a portion of the incident light will be transmitted and the rest reflected. Figure 3.1 shows the process of TIR and the evanescent wave generated.

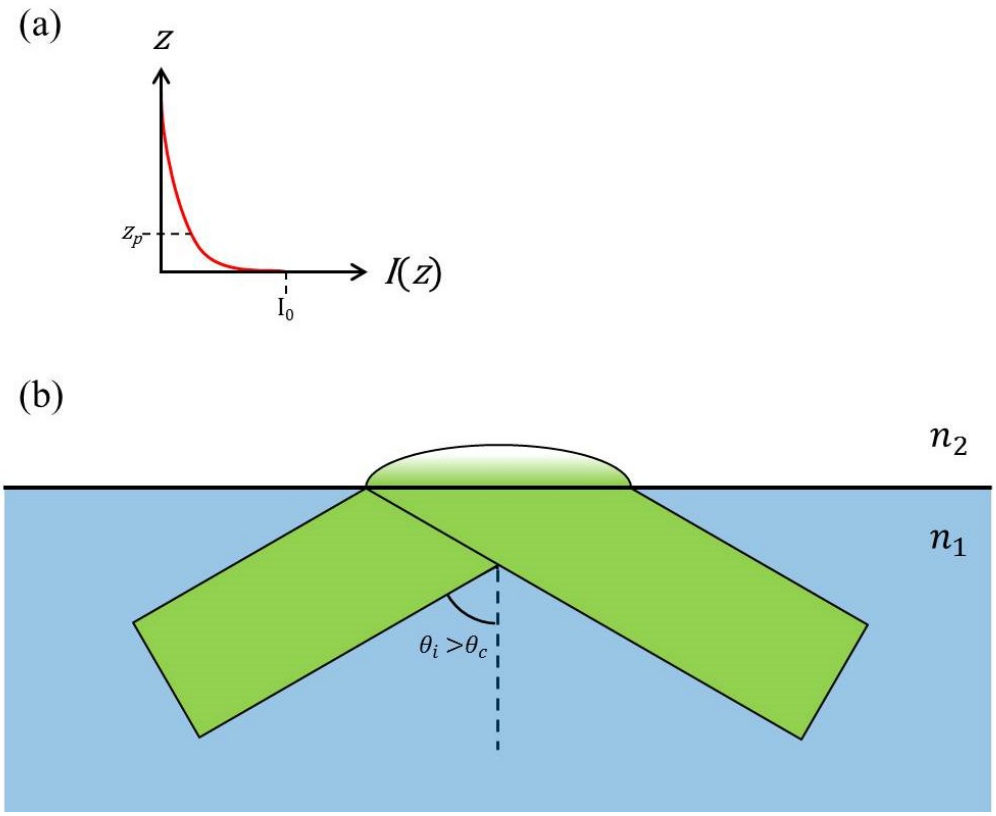

Figure 3.1 Diagram showing (a) the intensity profile of the evanescent wave which decays exponentially with distance from the interface ; and (b) the process of total internal reflection and the resulting evanescent wave that penetrates in to the medium with lower refractive index ($n_1 > n_2$). The value z_p represents the penetration depth (Equation 3.3) which is typically a fraction of the incident wavelength. For the experimental setup used in this work a value z_p = 86 nm is calculated. The intensity profile above the interface can be calculated by $I(z) = I(0) \exp\left(-\frac{z}{z_p}\right)$.

Typically, an evanescent wave penetrates the medium of lower refractive index by a small amount, a distance of the order of magnitude of the wavelength of light used.[112] Due to the short penetration distance, it is thought that the evanescent wave may be a means to observe NPLIN within a highly localized region. In this Chapter evanescent wave NPLIN (ew-NPLIN) is demonstrated in droplets of supersaturated potassium chloride at the glass interface of a dove prism.

3.2 Experimental

An evanescent wave was produced using a Dove prism as shown schematically in Figure 3.2. It is noted that the angle of internal reflection ($\theta = 72.7°$) differs significantly from the critical angle ($\theta_c = 63.9°$); this is a consequence of the convenient experimental geometry used as the horizontal laser beam was incident at an angle of 45° to the face of the prism.

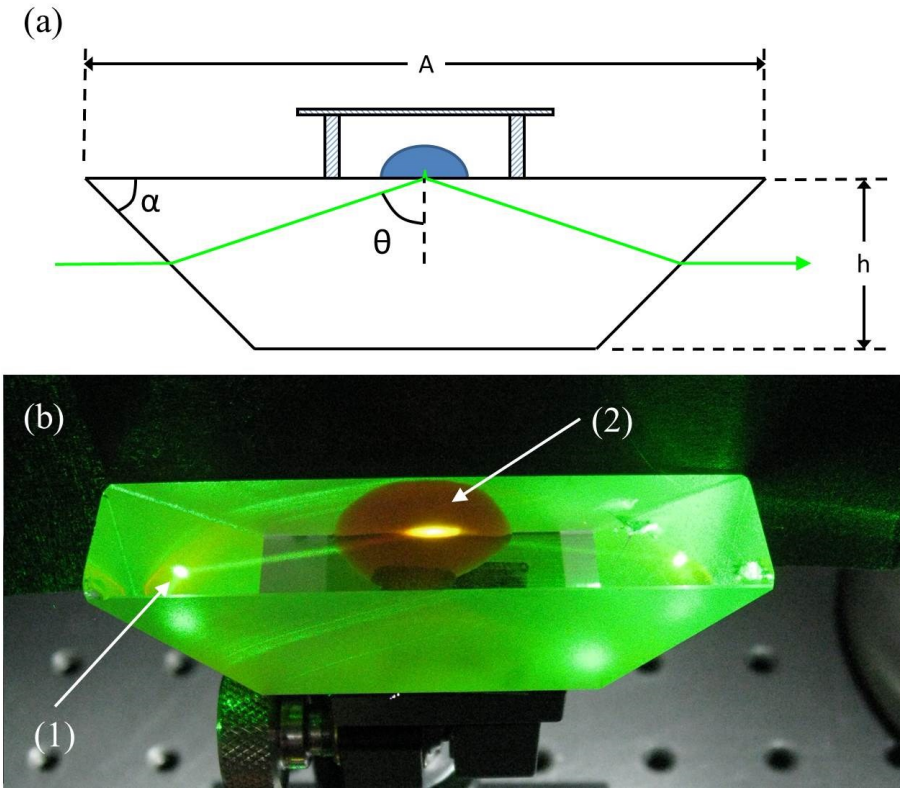

Figure 3.2 (a) Schematic diagram of the dove prism with dimensions A = 68 mm, h = 16 mm and α = 45°. The prism was made from BK7 glass with refractive index $n_1 = 1.519$ at 532 nm. The angle of internal reflection was calculated to be θ = 72.7°; the corresponding critical angle (assuming a droplet of supersaturated KCl with $n_2 = 1.365$) was $\theta_c = 63.9°$. (b) Photograph showing the beam path within the prism: the beam travels from left to right entering the prism at (1). The projection of the spatial profile of the Gaussian beam at the reflection interface is elliptical, as illustrated by the fluorescence observed in an aqueous droplet of rhodamine 610 dye at (2).

The surface of the prism went through a stringent cleaning procedure prior to sample assembly. The surface was cleaned thoroughly with ethanol before rinsing with 0.22 μm (Millex GP) filtered ultrapure water and dried in a 70 °C oven. Following the rinsing stage, in order to prevent contamination of the cleaned surface, the prism was

housed under a glass enclosure whenever possible. The saturation concentration of KCl at 23 °C was C_{sat} = 4.688 mol kg^{-1}.[94] A sample solution with supersaturation (C/C_{sat}) of S = 1.080 was prepared using potassium chloride (puriss, >99%, Fluka) without any further purification and ultrapure water. In order to eliminate solvent loss from the sample and any atmospheric contamination, the sample droplet was enclosed within a coverslip-capped glass ring assembly. Immediately prior to assembling the cell the prism surface was cleaned using a drag-wiping technique with ethanol and optical tissue to ensure a clean surface. The glass ring and coverslip were bonded centrally to each other, and the prism, using ultraviolet-curing adhesive (Norland Optical Adhesive 63) as shown in Figure 3.2.

Prior to shooting with the laser, the prism and enclosed droplet were placed in an oven at 50 °C for a period of one hour to redissolve any crystals that may have formed and allowed to cool for one hour to ambient temperature (23 °C). Samples were shot using the frequency doubled output (532 nm) from a Nd^{3+}: YAG (Continuum, Surelite II-10) pulsed laser system. The laser beam was passed through an iris of 8 mm diameter and then directed through a Glan-laser polarizer before entering a simple optical telescope (+200 mm planoconvex lens and -63 mm planoconcave lens) which produced a 2.5 mm diameter beam. The laser power was controlled by rotating the Glan-laser polarizer relative to the angle of the native linear polarization of the laser source.

The mean laser power of the 8 mm diameter beam was measured using a power meter (Nova, Ophir). Starting with a mean laser power of 10 mW (0.5 MW cm^{-2}), the sample was shot with 10 pulses, and then monitored for nucleation over a 3 minute period. If no nucleation had occurred, the mean laser power was increased by 10 mW and then shot again with 10 pulses. This process was repeated until nucleation had occurred, the laser power at which nucleation had occurred was recorded and the sample was refreshed, following the regeneration procedure outlined above. Samples were refreshed a maximum of 3 times before a new droplet was produced for experiments. In total, 16 samples were used which were found to nucleate with mean laser powers in the range 120–370 mW. In addition, the position of the resultant crystals following nucleation was noted.

3.3 Results

In these experiments, the sample droplet is not directly exposed to the incident laser pulse; nucleation is induced by the evanescent wave that results from total internal reflection within the dove prism. In order to calculate the maximum peak power density at the prism surface, elongation of the circular beam, due to refraction and reflections, must be accounted for. Simple ray-tracing methods show that an elliptical profile with beam area of 0.21 cm^2 is produced at the point of total internal reflection. After correcting for intensity losses due to the angle of polarization incident on the dove prism the peak power densities were calculated for each laser power used in experiment. Peak power densities in the range 9.9–31.6 MW cm^{-2} were achieved during experiments.

The intensity of the evanescent wave decays exponentially above the prism surface in the perpendicular direction (z) according to Equation 3.2.[112]

$$I(z) = I(0)\exp\left(-\frac{z}{z_p}\right). \tag{3.2}$$

The penetration depth, z_p, is characteristic of the system geometry and the wavelength, λ, and is given by Equation 3.3.[112]

$$z_p = \frac{\lambda}{4\pi\sqrt{(n_1^2 \sin^2\theta - n_2^2)}}, \tag{3.3}$$

where n_1 and n_2 are the refractive indices of the prism and the solution droplet at the point of TIR. For the experiments reported here, a penetration depth of z_p = 83 nm in to the solution droplet is calculated.

A plot of the cumulative fraction of samples nucleated is shown in Figure 3.3. The cumulative fraction is found by summing the total number of samples that nucleated at or below a certain laser power.

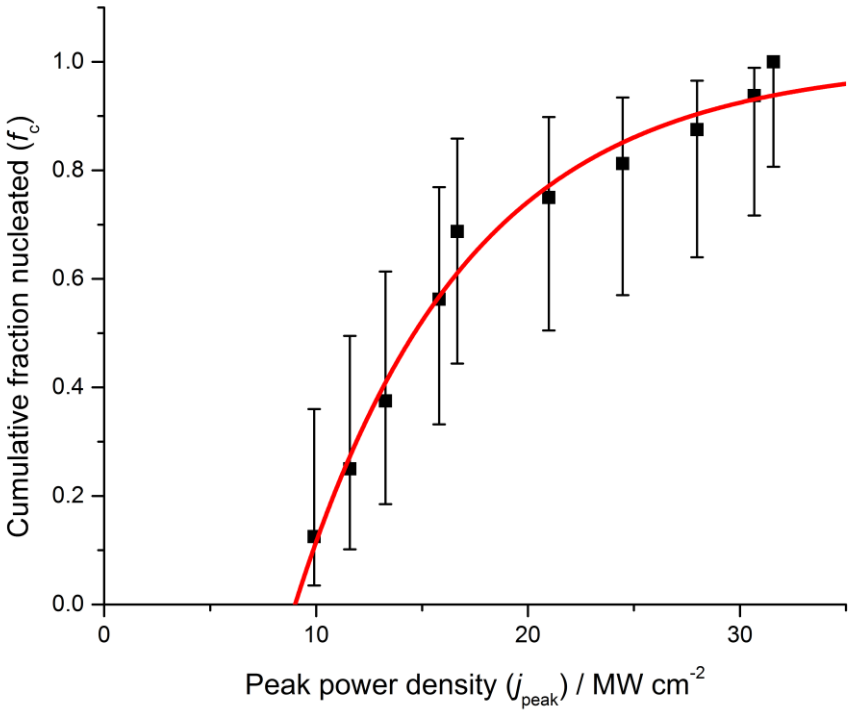

Figure 3.3 Plot of cumulative fraction of samples nucleated (f_c) against peak power density of the laser pulses (j_{peak}). Solid squares represent the experimental points; uncertainties were calculated at 95% confidence using the Wilson-score method.[85] The solid line represents a fit to a Poisson model of the nucleation probability. The model fit returns a threshold peak power density $j_0 = 9.0 \pm 0.3$ MW cm^{-2}, and a lability (slope at threshold) $m = 0.123 \pm 0.009$ cm^2 MW^{-1} (uncertainties represent standard errors from the nonlinear least-squares fit).

The data has been fitted with a Poisson model based on the IP model of NPLIN introduced in Section 2.4, giving parameter values of $m = 0.123 \pm 0.008$ cm^2 MW^{-1} and $j_0 = 9.01 \pm 0.35$ MW cm^{-2}. These values differ from the experimental values obtained from bulk samples placed directly in the beam path (Section 2.2), for ease of comparison these values are compared in Table 3.1.

		Fitted parameter values	
	Supersaturation (S)	lability (m) / cm^2 MW^{-1}	Threshold (j_0) / MW cm^{-2}
Evanescent wave	1.08	0.123 ± 0.008	9.0 ± 0.4
Vials	1.06	0.057 ± 0.004	5.6 ± 0.5

Table 3.1 Values of samples lability (m) and threshold peak power density (j_0) for experiments using an evanescent wave (ew-NPLIN, present work) compared to previous experiments where the beam was passed directly through solutions contained in glass vials (results of KCl nucleation reported in Sections 2.3). Note that the supersaturation used in the ew-NPLIN was higher. The resulting threshold and labilities were observed to be higher for ew-NPLIN.

Comparison shows that sample lability, m, obtained during the evanescent wave experiments is a factor of 2.16 greater than that obtained during bulk samples. The supersaturation dependence of NPLIN of KCl has previously been investigated by Alexander & Camp where samples in the range S = 1.053–1.102 were nucleated using a 1064 nm pulse. Their experimental data show a ratio of sample lability for samples of S = 1.08 and 1.06 of 1.5; indicating that the increased lability observed here for ew-NPLIN is due to more than an effect of solute concentration. Similarly, it can be seen that a higher threshold power density, j_0, is found during the evanescent wave experiments.

During the course of experiments the location of the produced crystal was noted, and was found to always be situated at a point along the elliptical profile of the reflected beam: see Figure 3.4. In some cases, the crystal formed was seen at the surface of the sample droplet. It is thought that convections within the droplet, driven by the crystal growth process, transport the growing nucleus to the surface where it becomes trapped at the air–solution interface and continues to grow.

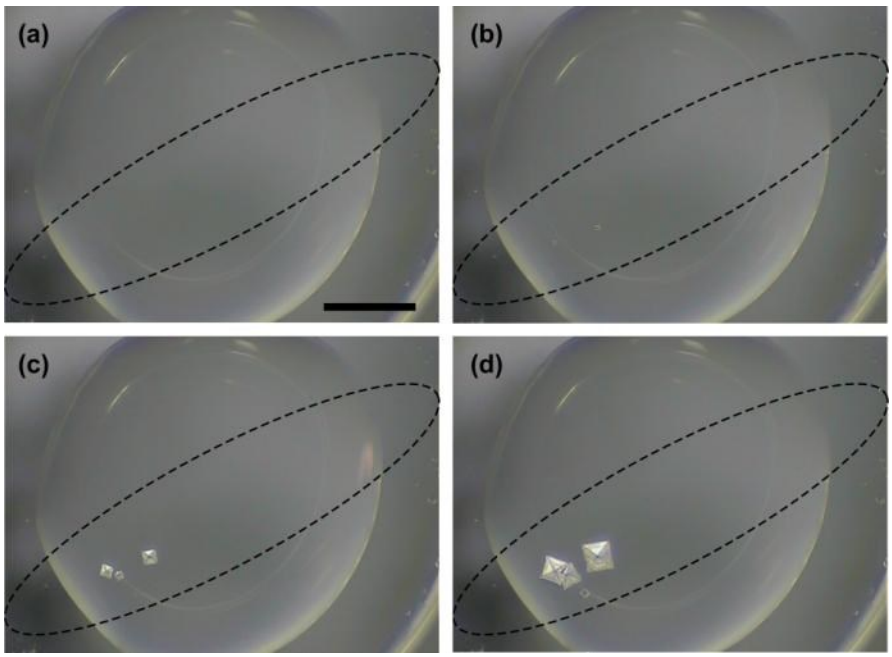

Figure 3.4 Examples time-lapse still images taken from a video recording of an ew-NPLIN experiment using a droplet of supersaturated (S = 1.08) KCl. Images are taken at (a) 10 s, (b) 30 s, (c) 60 s and (d) 300 s after nucleation. The dashed ellipse represents the approximate outline of the evanescent region. The scale bar in (a) represents 2 mm.

3.4 Discussion

The findings of this study are somewhat unexpected. Comparing the values of threshold power density and lability to those of bulk NPLIN studies (Table 3.1) it is found that a higher threshold and lability is obtained for ew-NPLIN, i.e., the samples are more labile to nucleation, but a higher threshold laser power is required to cause nucleation. The previous studies were carried out in vials; therefore, the results presented here suggest that the presence of the prism surface has an influence on nucleation. Possible causes might include (i) sedimentation of larger particles by gravity, so that they are more likely to fall within the evanescent field; (ii) effects due to the surface itself: either chemical or physical.

3.4.1 Sedimentation

According to classical nucleation theory,[2,5] solute clusters which are larger in size will be more likely to nucleate. We will assume that clusters or nanoparticles are spherical, at infinite dilution in the supersaturated KCl solution, which we

consider as an ideal solvent. The diffusion coefficient of a spherical particle can be obtained from the Stokes–Einstein equation:[114]

$$D = \frac{k_B T}{6\pi\eta r} \tag{3.4}$$

where k_B is the Boltzmann constant, T is temperature, η is viscosity of the solvent, and r is the radius of the particle. The root-mean-square displacement of the particle due to Brownian motion is given by $s_B = (6Dt)^{\frac{1}{2}}$,[114] where t is time. The limiting velocity of sedimentation (v_s) of a sphere is calculated by considering the hydrodynamic frictional force balanced against the external forces due to gravity:[115]

$$v_s = \frac{2gr^2\Delta\rho}{9\eta}, \tag{3.5}$$

where g is the gravitational acceleration (9.81 m s^{-2}) and $\Delta\rho = \rho_p - \rho_s$ is the difference in densities between the particle (ρ_p) and solvent (ρ_s); using the densities for crystalline KCl and supersaturated aqueous solution (Table 2.2), we have $\Delta\rho$ = 808 kg m^{-3}. The displacement over time t due to sedimentation (s_s) is then given by $s_s = v_s t$. Comparing the displacement due to Brownian motion (s_B) against gravitational sedimentation (s_s) over t = 1 s it is found that the values become comparable for particles with radius r ~ 840 nm. This is significantly larger than the nominal pore radius (110 nm) of the filters used in experiments. Therefore it is expected that sedimentation is insignificant for the size of particles involved in ew-NPLIN. It is possible, though, that pre-nucleated clusters grow after the filtration process. Recent work has shown that liquid-like clusters in concentrated glycine and DL-alanine solutions can deform to pass through a filter with pore size smaller than the cluster diameter.[23,24] In the absence of evidence supporting the idea of deformable clusters in concentrated KCl solution, sedimentation is ruled out as the source of the increased sample lability in ew-NPLIN of KCl.

3.4.2 Physical and surface effects

Due to the short penetration depth (z_p = 86 nm) of the evanescent wave, the particles nucleated by the laser pulse must be initially in very close proximity to the surface. Volmer's model of heterogeneous nucleation considers the free energy

change ΔG_{het} for growth of a hemispherical cluster on a flat surface: the free energy change for homogeneous nucleation ΔG_{hom} is modified by a factor[2,91]

$$\Delta G_{\text{het}} = f(\theta)\Delta G_{\text{hom}}\,, \tag{3.6}$$

where ΔG_{hom} is the free energy change for homogeneous nucleation and

$$f(\theta) = \frac{1}{2}(2 + \cos\theta)(1 - \cos\theta)^2\,. \tag{3.7}$$

Here θ is the contact angle between the substrate and the surface. The factor $f(\theta)$ takes values between 0 and 1, representing the affinity between the cluster and surface. The contact therefore lowers the free-energy barrier to cluster formation, and hence for nucleation. As discussed in Section 1.5.2 for NPLIN of molten sodium chlorate, it has been shown that the role of a heterogeneous surface was vital to the resultant nucleation.[89] For ew-NPLIN it seems very likely that interactions between a pre-nucleated cluster and the prism surface would reduce the free-energy barrier to nucleation, thus increasing the lability in comparison to bulk experiments.

An alternative explanation for the observed increase in lability may come from polarizability. As described by the IP model of nucleation of NPLIN,[55] the free-energy landscape of a pre-nucleated cluster is modified by the interaction between the electronic polarizability of the cluster and the electric-field of the laser pulse. The magnitude of this contribution to the cluster free-energy is given by $\Delta G_E = -aE^2$, where E is the electric-field, and parameter a depends on the dielectric permittivities of the cluster and surrounding solvent. Since part of the cluster is in contact with the surface rather than the solvent, this term will be modified. The magnitude of the modified term will depend on the permittivity of the substrate, and the degree of interaction between the cluster and the surface. Comparing the results in Table 3.1 it is seen that the sample lability for ew-NPLIN is a factor of 2.16 greater than the regular NPLIN outcome; therefore a similar increase in the value of ΔG_E would be expected to account fully for the increased sample lability. With permittivity values of a KCl particle (ε_p) and supersaturated solution (ε_s) calculated using the Maxwell relation ($\varepsilon = n^2$) the value of a can be evaluated using the following expression,

$$a = \frac{3\varepsilon_0\varepsilon_s}{2}\left(\frac{\varepsilon_p - \varepsilon_s}{\varepsilon_p + 2\varepsilon_s}\right) \tag{3.8}$$

where ε_0 is the vacuum dielectric permittivity. For NPLIN nucleation of KCl performed in vials a value of $a = 1.825 \times 10^{-12}$ F m^{-1} is calculated. To account fully for the increased lability measured for ew-NPLIN then a value of $a = 3.938 \times 10^{-12}$ F m^{-1} would be expected; the effective particle permittivity (ε_p^*) can then be estimated by rearrangement of Equation 3.9;

$$\varepsilon_p^* = -\frac{(3\varepsilon_0 {\varepsilon_s}^2 + 4a\varepsilon_s)}{(2a - 3\varepsilon_0\varepsilon_s)}. \tag{3.9}$$

Using the values listed in the text the effective permittivity of a particle interacting with the prism surface would be $\varepsilon_p^* = 2.921$; an increase of ~1.3 over the value estimated for a crystalline particle of KCl. This estimate is based solely on the factor of 2.16 increase in sample lability observed for ew-NPLIN ($S = 1.08$) compared to NPLIN in vials ($S = 1.06$). The effect on concentration on this value was discussed in Section 3.3 where a factor of 1.5 increase in lability was attributed to solute concentration. Taking in to account the effect of concentration on sample lability a value of $\varepsilon_{\mathrm{P}}^* = 2.541$ ($n_{\mathrm{p}}^* = 1.594$) is estimated; a factor of 1.10 greater than that of a crystalline particle of KCl. It is noted that the value of n_{p}^* (calculated using Maxwells relation, $\varepsilon = n^2$) estimated here is more similar to the value for the prism ($n = 1.519$) than for KCl ($n = 1.493$). To investigate the role of the prism surface in ew-NPLIN requires further work; however the notion that interaction with the prism surface could enhance nucleation through favourable interaction appears plausible. Furthermore it is possible that the two surface effects discussed here could operate cooperatively to provide the observed increased sample lability.

3.4.3 Effect of volume probed

In addition to the higher lability, an increased threshold for nucleation was observed for ew-NPLIN (see Table 3.1). At present there is no clear explanation for the increased threshold. Another key difference between ew-NPLIN and NPLIN in vials is the volume of solution probed by the electric-field. The footprint of the evanescent field used in the present work was estimated to be 0.21 cm^2. Using the calculated penetration depth ($z_{\mathrm{p}} = 86$ nm) the volume of probed solution is estimated to be ~2×10^{-6} cm^3; five orders of magnitude less than that probed during NPLIN experiments in vials (~0.2 cm^3). With reference to Equation 3.3 it is seen that the

penetration depth z_p is dependent on the angle of internal reflection. A future investigation of nucleation probability as a function of penetration depth (i.e., volume probed) is recommended for future work. Such an experiment would be a convenient way of assessing the effect of probed volume in the ew-NPLIN of KCl, and potentially other systems too.

Although the surface effects inherent to ew-NPLIN act to enhance the probability of nucleation occurring, the significantly reduced volume of solution that is probed will have an effect to the contrary. In this context it is proposed that the higher threshold and higher sample lability are a result of the two opposing consequences of ew-NPLIN; (i) favourable surface effects which act to enhance NPLIN, and (ii) unfavourable volume effects that lower the probability of the electric field to encounter a pre-nucleated cluster of sufficient size and structure.

With reference to Equation 3.3 it is seen that the penetration depth z_p is dependent on the angle of internal reflection. An investigation of nucleation probability as a function of penetration depth (i.e., volume probed) is recommended for future work. Such an experiment would be a convenient way of assessing the effect of probed volume in the ew-NPLIN of KCl, and potentially other systems too.

3.5 Conclusions

In conclusion, the results presented here successfully demonstrate ew-NPLIN of KCl from aqueous supersaturated (S = 1.08) solution. The power dependence of nucleation probability was investigated, giving a threshold power density of j_0 = 9.0 ± 0.4 MW cm^{-2} and a sample lability of m = 0.123 ± 0.008 cm^2 MW^{-1}. Both of these values exceed those determined for NPLIN of KCl from solution (S = 1.06) in sample vials. The differences in the results cannot be explained by the concentration difference alone, and clearly implicate the dove prism surface as a source of the dissimilar behaviour. A combination of effects is proposed to account for the experimental observations. The role of the surface in the increased lability is expected to result from two possible contributions: (i) the surface providing a heterogeneous substrate for a pre-nucleated cluster which acts to lower the free-energy barrier to nucleation, and (ii) the surface providing a favourable interaction

with pre-nucleated a cluster to enhance the electrostatic contribution to the free-energy barrier to nucleation through polarization effects. Due to the intensity profile associated with an evanescent wave, the volume of solution probed by the electric field (~2×10^{-6} cm^3) is five orders of magnitude less than that in previous reports (~0.2 cm^3). The reduced probability of the electric-field being incident upon a pre-nucleated cluster of critical dimensions was proposed to account for the increased threshold to nucleation.

Chapter 4: Rayleigh scattering in concentrated salt solutions: An investigation of solution structure

4.1 Introduction

Classically, solutions of low molar mass compounds and mixtures of freely miscible liquids have been considered as homogeneous on length-scales exceeding the molecular scale.[5,116] This view is in contrast with the basis of both CNT[2] and the 2SM[5,8,9] of nucleation; both of which assume the formation of molecular clusters prior to the nucleation event. Initial experimental evidence in support of solute clustering was indirect being provided by measurements such as diffusivity[47,117,118] and Raman spectroscopy.[119] Recent development of laser scattering techniques[46,49-51] has since provided an ever-increasing body of direct evidence that a wide range of chemical systems contain populations of mesoscopic particles; also assumed to be solute clusters (see Section 1.3.5). The scattering particles have been characterised for many systems where it has been established that they are real, long-lived particles with dimensions on the nanometre-scale (~10^1–10^2 nm diameter).[23,24,46,116] Particles of this size are typically smaller than the wavelength of light used in experiments, therefore the observed scattering is classed as Rayleigh scattering.

There remains debate on the exact nature of the particles identified in laser scattering experiments, i.e. are the objects native solute clusters, or are they simply due to impurities or contaminants? Studies in which the dynamics of the scattering objects have been examined suggest that the particles are not impurities.[23,24,46] A comprehensive investigation of cluster formation in α-amino acids identified populations of particles whose size was reduced by filtering (Anotop 25 anodic alumina filters, 20 nm pore size), however were then seen to reform rapidly (within 10s of seconds).[46] Similarly, in concentrated aqueous glycine solutions, the population of scattering particles can be removed from solution by filtration (Anotop 25, 20 nm pores) and then regenerated by dissolution of a seed crystal.

The chemical composition of these scattering particles has yet to be identified because of the challenging nature of such an experiment. Not only have laser scattering experiments shown an abundant population of nano-scale particles in

solution, but they must be studied *in-situ*. It is hoped that increasing the catalogue of systems investigated by laser scattering will (i) provide an insight to the fundamental nature of the observed particles, and (ii) help to identify solution systems for further characterization experiments. In this Chapter, a range of chemical systems were tested using a simple laser Rayleigh scattering technique to identify whether or not they contain populations of particles. The video footage collected during sample screening was then analysed using a bespoke nanoparticle tracking software to obtain an estimate of the size distribution of identified particles. In the remainder of this chapter, the findings are discussed with reference to the most likely sources of the particles.

4.2 Experimental

A simple sample cell was constructed using a quartz 4-windowed fluorescence flow cell (Starna, 2 mm pathlength, 0.9 mL nominal volume): see Figure 4.1. The cell ends were closed using silicone tubing and polycarbonate taps with luer-fittings to allow easy and clean rinsing of the cell and filling. Prior to use the sample cell, tubing and taps were soaked overnight in a specialist cuvette cleaning solution (Hellma, Hellmanex III), then rinsed thoroughly with deionized water. To ensure the cell was thoroughly rinsed, 40 cm^3 of filtered (0.22 μm) deionized water was flowed through the cell in both directions while simultaneously turning the taps. After rinsing, with the cell full of water, the cell was placed in the optical setup and inspected. If the cell showed no visible particles passing through the laser beam at the highest laser power, then the cell was considered clean and ready for sample solution. If particles were visible, then the rinsing procedure was repeated until the sample was free of visible particles.

A range of sample solutions were inspected. The solute systems chosen for investigation were those that have previously been demonstrated to undergo NPLIN or those whose effect on bubble stabilization has been determined; a possible cause of the scattering objects identified in laser scattering experiments. Sample concentrations equivalent to a supersaturation of $S = 0.95$ at the experimental temperature ($T = 23$ °C) were used. A full list of the solutes and the sample solution concentrations is shown in Table 4.1. Sample solutions were dissolved by gentle

heating in a temperature-controlled water bath held at 40 °C. Whilst warm, approximately 5 cm^3 of sample solution was flowed through a syringe filter (0.22 μm, Millex-GP) to flush, after which approximately 15 cm^3 of sample was flowed through the cell and the taps closed before removing the filter and syringe. To prevent unwanted crystallization at the tap ends, the exposed ports were rinsed to remove any residual sample solution using filtered ultrapure water. The cell was then mounted in the optical setup to ensure correct alignment and then left in place for 30 minutes to allow the solution to cool to the appropriate temperature. As well as sample solutions, a series of samples that contained particles of known sizes were inspected. Aqueous dispersions of polystyrene spheres with diameters of 1.0, 0.53, 0.18 and 0.1 μm were prepared by addition of ultrapure water to achieve sample concentrations of approximately 0.002 mg mL^{-1}. To rule-out cross contamination, a separate cell assembly, with identical dimensions, was used exclusively for samples of polystyrene spheres.

A perpendicular scattering and observation arrangement was used during experiments. Scattering light was provided by a continuous-wave (CW) laser source (MGL-III-532, λ = 532 nm) with the 2 mm diameter beam focussed using a +63 mm plano-convex lens. The sample cell was located such that the focussed beam waist was in the centre of the sample cell. Fine control over the cell position was provide by a micrometer *x*, *y* translation stage. The scattered light was detected using a CCD camera (AVT, Stingray F033B) and a microscope objective (Achrovid, ×10 magnification, 0.21 NA), the camera and objective assembly was mounted on a micrometer *xyz* translation stage to allow fine control over its position relative to the sample cell.

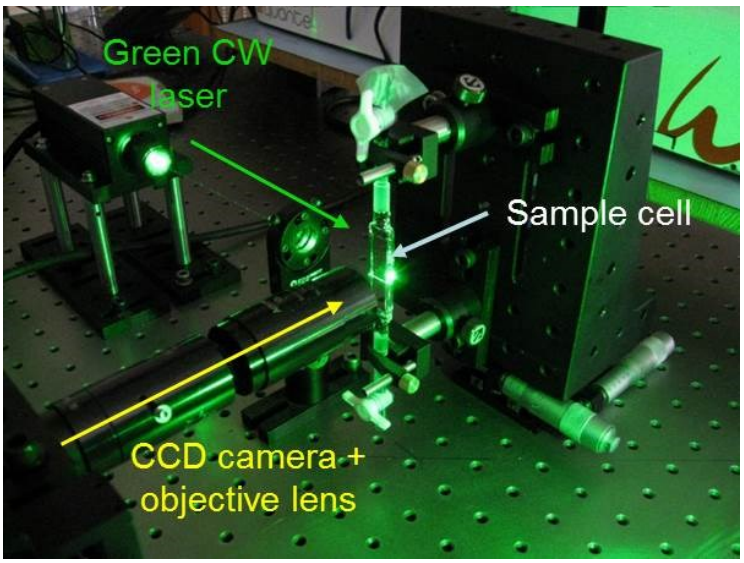

Figure 4.1 Picture showing the experimental setup used to perform laser scattering observations. The continuous wave (CW) scattering laser (532 nm) is focussed in to the centre of a 4-windowed flow-cell using a 63 mm plano-convex lens. Scattering is recorded using a microscope objective and CCD camera arranged perpendicular to the incident scattering CW beam.

4.3 Results and Discussion

4.3.1 Sample screening

With a view to investigating the nature of the particles observed in laser scattering experiments, numerous near saturated ($S = 0.95$) aqueous solute systems were tested using a simple laser scattering experiment as shown in Figure 4.1. The majority of experiments were carried out using a low level of magnification (×10, 0.21 NA), however some samples were inspected using higher magnification objectives (×50 and ×100) with a similar scattering setup at the Lasers for Science Facility at Harwell, Oxford. Samples tested with higher magnification will be identified in the text. A complete list of the systems tested is given in Table 4.1. During the course of testing different samples it was found that some samples showed scattering objects passing through the laser beam and some showed none at all. At a given level of magnification it was found that the type and abundance of scattering particles, or the lack thereof, in a particular solution was consistent over several repeat experiments.

Solution	See particles?	Ion combination	mol% solute
Water	no	αβ	N/A
Tetrabutylammonium perchlorate (TBAP)	yes	ββ†	0.001
Tetramethylammonium perchlorate (TMAP)	yes	ββ	0.12
Potassium dihydrogen phosphate	yes		2.92
Ammonium perchlorate	yes	αβ	3.33
Glycine	yes		5.12
Sucrose	yes	αα*	5.20
Potassium chloride	yes	αα	7.41
Ammonium chloride	yes	αα	11.0
Sodium chlorate	no	αβ	13.7
Tetraethylammonium chloride (TEAC)	yes	βα†	15.4
Sodium perchlorate	no	αβ	22.2
Urea	yes	αα*	24.5
Ammonium nitrate	no	αα	30.3
Potassium acetate	yes	αβ	31. 5
Acetamide	no		54.1

Table 4.1 Summary of the sample solutions tested using laser Rayleigh scattering (Figure 4.1). All sample solutions were prepared to have a saturation of $S = 0.95$. The observations were made using a ×10 objective (0.21 NA). The incident laser power required to observe particles varied for each sample. Samples identified as not containing particles showed no scattering particles at the highest available laser power but did show a strong background haze (Figure 4.2). The notation for ion combination (α/β) will be discussed later in Section 4.3.7.

Consideration of the results summarized in Table 4.1 shows no obvious trends as to why a certain sample solution shows scattering particles in solution and another does not. However, for samples that show no particles moving through solution, the unresolved background scatter (or 'haze') due to the laser passing through solution often appears more intense than in other solutions. This behaviour typically coincides with samples of high absolute concentration (approximately > 11 mol% solute). Figure 4.2 shows a side by side comparison of the scattering typically observed from filtered solutions of KCl and ammonium nitrate.

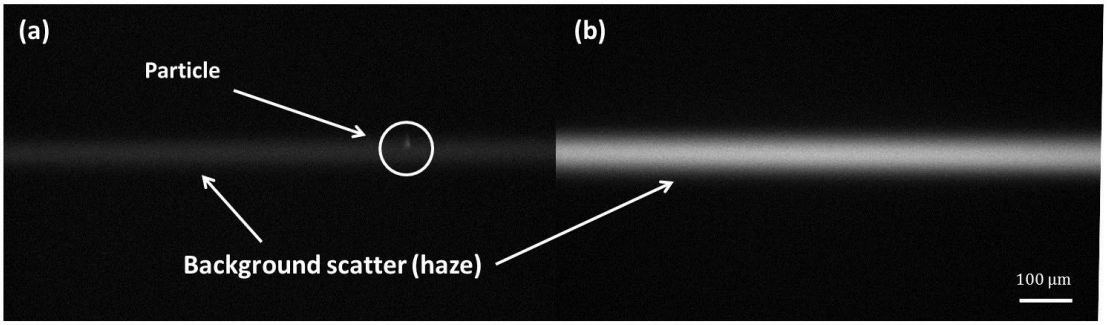

Figure 4.2 Comparison of the typical scattering observed in sample solutions of low and high solute concentration (×10 magnification). The stills have been taken from video footage recorded during testing of 95% saturated aqueous solutions of; (a) potassium chloride (7.41 mol%) and (b) ammonium nitrate (30.3 mol%). A higher laser scattering power (67 mW) was used for sample (a), however it is clear that the background haze is more intense in sample (b) where a far lower power was used (35 mW). The scale bar (bottom right) represents 100 µm.

Ammonium nitrate is a highly soluble substance that produces solutions with a high salt–solvent ratio, for example in a 95% saturated solution at 23 °C we find a solute concentration of 30.3 mol%. In such a system where there is so much solute in solution one would expect this to be the perfect environment for solute clustering to occur. The tendency would be to lower the system energy by increasing the proportion of solute–solute interactions. The strong background scatter might suggest that there are solute clusters present within the illuminated volume, but that they cannot be resolved using the ×10 objective. To test this hypothesis the aqueous ammonium nitrate system was later investigated using higher magnification objectives (Mitutoyo, ×50, 0.55 NA and Mitutoyo, ×100, 0.70 NA, both long working-distance). When using the higher magnification setup scattering objects could then easily be identified. The particles displayed similar behaviour to those seen using the lower magnification setup for other sample solutions.

The results suggest that all of the systems investigated contain scattering particles; however, the size distribution of particles present in each sample solution can limit their chances of being observed. In addition, it is seen that a higher level of magnification is required to detect these particles in the majority of solutions with solute concentration exceeding ~ 11 mol%. Furthermore, the results suggest a relationship between solute concentration and mean particle size, i.e., formation of smaller particles is favoured at higher absolute solute concentrations. This

observation is based on a limited number of systems, therefore further work would be required to test this hypothesis.

4.3.2 Qualitative estimation of particle size

In order to obtain an estimate of the size of the particles seen during scattering experiments, a series of polystyrene spheres with mean sizes 0.1–1.0 μm was tested. It was clear that the polystyrene beads scattered very strongly. Even when using the smallest polystyrene beads (100 nm), the particles could still be identified at very low laser powers ($P \sim 3$ mW), far lower than required to observe any particles in simple salt solutions ($P \sim 50$ mW). This comparison could be taken as an indication that the particles seen in salt solutions are much smaller than the smallest polystyrene bead tested, i.e., <100 nm diameter. However, it is essential to consider the structure and shape of the scattering object before drawing such a conclusion. The intensity of scattered light from a spherical particle in the Rayleigh regime, that is, when the particle is smaller than the wavelength of incident light, is given by[50]

$$I = I_0 \frac{r^6}{\lambda^4} \left(\frac{n_2^2 - n_1^2}{n_2^2 + 2n_1^2} \right)^2 \times F \qquad (4.1)$$

where I_0 is the incident intensity, r is the radius of the particle, λ is the wavelength of incident light, n_1 and n_2 are the refractive indices of the surrounding solution and particle respectively. F is a function related to the relative orientations of the scattered light, incident beam, dipole moment and the observation point. The equation shows a strong dependence on particle size and the wavelength of incident light ($I \propto r^6 \lambda^{-4}$). In addition, there is a critical dependence on the difference of refractive index between the scattering particle and surrounding solution. Therefore for strongly scattering particles, a notable difference in refractive indices of the particle and surrounding medium would be expected ($n_2 > n_1$); similarly a particle with similar refractive index ($n_2 \approx n_1$) to the surrounding medium would be expected to scatter less strongly. Furthermore, a solid polystyrene sphere will have a sharp boundary with the surrounding solvent of lower refractive index, whereas for a solute cluster in solution a diffuse interface is expected. These considerations are particularly relevant when discussing the likely refractive index difference between a

dense solute cluster that contains a number of solvent molecules and the surrounding solvent; such a system would likely show a small difference in the respective refractive indices.

4.3.3 Quantitative estimation of particle size

Although empirical, a more appropriate estimate of particle size can be obtained by the relative differences of the Brownian motion observed for the polystyrene beads and the particles seen in concentrated solutions. The Brownian motion is a result of random molecular collisions at the surfaces of the particle which cause the particle to move randomly in the field of view. The motion of a particle can be monitored as a function of time (t) from which the mean-square displacement (MSD) of the particle is extracted. Brownian motion is an effect which acts on a particle in 3 dimensions; however in experiment particle motion is typically monitored in 2 dimensions. Therefore, when tracking a particle in 2 dimensions, the measured mean squared displacement (MSD) is related to the translational diffusion coefficient (D_t) by the relation shown by Equation 4.2.[120]

$$\mathrm{MSD}(t) = 4D_t t \tag{4.2}$$

The calculated diffusion coefficient is dependent on the size (hydrodynamic diameter) of the particle; as described by a modified Stokes–Einstein equation,[120]

$$D_t = \frac{k_B T}{3\pi\eta d_h} \tag{4.3}$$

where k_B is Boltzmann's constant, T is absolute temperature, η is the dynamic viscosity and d_h is the hydrodynamic diameter. Before performing a full analysis it was noted that the particles found in sample solutions (KCl, ammonium chloride, urea, glycine and others), appeared to move in trajectories most similar to the 100 nm polystyrene spheres than the other spheres tested; suggesting a hydrodynamic diameter of d_h ~ 100 nm. However, this is clearly a subjective observation, based on a relative comparison by eye.

With a view to performing a quantitative analysis of the recorded scattering data, particle tracking software developed by Wagner et al.[121] was employed which was adapted to suit our requirements; the software analysis is based on the Stokes–Einstein relation as described above. Additions and revision to the software were

carried out in collaboration with Wagner, T. of ref. 121. Details of the analysis can be found in Appendix C and reference 121. The performance of the software was tested with data simulated using a simple Monte Carlo sampling method.[122] The motion of the particles in all concentrated solutions tested displayed a linear drift in addition to the Brownian motion, therefore test data was simulated with and without a linear drift. The analysis performed includes a simple correction to account for the additional linear drift seen in sample solutions. Given a set of tracked trajectories composed of *N* steps the mean difference between the *x* and *y* directions are calculated over all tracks. If the tracks are solely due to Brownian motion, then the mean velocities in the *x* and *y* direction should be zero. If not, then the excess velocities in the *x* and *y* directions ($v_{x\,\mathrm{drift}}$ and $v_{y\,\mathrm{drift}}$, respectively) represent an estimate of the linear drift in the system. The minimum time interval (Δt) between measurement of particle position is determined by the video frame-rate of the footage to be analysed, i.e., the time between successive frames. The corresponding particle displacement in the *x*-direction in this time due to drift is given by $x_{\mathrm{drift}} = \Delta t \times v_{x\,\mathrm{drift}}$, and likewise in the *y*-direction. Measurements of particle position can be made at different intervals, i.e. between multiple video frames; the integer value timelag (τ) is used to represent the number of frames between particle position measurements. The drift correction used in the present work is shown in Equation 4.4. This method assumes a constant drift in the system during the period that particles are tracked.

$$\mathrm{MSD}(\tau) = \frac{1}{N-\tau}\sum_{i=1}^{N-\tau}((x_{i+\tau} - x_i - \tau \times x_{\mathrm{drift}})^2 + (y_{i+\tau} - y_i - \tau \times y_{\mathrm{drift}})^2) \quad (4.4)$$

Examples of the time lag dependence of the drift corrected MSD are shown in Figure 4.3. Each data point represents the MSD of a single particle at different time intervals ranging from $\tau = 1$ to 10. The data used is real experimental data obtained from analysis of scattering footage of 100 nm polystyrene beads and near saturated ($S = 0.95$) solutions of urea and glycine. A least-squares linear fit has been used to highlight the linearity of the MSD plots; this confirms that the particles are freely diffusing particles displaying Brownian motion.

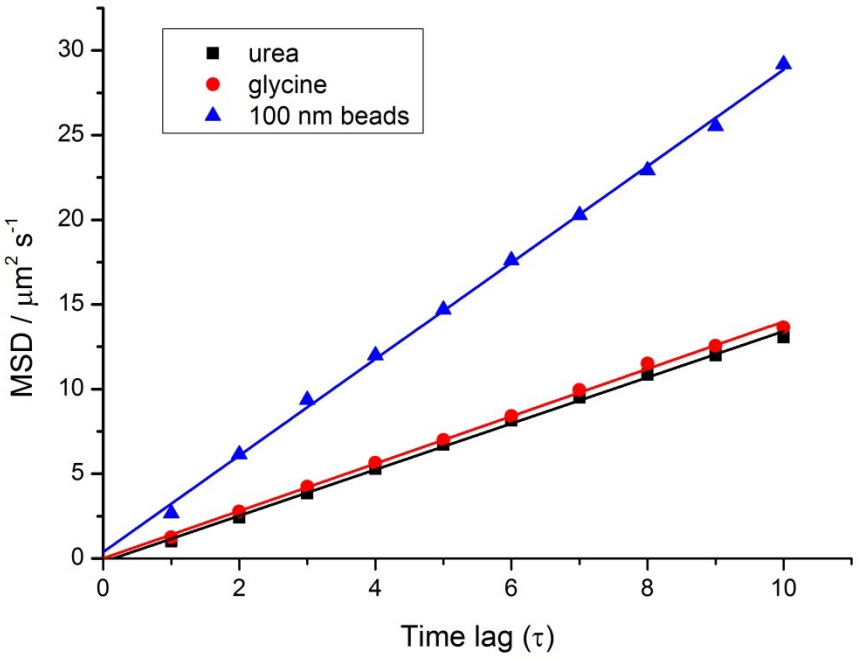

Figure 4.3 Plot showing the time-lag dependence of the measured MSD for a single particle from analysis of scattering footage of 100 nm polystyrene beads and near saturated ($S = 0.95$) aqueous solutions of urea and glycine. The plots all display a linear relationship; showing that the motion of the tracked particle is freely diffusing and Brownian. The time dependence of the MSD was checked for all samples used in NTA analysis; a linear relationship was always noted as shown above.

The results obtained from the analysis of simulated data are shown in Table 4.2, which shows excellent agreement between the expected and calculated values of d_h.

		Results	
Simulated (d_h) / nm	Relative drift / 10^{-5} cm s^{-1}	Calculated (D) / 10^{-10} cm^2 s^{-1}	Calculated (d_h) / nm
50	0	920 ± 11	50 ± 1
100	0	446 ± 6	103 ± 1
250	0	185 ± 2	248 ± 3
500	0	92 ± 1	501 ± 4
50	0.1	883 ± 11	52 ± 1
100	0.1	455 ± 5	101 ± 1
250	0.1	184 ± 1	251 ± 1
500	0.1	92 ± 1	495 ± 4
250	0.2	182 ± 2	248 ± 1
250	0.4	181 ± 2	255 ± 4
250	0.6	184 ± 1	250 ± 1

Table 4.2 Summary of the results of particle tracking analysis using simulated data of known diameter d_h. For all simulated data experimentally relevant numbers of frames (550) and a temperature of 23 °C was used. Each data set was simulated to contain 30 particles with a video spatial resolution of 166 nm $pixel^{-1}$. The errors associated with the values of D and d_h are the standard error calculated during the least-squares Gaussian fit of the D and d_h distributions provided by the tracking analysis. The results show that the analysis can successfully account for an additional linear drift in the particle system.

As a further test of the tracking software, a set of video recordings of polystyrene spheres in aqueous suspension were analysed. From this stage onwards the tracking data was analysed using the Walker method[123] which has been shown to perform well in situations where particles are tracked for relatively short period (small number of frames); a situation typically encountered for particles seen in sample salt solutions. The results are summarized in Table 4.3, where it is seen that the software does a reasonable job of estimating the particle size in some cases, but shows large error in others. Deviations from the expected values of D or d_h are attributed to the relatively low spatial resolution of the video footage used in analysis. The majority of recordings were obtained using a low level (×10) of magnification. A consequence of low magnification is that the resulting spatial resolution is relatively low (> 1 μm $pixel^{-1}$), which can lead to significant tracking errors for both large and small particles, as highlighted by the better performance when higher magnification

is used. The spatial resolution achieved for recordings of Rayleigh scattering was obtained by imaging a graticule (0.01 mm division) and establishing the scale of one image pixel. For example, the image size in a scattering experiment (×10 magnification) is 640×480 pixels. The scaled width of the image = 65.9 μm, therefore the spatial resolution = 65.9 μm / 640 pixels = 1029 nm pixel^{-1}. Details of the calculation of the resultant spatial resolution achieved in experiments are outlined in Appendix B.

				Results
Spheres (d) / nm	magnification	Frame rate / Hz	Spatial resolution / nm pixel^{-1}	Calculated (d_h) / nm
100	×50	20	181	79 ± 1
182	×10	12.3	1029	332 ± 2
530	×10	12.3	1029	404 ± 2
1000	×50	20	181	1141 ± 3

Table 4.3 Results obtained from particle tracking analysis using video recordings of the scattering observed in aqueous dispersions of polystyrene size standards. The values of d_h are the mean values of the dominant peak in the calculated distribution. It is clear that some conditions of video footage (magnification, frame rate and spatial resolution) result in a more realistic analysis; increasing spatial resolution appears to result in better performance.

Video footage suitable for analysis (181 nm pixel^{-1}) was limited to three sample solutions; 95% saturated aqueous solutions of urea, glycine and ammonium nitrate. The results of the analysis are shown in Table 4.4.

		Results	
Solution	Number of completed tracks	Calculated (d_h) / nm	Estimated particle number density / 10^7 particles cm^{-3}
Glycine	345	196 ± 1	11.55
Urea	222	268 ± 1	3.32
Ammonium nitrate	24	–	0.19

Table 4.4 Results of particle tracking analysis of footage obtained using ×50 objective lens; resulting in pixel size of 181 nm pixel^{-1}. The calculated values of d_h were obtained by peak fitting of the size distribution provided by Walker analysis[123] of the tracking data. The distribution obtained for ammonium nitrate solution shows series of peaks in the range 148–384 nm; a result of too few (24) completed tracks for analysis. Particle number density was estimated by consideration of the illuminated volume and the mean number of particles visible over 10 randomly chosen frames. The particles in question were resident in shot for long times, therefore are expected to provide a good

estimate of the number of particles per unit volume. Only 4 particles were counted in the estimate of particle number density for ammonium nitrate solution.

The results obtained for glycine samples provide a dominant peak in the range d = 132–196 nm: see Figure 4.4. This value is in excellent agreement with the value d ~ 195 nm reported by Jawor-Baczynska et al. for supersaturated (S = 1.1) glycine solutions.[23,24]

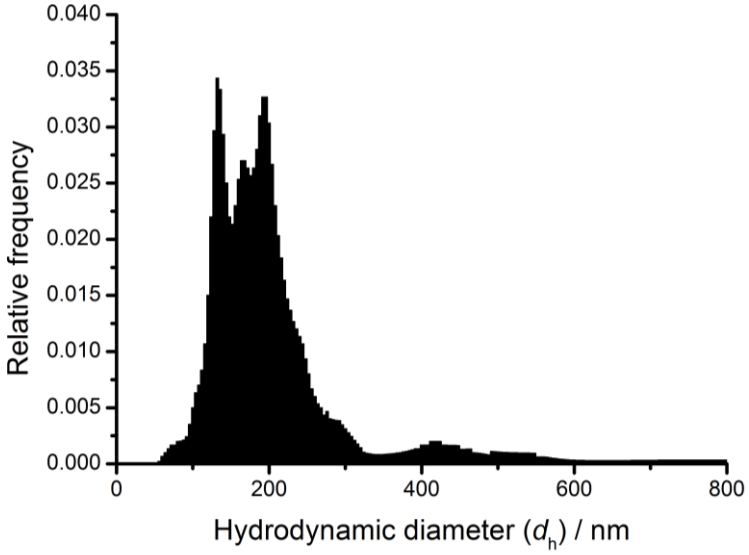

Figure 4.4 Histogram plot showing the calculated size distribution (Walker method[123]) of particles found in 95% saturated aqueous glycine solution. The plot represents the average distribution obtained by analysis of 3 sets of 550 frames at different points of the video recording.

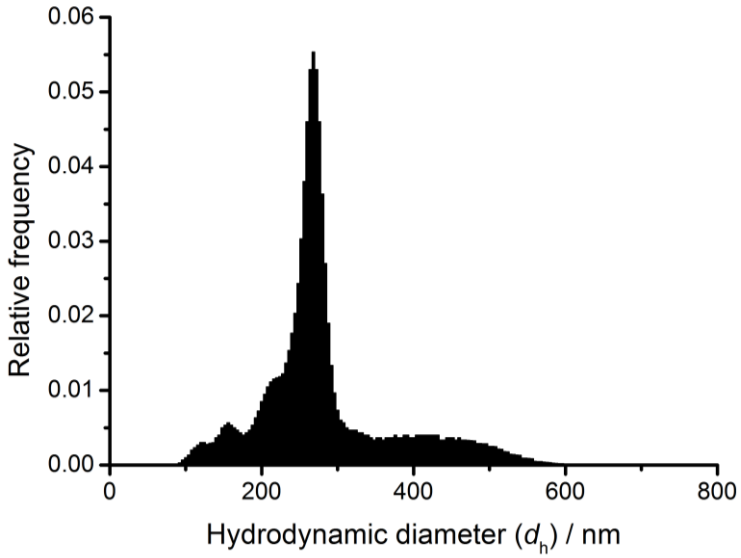

Figure 4.5 Histogram plot showing the calculated size distribution (Walker method)[123] of particles found in 95% saturated aqueous urea solution. The plot represents the average distribution obtained by analysis of 3 sets of 550 frames at different points of the video recording.

A similar peak is found for urea solutions with the dominant population found around $d \approx 268$ nm; in good agreement with the size distribution reported by Sedlác and Rak for particles observed in low concentration aqueous urea solution ($c = 0.75$ mol kg^{-1}) who report a broad distribution $d_h = 200–700$ nm.[116] The diameters reported in this thesis were obtained by analysing three sets of 550 consecutive frames taken from the video footage at different stages of the recording. For each set of 550 frames analysed it was always found that the tracking analysis identifies a population of larger particles ($d_h \sim 270$ nm) in urea solution than in glycine solutions ($d_h \sim 200$ nm).

Further analysis of the video footage allowed an estimate of the particle number density in solution to be made. The volume of illuminated solution was approximated as a cylinder with diameter of 45 μm and length 104 μm to give a volume of 2.11×10^{-7} cm^3. A series of 10 randomly chosen frames from the video recordings analysed by the particle tracking software were used to obtain mean particle counts per video frame. The particles observed in these video recordings were resident in the illuminated volume for long times, many persisting for the duration of the video (550 frames); the number of particles counted are expected to provide a good estimate of the number of particles present per unit volume of solution. Combining the value of illuminated volume and mean particle number per frame provides estimates of particle number density as shown in Table 4.4.

The estimates obtained for glycine (11.6×10^7 particles cm^{-3}) and urea (3.3×10^7 particles cm^{-3}) solutions appear systematically an order of magnitude lower than reported previously.[23,24,116] The reason for such a discrepancy is unclear, possibly associated with difficulty in counting all particles in view or estimating the volume in which particles should be visible; however the trend of the number density of particles in glycine solution being an order of magnitude greater than the density in urea solution is shown. A more accurate estimate could be performed by monitoring the scattering for a longer period of time using the method employed by Lian et al. in their study of particles in concentrated potassium dihydrogen phosphate solution.[51]

The distribution obtained from the ammonium nitrate analysis yields a series of discrete peaks spread over a large range of diameter. Unlike the footage of urea and glycine solutions, few particles were observed in solution (24 in total), resulting in a low number of completed tracks for analysis, which will lead to introduction of large uncertainties. The estimate of particle number density in ammonium nitrate solution is shown in Table 4.4 and gives an estimate of $\sim 2\times 10^{6}$ particles cm^{-3}; however, as with the estimate of particle size the value is based on the observation of a small number (4/10 frames) of particles.

As shown in Figure 4.6, the computed distribution for ammonium nitrate shows peaks at diameters comparable to the size of those found in urea and glycine solutions. This appears to go against the qualitative observation that particles in ammonium nitrate solutions must be smaller than others due to the fact that a higher level of magnification is required in order to see them. The cause of this disagreement is not clear; the footage simply does not provide enough particles to yield a reliable analysis–only 24 particles found in total (1650 frames). Alternatively, the peaks could represent an overestimation of the physical particle size; however this notion contrasts with the good performance of the analysis seen for particles found in aqueous glycine and urea solutions. It is also possible that the small numbers of particles identified by Rayleigh scattering in ammonium nitrate solution are those that compose the tail of the particle size distribution; the rest of the distribution may remain unresolved due to the combination of magnification (see Section 4.3.4) and scattering strength (see Section 4.3.2) of the particles.

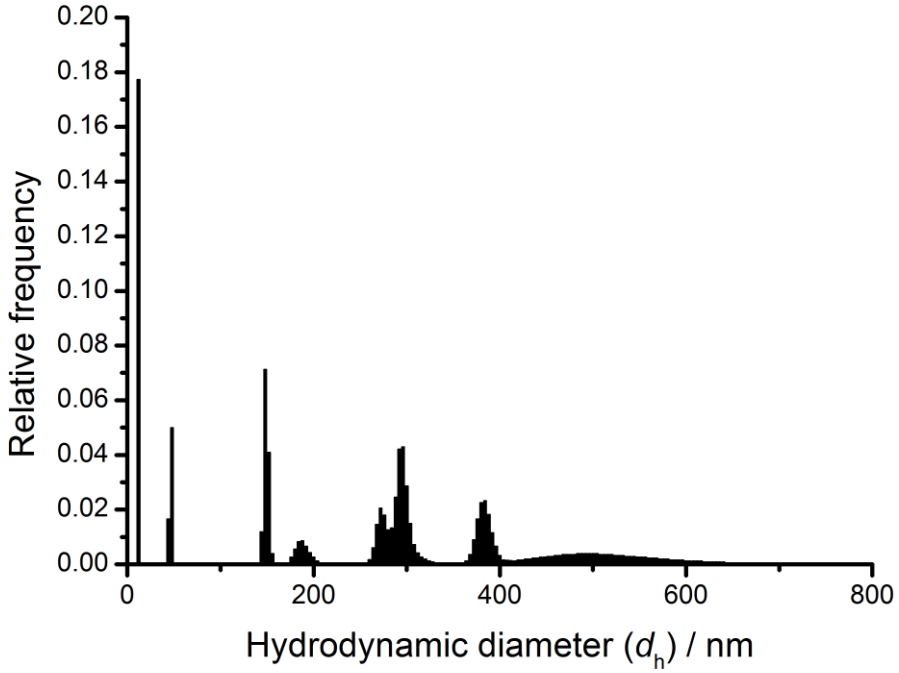

Figure 4.6 Histogram plot showing the calculated size distribution (Walker method[123]) of particles found in 95% saturated aqueous ammonium nitrate solution. The plot represents the average distribution obtained by analysis of 3 sets of 550 frames at different points of the video recording. A total of 24 tracks were identified in the video for analysis.

4.3.4 Nanosight™ analysis

In order to compare the results obtained using the bespoke microscopy setup in the laboratory, a commercial nanoparticle tracking analysis (NTA) instrument (Nanosight, LM10) was used to analyse aqueous solutions of urea, glycine and ammonium nitrate. I am grateful to the Sefcik research group at the University of Strathclyde who provided access to the Nanosight instrument for these experiments. The samples tested were prepared to have identical concentrations to those discussed in Section 4.3.3. The results obtained from the nanosight analysis are summarized in Table 4.5, which demonstrate excellent agreement with the results shown in Section 4.3.3.

	Hydrodynamic diameter (d_h) / nm	
Solution	Nanosight	Our analysis
Ammonium nitrate	–	–
Urea	238 ± 73	268 ± 1
Glycine	226 ± 66	196 ± 1

Table 4.5 Summary of the results obtained from nanoparticle tracking analysis performed using a commercial instrument (Nanosight, LM10) and the values of hydrodynamic diameter provided using our own analysis (see Section 4.3.3). The Nanosight analysis provides a particle number density weighted estimate of d_h. The values of d_h provided from our analysis of Rayleigh scattering video footage are obtained by a Walker analysis[123] of the measured particle tracking data (see Section 4.3.3). The error limits quoted for our analysis is the standard error of the peak value obtained by a non-linear least-squares Gaussian fit of the dominant peak in the size distribution. For the Nanosight analysis the error limits represent the standard deviation of estimated particle size for all tracked particles during analysis. Ammonium nitrate solution could not be analysed by NTA; too few particles or none at all (Nanosight) were seen. The estimates of d_h are in good agreement with each other and highlights the capability of our analysis to provide a realistic estimation of particle-size distribution.

No particles were detected in ammonium nitrate solutions using nanosight, which was attributed to the low level of magnification (× 20, 0.40 NA), used with the instrument. It was clear, however, that the background haze fluctuated during observations, a feature that is consistent with the presence of particles with size below the limit of resolution of the instrument ($d \lesssim 20$ nm).

The results obtained with the commercial instrument compare well with the size estimates of particles in urea and glycine solutions obtained from the analysis of video footage collected during Rayleigh scattering observations; as outlined in Section 4.3.1. This shows that the analysis developed in the present work is capable of providing reliable estimates of hydrodynamic radii of particles found in concentrated samples of salt solutions. Comparison of the two methods used highlights two key features of the video footage that could be improved to provide more reliable data using our tracking analysis; (i) increased video frame rate and (ii) minimization of pixel size. Higher frame-rate allows for longer track lengths, therefore increasing the accuracy of the resulting size estimations.[121,124] Increasing the spatial resolution is more difficult to deliver, as simply increasing the magnification simultaneously reduces the field of view and therefore track length.

In order to provide the maximum possible spatial resolution it is necessary to match the CCD resolution to the optical magnification. The maximum spatial

resolution (∅) of a microscope objective is the diffraction limited resolution, $\emptyset = (0.61 \times \lambda)/\mathrm{NA}$, where λ is the wavelength of light and NA is the numerical aperture of the objective used. Maximum resolution at the detector is achieved by matching the diffraction limited resolution (∅) of the optical system on two pixels on the CCD in each linear dimension. This requirement is called the Nyquist limit[125] (Equation 4.5) which can be used to calculate the level of magnification to use with a CCD detector with physical pixel size Ω.

$$\text{Magnification} = \frac{2\Omega}{(0.61 \times \lambda/\mathrm{NA})} \tag{4.5}$$

By inputting the values corresponding to the details used in experiment (×10 objective, 0.21 NA, λ = 532 nm, Ω = 9.9 μm) the required magnification required for maximum performance is ×12.8. This could simply be achieved by introduction of additional optical component in the optical path. However, such a change in magnification provides minimal improvement of the resultant spatial resolution (see Appendix B) of the optical system and remains poor (~1 μm pixel^{-1}). In order to increase spatial resolution whilst maintaining a relatively large field of view it would be required to increase CCD resolution and to use a moderate (slightly greater) level of magnification. For example in comparison to the ×10 objective and camera (656 × 492 pixels) used in this work (~ 1 μm pixel^{-1}); a ×20 objective in combination with a CCD with double the resolution, should yield a ~ 4 times improvement to the spatial resolution achieved. Future work in this area would benefit from a revised combination of CCD and microscope objective to enhance the capability of the setup for tracking analysis.

4.3.5 What are the scattering objects?

As shown in Table 4.1 scattering particles can be observed clearly in a wide range of sample types. The important question to ask is: what are they? Previous reports suggest these particles are solute clusters that form spontaneously in concentrated solution, and may be the precursors to the nucleation process. Laser scattering work reported by Lian et al.[51] investigated concentrated solutions near the point of saturation (see Section 1.3.5). Not only did they identify particles in a wide range of sample solutions, but for the case of KDP a clear interaction between the

scattering particle and the growing crystal of KDP was observed. Arguably, the best evidence to date has been provided by Jawor-Baczynska et al.[23,24] who investigated the aqueous glycine system. It was shown that the particles found in solutions were dense, liquid-like droplets the number of which increased significantly upon dissolution of glycine solid. In addition, the results suggested that dense droplets must reach critical dimension ($d \sim 750$ nm) for nucleation to occur.

4.3.6 Structure of the particles

During the course of experiments in this present work it was clear that some particles appeared to flash in the illuminating beam. The period of flashing was not regular for a given particle as shown in Figure 4.7.

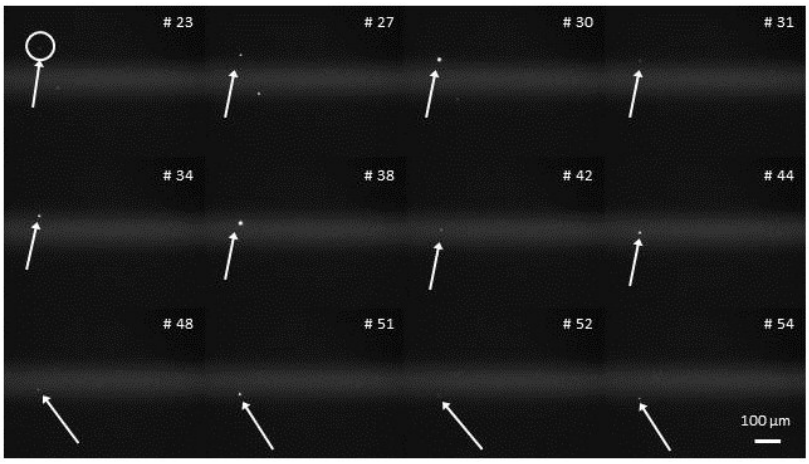

Figure 4.7 A series of stills taken from a video recording of the scattering observed in a 95% saturated solution of ammonium chloride (11.0 mol%). A single particle is highlighted in the first still (top left) and then followed as it passes through the beam. During its transit, the particle appears to repeatedly increase and decrease in intensity: in contrast to the behaviour of spherical particles.

This type of behaviour was only observed in the concentrated solute systems. When using samples of polystyrene beads, the scattered intensity remained constant for the particles transit through the scattering beam. Moreover some particles in salt solutions were seen to produce a non-uniform scattering pattern detected by the CCD camera, that is to say the scattered light did not produce a circularly spherical pattern as seen exclusively in samples of polystyrene spheres; a comparison is shown in Figure 4.8.

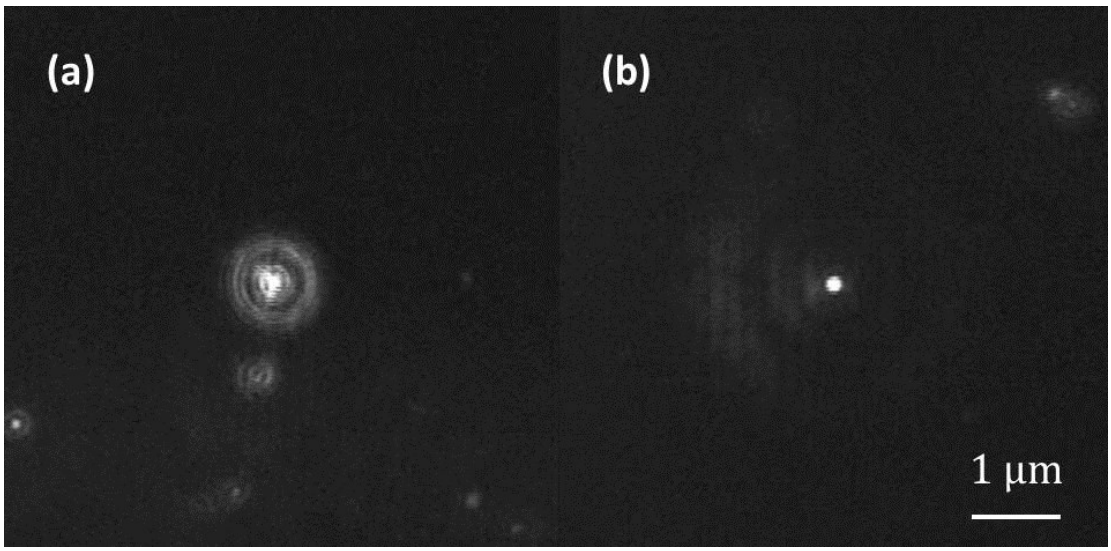

Figure 4.8 Comparison of the scattering observed from a particle in (a) nearly saturated (S = 0.95) aqueous urea solution and (b) an aqueous dispersion of 100 nm polystyrene spheres. In both cases the laser power used P = 200 mW. The urea solution was filtered (0.22 μm pore) and the dispersion of polystyrene spheres was prepared from ultrapure deionized water, also filtered (0.22 μm). The scale bar (bottom right) represents 1 μm.

Recent work by Jawor-Baczynska et al.[23,24] has suggested that scattering objects seen in aqueous samples of supersaturated glycine (S = 1.1 at 25 °C) are non-spherical, dense collections of solute molecules with an irregular surface topology. It is expected that such particles would scatter light less strongly than a solid, well-defined particle; therefore it is clear that a direct comparison with the scattering observed using polystyrene beads is not a suitable method to estimate the size of particles found in sample solutions.

These observations imply that the particles observed in these laser scattering experiments are not exclusively homogeneous or spherical in shape. A particle with non-uniform shape would rotate as it moved through solution; this behaviour would make the particle appear as if it were flashing as it passed through the scattering laser beam. For a spherical particle, the rotational diffusion coefficient (D_{rot}) in solution can be estimated using the Stokes-Einstein relation,[126]

$$D_{\mathrm{rot}} = \frac{k_{\mathrm{B}}T}{8\pi\eta r^3}. \tag{4.6}$$

A summary of the calculated values of D_{rot} for particles of different size in a liquid with dynamic viscosity $\eta = 0.903\times10^{-3}$ kg m^{-1} s^{-1} (water, $T = 23$ °C) is shown in Table 4.6.

Diameter (d) / nm	Rotational diffusion coefficient (D_{rot}) / s^{-1}	Period of rotation (τ) / s	Equivalent number of frames
20	180	0.01	0.07
100	1.44	0.69	8.54
200	0.18	5.56	68.3

Table 4.6 Estimates of the rotational diffusion coefficient for a spherical particle in water at $T = 23$ °C calculated using the Stokes–Einstein relation (Equation 4.6). The equivalent number of frames is calculated using the video frame rate (12.3 Hz) achieved during experiments using a ×10 objective.

The estimates provided in Table 4.6 are based on a simplified picture of spherical objects in a liquid. A similar scaling with particle 'size' is expected for nonspherical particles. If the flashing behaviour observed during experiments is due to particle rotation, then the apparent flashing should correlate with the period of rotation. Taking the flashing particle shown in Figure 4.3 it is seen that the scattered intensity cycles between local maxima and minima on average every 6.4 frames; implying a value of $D_{rot} = 1.91$ s^{-1} (frame rate = 12.3 Hz). Using this value of D_{rot} with Equation 4.6 and assuming the dynamic viscosity of water at 23 °C a hydrodynamic diameter of 460 nm is estimated. This value is based on only a few frames (33 frames) to monitor the apparent flashing. It is also assumed that each cycle of scattered intensity corresponds to one uniform rotation.

The results presented here are consistent with the hypothesis that **concentrated solutions contain populations of particles that are probably not spherical in shape**. With reference to other reports in the literature[23,24,46,51] the particles identified in these laser scattering experiments are attributed to solute clusters which are thought to play a key role in nucleation. However, two alternative explanations for the experimental observations should be considered: (i) that the scattering objects are nanobubbles, or (ii) that the objects may be nano-scale impurity particles. These alternatives will be discussed in the following sections.

4.3.7 Nanobubbles

It is well known that electrolytes can inhibit bubble coalescence in water.[127-130] This behaviour is generally observed at electrolyte concentrations ~ 0.1 M: a concentration exceeded in studies discussed here. An example of coalescence inhibition is the foam formed in sea water; the same does not occur in freshwater locations. Work by Craig et al. has demonstrated that this behaviour is ion-specific and dependent on the combination of cation and anion in the electrolyte.[128,131] The effect has also been reported for non-electrolytes, such as sugars and urea.[132] It was shown that anions and cations can be classified as either α or β type with αα and ββ combinations acting to inhibit bubble coalescence, while αβ and βα salts do not inhibit coalescence. The inhibition of coalescence has been attributed to specific partitioning of the ions between the bubble surface and the bulk solution. Craig et al. suggest that the observed inhibition of coalescence is due to the formation of surface-stabilized bubbles, which occurs only for certain electrolytes. The solute partitioning model (SPM) is based on the hypothesis that α-type ions are preferentially located in the bulk solution, and β-type ions are associated with the bubble surface: see Figure 4.9.

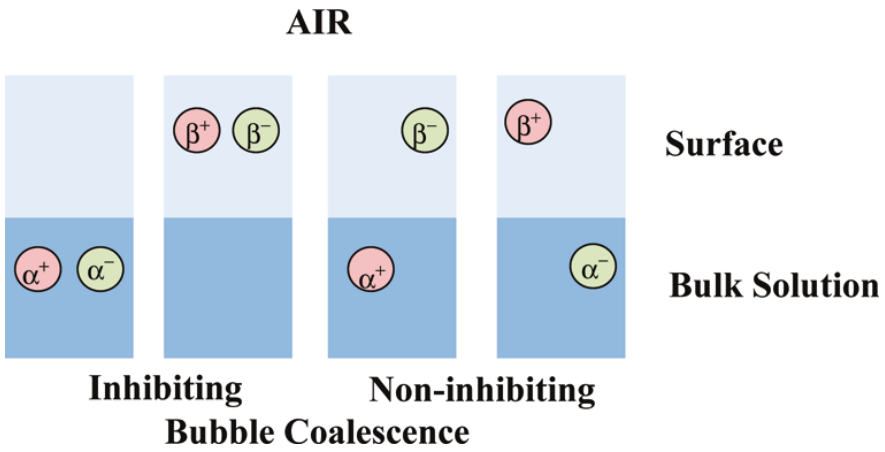

Figure 4.9 Schematic diagram (taken from ref. 131) to illustrate the Craig model of ion partitioning of α- and β-type ions at the air–solution interface. To inhibit coalescence, a combination of ions resident in the same component is required (left two panels).

It is possible that the scattering particles observed in Rayleigh laser scattering experiments may be nanobubbles that are able to survive in the concentrated salt solutions due to ion partitioning effects. Classically such bubbles should not exist

due to the extremely high internal gas pressure required, which can be calculated using the Young–Laplace equation.[133] For the case of a spherical bubble the expression simplifies to that shown by Equation 4.7.

$$\Delta P = \frac{2\gamma}{r}, \tag{4.7}$$

where the difference between the internal and external pressures is ΔP, γ is the surface tension and r is the bubble radius. Using a value of $\gamma = 0.72$ mN m^{-1} at 23 °C it is found that the excess pressure experienced by a 1.0 μm diameter bubble in water would be 2.9 atmospheres, whereas a 100 nm bubble would see an excess pressure of 29 atm. Such high pressures should lead to dissolution of the bubble in the surrounding liquid; however, recent studies have shown evidence that supports the existence of nanobubbles in bulk solution.[134-136] The validity of the Young–Laplace equation on the nano-scale has been tested by Matsumoto and Tanaka[137] using molecular dynamics simulations. They found that the surface tension and vapour pressure were practically constant, showing little dependence on bubble radius. Furthermore, considering the Young–Laplace relation Ljunggren and Eriksson[138] estimated the lifetime of a 200 nm diameter gas bubble would be ~100 μs. It is possible that if nanobubbles do form and persist in solution, that they are stabilised by action of ion partitioning effects as outlined by Craig et al.[127,128,131,132] To investigate this hypothesis a range of salt solutions with ion combinations that should and should not inhibit bubble coalescence were tested by the laser scattering using methods outlined in Section 4.2. The combinations explored are summarized in Table 4.7.

Ions		Na^+	K^+	NH_4^+	H^+	$(CH_3)_4N^+$
	Ion type	α	α	α	β	β
OH^-	α	✓	✓		×	
Cl^-	α	✓	✓		×	×
NO_3^-	α	✓	✓		×	
ClO_3^-	β	×				
ClO_4^-	β	×		×	✓	
CH_3COO^-	β	×	×	×	✓	✓

Table 4.7 Summary of the anion–cation combinations relevant to the solutions investigated in this present work. The contents of the table are based on Craig et al.[131] Gaps in the table represent ion combinations for which the bubble coalescence has not been tested. Electrolyte solutions with αα or ββ ion combinations have been shown to inhibit coalescence (marked with ticks), while αβ or βα combinations have no effect on bubble coalescence (marked with crosses).

Solution	See particles?	Bubbles stabilised?	Ion combination	mol% solute
Tetrabutylammonium perchlorate (TBAP)	yes	yes	ββ†	0.001
Tetramethylammonium perchlorate (TMAP)	yes	yes	ββ	0.12
Potassium dihydrogen phosphate	yes	–	–	2.92
Ammonium perchlorate	**yes**	**no**	**αβ**	**3.33**
Glycine	yes	–	–	5.12
Sucrose	yes	yes	αα*	5.20
Potassium chloride	yes	yes	αα	7.41
Ammonium chloride	yes	yes	αα	11.0
Sodium chlorate	no	no	αβ	13.7
Tetraethylammonium chloride (TEAC)	**yes**	**no**	**βα†**	**15.4**
Sodium perchlorate	no	no	αβ	22.2
Urea	yes	yes	αα*	24.5
Ammonium nitrate	**no**	**yes**	**αα**	**30.3**
Potassium acetate	**yes**	**no**	**αβ**	**31.5**
Acetamide	no	–	–	54.1

Table 4.8 List of the sample solutions inspected using the low magnification (×10 objective). The ion combination column refers to the Craig[128] assignments of anion and cations. Combinations of αα or ββ are expected to stabilise bubbles; αβ or βα combinations should not stabilise bubbles. The table rows in bold highlight the cases where laser scattering observations conflict with the potential for bubble stabilization. Ion combinations marked with an asterisk (*) are non-electrolytes for which the bubble coalescence has been studied elsewhere.[132] Ion combinations marked with a dagger (†) have not been tested for bubble coalescence, but are categorized based on the assignment of the tetramethylammonium cation as β-type.

The results shown in Table 4.8 show no clear correlation between samples that show scattering particles and those that should or should not stabilize bubbles. A total of 12 samples tested in this work have a known effect on bubble coalescence in solution. From this set, 8 solutions show a positive correlation between their effect on bubble stabilization and the presence of particles observed in scattering

experiments. It is important to highlight that these observations were made using a low level of magnification (x10 objective). As has been shown for ammonium nitrate solution a higher magnification was required to observe particles. It may be the case that a higher magnification would allow identification of particles in other solutions too, i.e., acetamide, sodium perchlorate and sodium chlorate. It is clear that further work in this area would be required in order to rule out the possibility that the scattering objects seen in scattering experiments are or are not stabilised nanobubbles in solution. Furthermore it is important to highlight that all sample solutions studied in the laser-scattering work were filtered using a 0.22 μm syringe filters: these filtration units are regularly used for degassing solvents used in HPLC. However, it is not known how efficient this degassing procedure would be for nanobubbles, assuming that they exist.

4.3.8 Impurities

Another explanation for these scattering objects is that they are insoluble impurity particles in the sample solution. During the course of experiments several control measures were taken to investigate the origin of the particles found in solutions. After cleaning the sample cell was filled with filtered (0.22 μm) ultrapure water and inspected using the laser scattering apparatus. The cell was considered clean if no particles were observed, even at the highest laser powers ($P \sim 200$ mW). If particles were seen the cleaning process was repeated until a clean sample was produced; these particles were attributed to dust. The efficiency of the filtering process was inspected as a source of the scattering particles. The performance of a number of different syringe filter units which differed by brand or membrane type were assessed by filtering solutions of glycine and urea; the filtrate then tested for the presence of particles by laser Rayleigh scattering as described in Section 4.2. Each type of filter was seen to have the same effect for each solution, i.e. all did or all did not result in particles in solution.

For samples that provided a solution with particles, a new filter of the same type was used to filter a sample of ultrapure water; the resulting sample was always free from abundant particles as found in sample solutions. It is recommended that a few mL of sample solution is passed through the filter units prior to collection of

filtrate: this protocol was always followed. As further tests, samples of urea solution which showed particles were filtered using a filter that had been previously flushed through with 500 mL of ultrapure water, and a filter flushed with 200 mL of sample solution before filling the sample cell; both procedures produced a solution with particles as seen previously.

The most likely source of any impurity particles in the sample was identified as the solid material used to prepared solutions. The solids used in preparation of solutions used in these experiments are typically of high purity (ACS, > 99.9%) with trace elements varying from solid to solid. There appears to be no correlation with samples that do and do not show scattering objects. The impurities found in the bottled solids likely result from the starting materials and the process of manufacture. Therefore, it is reasonable to suggest that solids that are similar in composition would contain similar impurities. Looking at the scattering results (×10 objective) obtained for solutions of ammonium nitrate and chloride (Table 4.8) it can be seen that particles are clearly observed in the chloride, however nothing is seen for the nitrate. Similarly, it is seen that particles were identified in solutions of ammonium perchlorate, but none found in sodium perchlorate solutions. In these pairs of chemicals, the samples that do not show scattering objects in solutions are those with the higher absolute concentrations, which might be expected to have a greater likelihood of introducing solid impurities to the sample solution.

Impurity particles introduced via the solute would have a maximum size of ~0.22 μm (pore diameter of syringe filters): this is comparable in size to the smaller polystyrene size standards tested. It is expected that solid particles of this size would scatter light strongly, as seen for the polystyrene spheres; however the particles found in sample salt solutions scatter with far lower intensity. This observation suggests that the particles found in sample solutions are unlikely to be solid impurities comparable in size to the spheres (d > 100 nm) used in experiments. The possibility that the impurities may be soluble in water, but insoluble in concentrated salt solution has also been considered. The 95% saturated sample solutions were prepared in advance and allowed to cool to the experimental temperature before use. If impurity particles had formed in solution during the cooling process the subsequent filtering process would remove particles > 0.22 μm diameter.

It would be of great benefit to identify the composition of the particles found in scattering experiments; however the low number density of scattering particles and the high solute concentration in sample solutions rule out routine analysis such as mass spectrometry. It is known that the population of scattering particles seen by laser scattering can almost be removed completely in aqueous glycine solution by filtration.[23,24] If the particles seen in other solution systems can also be removed by this type of filter it may be possible to collect the scattering objects by filtering a large volume of sample solution. After removal of excess solution by flushing, the trapped filtrate may then be probed by a technique such as scanning electron microscopy (SEM) or X-ray fluorescence (XRF) spectroscopy. Such experiments are currently ongoing in the Alexander group.

4.4 Conclusions

In summary, a wide range of concentrated aqueous solutions have been investigated using a Rayleigh laser scattering technique. Populations of scattering objects could be detected in almost all sample solutions using a low level of magnification (×10). The detected objects appear long-lived and able to move freely through solution. Some solutions were also investigated using a higher magnification (×50), all of which showed a population of scattering particles, including ammonium nitrate solution in which no objects were seen using the lower magnification. It is expected that all sample solutions contain these scattering objects; however, the size distribution of objects in a given system determines the resolving power required for imaging.

Video footage recorded during laser scattering experiments was analysed using modified particle-tracking software. The estimates of particle size obtained are in good agreement with the value reported in the literature, and with the results produced using a commercial instrument (Nanosight NTA). However, the methods employed to estimate the mean particle size in this work differ from those used in the commercial analysis, therefore care must be taken when comparing the results directly. Comparison of the performance of the Nanosight instrument and the laser scattering setup used in this work has allowed several key improvements to be

identified that would allow creation of a reliable and low-cost alternative to the expensive commercial analysis package.

The observations made during this work are in agreement with those made in other laser scattering experiments in which the identified particles were attributed to pre-nucleation clustering. The possibility that the scattering objects seen in experiment are long-lived, stabilised nanobubbles was investigated. The results presented here show no certain correlation with the results of previous studies of bubble coalescence and do not allow the possibility of persistent nanobubbles to be ruled-out. However, it is noted that the objects identified in concentrated solute systems scatter far less strongly than small (100 nm) polystyrene spheres; an indication of low refractive index difference between particles and surrounding solution. Furthermore, evidence of non-spherical particles in solution was found in this work. These observations contrast with the expected behaviour of nanobubbles in solution.

Chapter 5: Second-harmonic scattering in aqueous urea solutions: evidence for solute clusters?

5.1 Introduction

As evidence in support of the 2SM of nucleation grows,[8,5] it is becoming increasingly accepted that nucleation in general occurs via a 2-step pathway. The first step sees formation of dense regions of solute or metastable clusters that are expected to be liquid-like in structure and may include solvent; the second step involves a structural reorganization or nucleation within the solute-rich domains. There are many reports that provide indirect evidence of the existence of these clusters from studies including diffusivity measurements,[47,117,118] Raman spectroscopy,[119] small-angle neutron scattering (SANS),[71,70] static (Rayleigh) light scattering[49,50] and dynamic light scattering (DLS).[24,23,48,139] Other experiments, however, suggest that clustering is not at all prevalent.[68] It is clear that in most of the systems investigated using light-scattering techniques there exists a population of particles on the nano-scale; however, fundamental knowledge of the structure and composition of these particles remains unknown. Assuming that the particles found in solutions are solute clusters, key questions raised are: what is the internal structure of a typical cluster? Are solute clusters completely disordered, or do they contain an ordered (e.g., crystalline) component?

In crystalline form, a material can be described as centrosymmetric or non-centrosymmetric depending whether the crystal structure contains an inversion centre or not.[140] These two different crystal classes are routinely distinguished by taking advantage of a particular optical property of non-centrosymmetric materials: bulk second harmonic generation (SHG).[141] SHG is a non-linear optical response to an intense coherent optical field (e.g., laser light) that results in doubling of the frequency of the incident light. In the electric-dipole approximation, SHG requires the incoming and outgoing photons to be phase-matched in a material with a non-zero second-order susceptibility tensor $\chi^{(2)}$. This is a highly efficient method to determine crystal symmetry as SHG is forbidden in bulk centrosymmetric media due to symmetry considerations. It is also possible to observe SHG at the surface (or

interface) of a centrosymmetric material, as the local symmetry is broken. The disordered, homogeneous nature of an aqueous solution would be expected to preclude bulk SHG. However, second-harmonic scattering (SHS) may also be observed in liquids due to hyper-Rayleigh scattering (HRS), which is caused by local density and orientation fluctuations.[142,143] On the timescale of the incident laser pulse fluctuations in the liquid or solution can lead to a transient structure with non-zero hyperpolarizability. The proceeding scattering is spontaneous process and is analogous to Rayleigh scattering where the emission is at the second harmonic frequency.

Following the work discussed in Chapter 4, the aqueous urea system was selected as an ideal system for further study as it contains a population of easily identifiable particles. There is only one known crystal polymorph of urea at ambient pressures[144] and the crystallographic space group is $P\bar{4}2_1m$,[145] which is non-centrosymmetric and second-harmonic active. In the case of urea, if the particles identified in laser scattering experiments are solute clusters and they have a crystalline component, it is likely to be that of the known solid phase and therefore second-harmonic active. With a view to detecting these particles and probing their internal structure in aqueous (metastable) supersaturated urea solutions a series of SHS experiments were carried out; the results of which are discussed in this Chapter, and have been published elsewhere.[146]

5.2 Experimental

Measurements of SHS were made using microscopy based on a fluorescence-lifetime imaging setup that has been described in detail previously.[147] The light source used was a diode-pumped Ti:sapphire laser (Coherent, Verdi V18 and Mira F900) which produced 180 fs pulses of 800 nm light at a repetition rate of 75 MHz. The beam was introduced to the inverted microscope where it was then tightly focussed by a water-immersion microscope objective (×60, NA 1.2) in to the sample cell, which was mounted on a motor-controlled translational stage (Marzhauzer Wetzlar GmbH & Co. KG, SCAN IM120 × 100). Photon scattering was collected through the same objective and detected using an external fast micro-channel plate photomultiplier tube (Hamamatsu, R3809U-50). Emission was recorded using time-

correlated single photon counting (TCSPC) through a computer interface (Becker and Hickl, SPC830). A series of optical filters were used to control the wavelength range detected. A visible band-pass filter was used to block the pump beam while allowing detection of wavelengths in the range 340–610 nm. In addition, different interference filters were used to detect narrow bands at 400 ± 40, 450 ± 40 and 458 ± 10 nm (Comar optics 400IU25, 450IU25 and 458IL25 respectively). The emission was detected without selection of polarization. Collection of SHS was investigated in the forward direction using a second objective lens; however, it was found that the signals obtained were fractionally lower. The lower collection efficiency may be attributed to the difficulty in aligning un-matched objectives. Laser powers reported here were those measured before the objective lens: 1 mW corresponds to a single peak power density of ~50 GW cm^{-2}.

Sample cells were produced by gluing glass rings (17 mm diameter × 4 mm tall) to a circular cover glass (No. 1.5) using Norland optical adhesive (Norland Optical Adhesive 61). Two different sources of urea solid were used during experiments, one from VWR (BDH, AnalR grade) and the other from Sigma Aldrich (puriss p.a. ACS grade, 99.8%). Sample solutions were prepared with supersaturation ranging from $S = 0.15$ to 1.86 at the experimental temperature of 21 °C, where the saturation concentration is calculated as $C_{sat} = 18.14$ mol kg^{-1}. The sample solutions were filtered using a 0.22 μm-pore syringe filter (Millex GS), allowing a few mL to pass before placing a droplet (volume ~0.02 cm^3) in the centre of the sample cell; the cell was then immediately sealed with another cover glass. Samples were allowed to cool to the experimental temperature (21 °C) before investigation.

For comparative experiments, aqueous dispersions of known SHG-active nanoparticles were prepared. Barium titanate nanoparticles ($BaTiO_3$, 99.9%, tetragonal phase) were purchased from Nanostructured and Amorphous Materials Inc. (Houston, TX). The particles were approximately spherical in shape, with mean diameter, $d = 200$ nm. To disperse the particles, 8 mg of $BaTiO_3$ was added to 11.6 g of urea solution (2.72 mol kg^{-1}) followed by shaking and sonication. 1.00 g of the crude stock was filtered through a 0.22 μm syringe filter in to 8.50 g of urea solution (1.02 mol kg^{-1}). The resulting solution contained $BaTiO_3$ nanoparticles ($d < 200$ nm)

in 1.19 mol kg^{-1} urea solution. Successful dispersion was verified by the microscope; no further analysis was carried out.

The data collection involved integrating the time-dependent TCSPC photon counts over a fixed period of time. In order to probe a large volume of solution the motor controlled *xy* sample stage was used to scan the sample through the fixed focal point of the objective. The sample stage was programmed to scan the sample through a series of translational steps (shown schematically in Figure 5.1): along the *x* direction for 1 mm followed by a 2 μm step in the *y* direction, and so on.

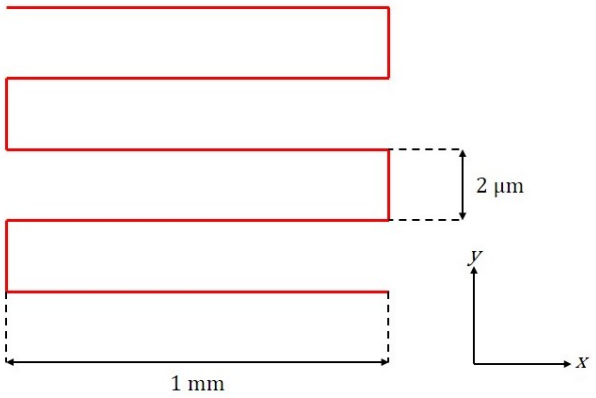

Figure 5.1 Schematic (not to scale) showing the scanning pattern used when translating the sample cell through the focal volume of the probe laser beam. The sample is translated 1 mm in the *x*-direction followed by a 2 μm step in the *y*-direction. The sample cell and laser components are not shown for clarity.

During measurements, the focal plane was maintained at a depth of around 100 μm above the droplet–cover glass interface. The photon count was continually integrated during the scanning procedure.

5.3 Results

The experimental setup was optimized using a sample of crushed, crystalline potassium dihydrogen phosphate (KDP), which is a highly efficient second harmonic active material.[141] The TCSPC time-dependent photon count is shown in Figure 5.2, the trace shows a sharp signal peak at $t = 1$ ns which is attributed to SHG at 400 nm using the 800 nm pump beam, and represents the instrument response function. The signal peak can be fitted with a Gaussian function with full-width at half-maximum

(FWHM) of 55 ps. The same KDP sample was regularly inspected to verify the instrument response over the course of experiments.

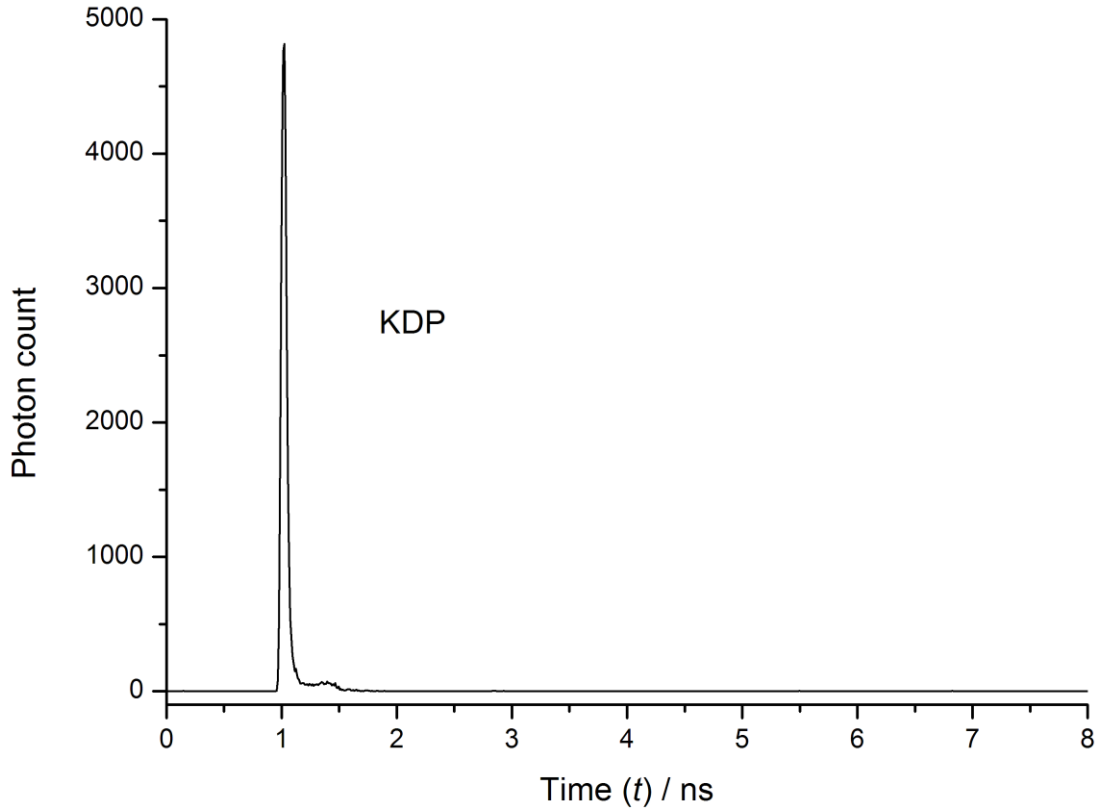

Figure 5.2 Time-dependent photon count for solid potassium dihydrogen phosphate crystals. The peak is attributed to second-harmonic generation at 400 nm using an 800 nm pump-pulse train (laser power, P = 0.7 mW, 10 s integration). The shape of the peak represents the instrument response function and can be fitted using a single Gaussian function with full-width at half-maximum (FWHM) of 55 ps.[146]

Samples of water and slightly undersaturated (S = 0.98) urea solution were tested for second harmonic scattering, the traces obtained are shown in Figure 5.3. For the water sample, the trace shown was collected using a visible band-pass filter, and shows no clear peak at t = 1 ns. The urea trace obtained using a narrow-pass 400 nm filter shows a clear peak at t = 1 ns. A Gaussian fit of this peak provides a FWHM = 43 ps, which is very similar to the value obtained for KDP. To rule out the possibility that the peak observed in Figure 5.3 is due to a broadband emission, data was collected using a 458 nm narrow-pass filter; no peak was observed, supporting the argument that the signal seen from urea solution is SHS at 400 nm.

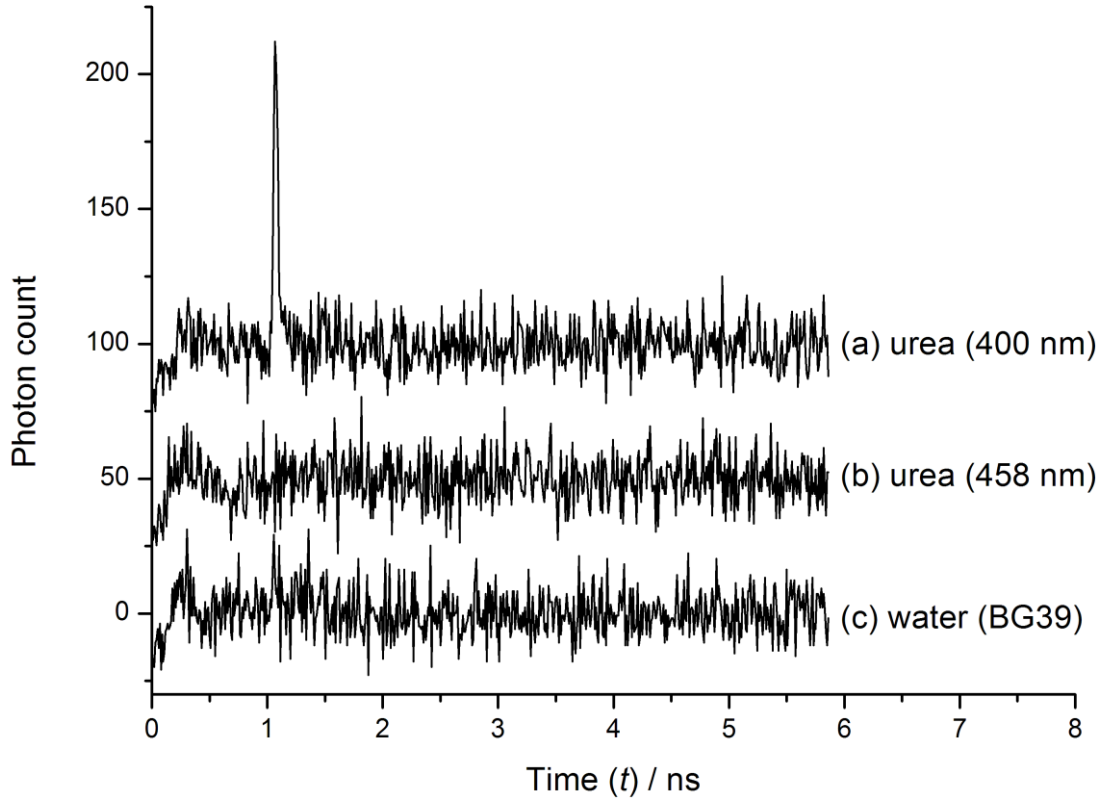

Figure 5.3 Time-dependent photon counts for undersaturated urea solutions (S = 0.98) and water. All traces were obtained with integration time of 180 s while scanning the droplet through the probe beam using identical laser powers (P = 3.8 mW). Trace (c), for water, was acquired using a visible band-pass filter (BG39). Traces obtained for urea solutions were acquired using (a) 400 ± 40 nm and (b) 458 ± 10 nm interference filters, respectively. The peak in (a) can be fitted using a Gaussian function with FWHM of 43 ps.[146]

Analysis of the data found that the total SHS signals ($I_{2\omega}$) collected from water and urea solution (S = 0.98) showed a quadratic dependence on the incident laser intensity (I_0), i.e., $I_{2\omega}^{(\mathrm{SHS})} \propto {I_0}^2$, consistent with a 2-photon process. One possible artefact could be plasma generation due to multiphoton absorption at the focal point. Although the temporal profile of such a plasma emission is expected to be similar to that seen for SHS, it is important to highlight that the laser power densities used in this work are orders of magnitude lower than required for solvent breakdown.[80] Furthermore, the contrasting results obtained using 400 and 458 nm filters show that the signal is due to a narrow-band emission, not a broadband signal that would be expected for plasma emission.

Other possible sources of SHS include SHG directly from the coverslip, or at the coverslip–droplet or droplet–vapour interfaces. At the same powers (P = 3.8 mW) used to obtain the traces in Figure 5.3, a small signal was seen with water when focussed on the coverslip–droplet interface. This signal was removed by moving the focus a depth of ~20 μm further in to the droplet. Increasing the laser power to P = 10 mW saw a signal even at 20 μm into the droplet, the intensity of which was found to decrease with increasing depth in to the droplet. The signals observed at close proximity to the coverslip are attributed to surface SHG at the coverslip–droplet interface, with increasing HRS expected from the samples at higher laser powers (as discussed below). To avoid collection of any interfacial SHG, the measurements reported here were performed at sufficient powers (< 4 mW) and depths (~ 100 um) to avoid interference; these parameters were verified regularly during experiments.

As well as urea, attempts were made to measure SHS from aqueous samples of glycine and sucrose. The TCSPC time-correlated photon counts obtained for both samples show a peak at t = 1 ns, followed by a long decay with sufficient intensity to mask any underlying SHG signal. An example of this is shown in Figure 5.4, where the trace obtained for glycine solution is presented.

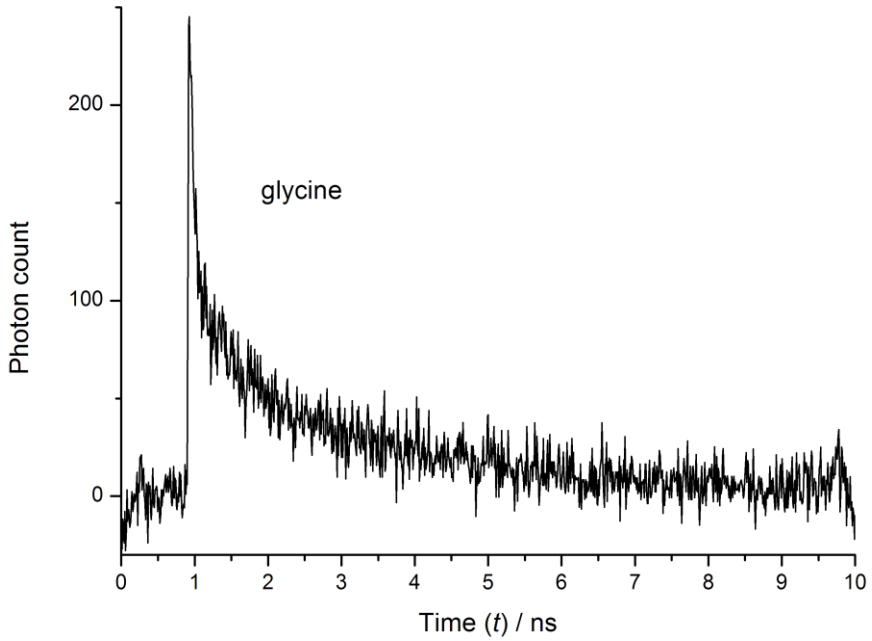

Figure 5.4 Time-dependent photon count for undersaturated glycine solution (S = 0.95). The signal was integrated for 180 s while scanning through solution using a laser power of P = 4.0 mW. The decay of the trace can be fitted with two exponential functions (lifetimes, τ_1 = 0.16 ns and τ_2 = 2.16 ns).[146]

Looking at the reported electronic structure of glycine, no absorption bands of an appropriate energy were found to account for the apparent 2-photon fluorescence observed in this work.[148] It may be possible that aggregation of glycine monomers in the concentrated sample solution is the cause of the fluorescence. These systems were not investigated any further for this work and in the absence of further data the emission is attributed to trace impurities in the samples used.

5.3.1 Concentration dependence

A study of SHS from urea solutions with a range of supersaturations $S = 0.15–1.86$ was carried out, and the results are shown in Figure 5.5. The results show a non-linear increase of signal with supersaturation, approaching a local maximum at $S = 0.95$ then decreasing up to $S = 1.35$; the signal then increases up to $S = 1.75$, and drops at the highest supersaturation tested ($S = 1.86$). The signal intensity does not increase monotonically as would be expected for hyper-Rayleigh scattering,[149] and is a strong indication that the signal measured is inherent to the structure of the sample solution. The local maximum identified near the point of saturation ($S = 0.95$) is of particular significance, as it potentially highlights a change of the solution structure at this point. Diffusivity measurements on urea solutions performed by Sorell and Myerson saw a rapid decrease above saturation with the change attributed to solute cluster formation.[118]

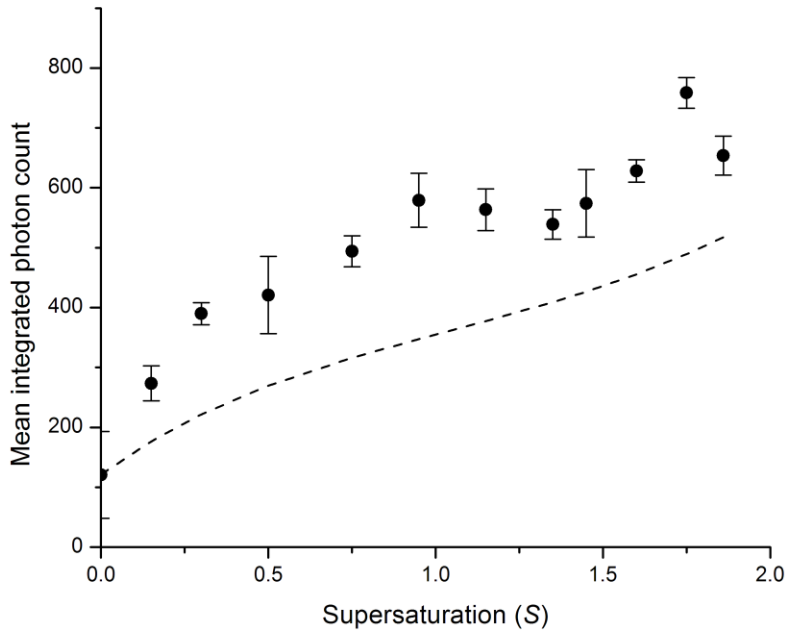

Figure 5.5 Results of a concentration dependence study of SHS signal from urea solutions. The laser power used was P = 3.8 mW with the laser focal depth maintained at ~ 100 μm above the cover glass interface. SHS signal was measured during scanning with an integration period of 180 s per trace. For each trace a baseline was estimated by averaging data from 2 to 3 ns (*cf.* Figure 5.3) and this was subtracted from the data. The total photon count under the peak was integrated. The mean values of these signal counts, calculated from repeat measurements, are shown by the black circles. Error bars represent 95 % confidence intervals from repeat measurements. The dashed line represents model calculations of hyper-Rayleigh scattering, which have been scaled by a constant factor to match the experimental data at the point S = 0 (water).[146]

The analysis of the data shown in Figure 5.5 was completed by computing the contribution of hyper-Rayleigh scattering to the measured signal. The total intensity of HRS ($I_{2\omega}^{(\mathrm{HRS})}$) can be determined using $I_{2\omega}^{(\mathrm{HRS})} = G{I_0}^2B^2$, where G is a proportionality constant containing geometrical and electronic factors and I_0 is the incident intensity[149]. For a two-component system the B^2 term can be written as,

$$B^2 = N_{\mathrm{solute}}\langle{\beta_{\mathrm{solute}}}^2\rangle + N_{\mathrm{solvent}}\langle{\beta_{\mathrm{solvent}}}^2\rangle \qquad (5.1)$$

where the N term represents the molecule number densities of each component and $\langle\beta^2\rangle$ is the corresponding laboratory-frame average of molecular-frame hyperpolarizabilities. Values of $\langle\beta^2\rangle$ are evaluated as $\langle\beta^2\rangle = \langle{\beta_{ZZZ}}^2\rangle + \langle{\beta_{XZZ}}^2\rangle$ where the terms on the right represent the rotationally averaged molecular-frame hyperpolarizabilities.[150] The description of the hyperpolarizability for HRS is dependent on the molecular symmetries. Urea and water share a common space

group (C_2v) for which the diagonal β_{ZZZ} and non-diagonal β_{XZZ} coefficients of the hyperpolarizability tensor are required to compute the laboratory-frame, space averaged hyperpolarizability $\langle\beta^2\rangle$. Values of $\langle\beta^2\rangle$ were calculated using theoretical values of the molecular-frame terms[151,152] to give $\langle{\beta_{\text{urea}}}^2\rangle = 0.14 \times 10^{-30}$ esu and $\langle{\beta_{\text{water}}}^2\rangle = 0.011 \times 10^{-30}$ esu. These values were then used to calculate the expected concentration dependence contribution of hyper-Rayleigh scattering to the measured signal. The result of this was scaled by a constant factor to match the experimental results at $S = 0$ (pure water sample) and is shown in Figure 5.5 by the dashed line. It can be seen that the general trend of the HRS model follows that of the experimental data; however at higher supersaturations the experimental points differ significantly from the HRS model.

5.3.2 Source of SHS signal

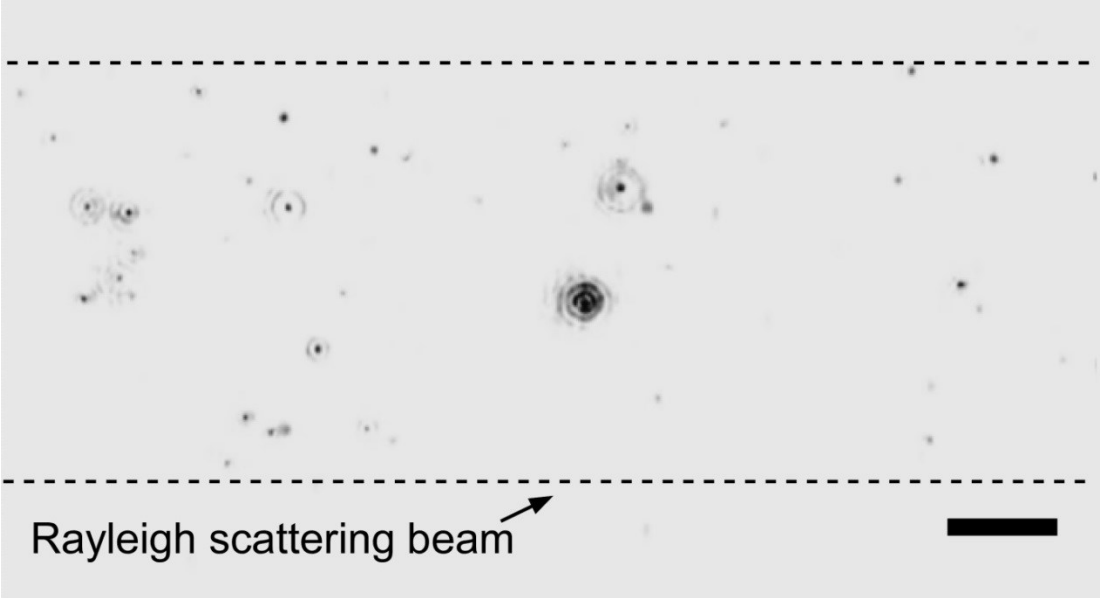

Figure 5.6 Image taken from a video recording of the Rayleigh scattering observed in undersaturated urea solution ($S = 0.95$). The 488 nm beam ($P = 55$ mW) was focussed into solution using a lens (focal length = +200 mm) and the Rayleigh scattering imaged at right angles through an objective (×50). The scale bar (bottom right) represents 10 μm.

Using procedures outlined in Section 4.2 the Rayleigh scattering from urea solutions (as used in SHS microscopy) was measured that showed a population of free particles in solution, as shown in Figure 5.6. In order to determine if the SHS signal measured during initial experiments may have originated from the particles

identified by laser scattering, the experiments were repeated with a shorter integration time of 0.2 s (compared to 180 s used during initial experiments). The results obtained from a series of 2000 traces from a slightly undersaturated (S = 0.98) urea solution are shown in Figure 5.7. The plot shows a series of peaks encountered during the scanning process. Figure 5.7 (b) shows the total time-dependent photon count obtained by summing all constituent traces of Figure 5.7 (a). The summed trace clearly shows a single peak at t = 1 ns with intensity comparable to that shown in Figure 5.3. This result demonstrates that the SHS signal obtained in experiments is the result of many smaller events encountered during the scanning process, and further supports the idea that the SHS signal is intrinsic to the sample solution and not a result of surface or interfacial effects.

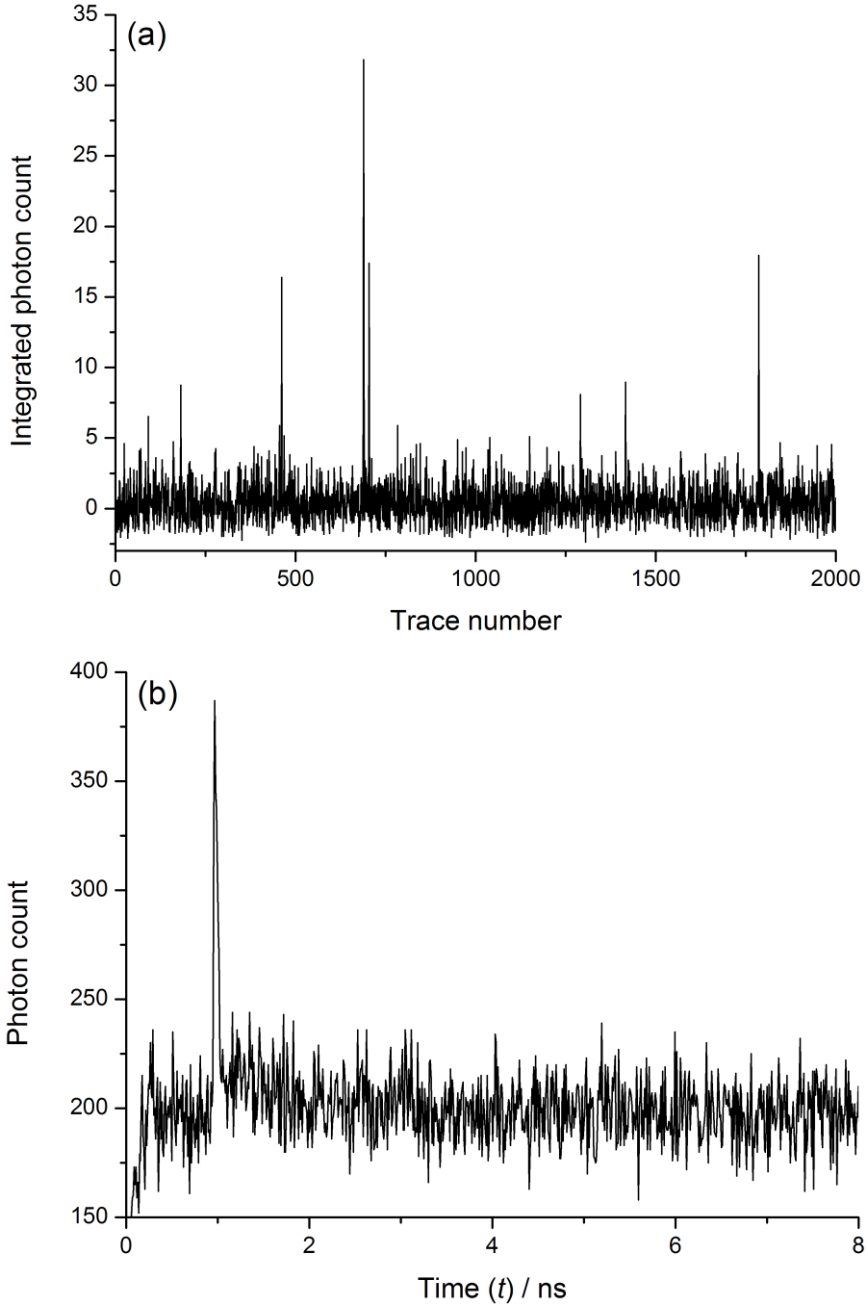

Figure 5.7 (a) Integrated peak photon counts from a series of consecutive traces taken while scanning through urea solution ($S = 0.98$). The integration time for each trace was 0.2 s. The photon count under the peak in each trace was integrated as detailed in Figure 5.5. The pump-laser power was $P = 3.4$ mW. The total signal from summing over all 2000 traces is shown in (b). The peak at ~ 1 ns is the SHS signal. The result suggests that the total signal originates from individual peak events encountered during scanning.

The data shown in Figure 5.7 was collected over a period of approximately 400 s, with the scan covering a linear distance of approximately 0.18 m. If a focal volume

width of 400 nm and depth of 600 nm is assumed, the total volume probed during the scan was 4.3×10^{-14} m^3. Setting an arbitrary threshold photon count and assigning one particle to each of the peaks allows 7 particles to be identified. Considering the volume probed during the scan, this equates to roughly 1.6×10^8 particles cm^{-3}. This estimate is in good agreement with the value reported by Lian et al. who measured 1.3×10^6 particles cm^{-3} for supersaturated KDP ($S = 1.001$) solution using Rayleigh scattering[51]. It is expected that the number density of solute clusters would show some dependence on solute type. A recent study of the aqueous glycine system[24] ($S = 1.08$ at 25 °C) measured a population of $\sim 10^9$ particles cm^{-3}. Considering the volume illuminated by the scattering beam, measurements of Rayleigh scattering in the present work (Figure 5.6) suggest a population of 2.9×10^8 particles cm^{-3}, in good agreement with the values estimated here.

The results so far suggest that the SHS signal detected here originates from free particles that are present in the sample solution; however the structure of these particles remains unknown. With the aim of obtaining some information of the structure of the SHS objects in urea solutions, samples containing particles of SHG-active material of known size and shape were tested. Dispersions of $BaTiO_3$ nanoparticles were used for this study. The nanoparticles were well-characterized with a mean diameter of 200 nm and approximately spherical in shape. The results obtained for the $BaTiO_3$ and aqueous urea ($S = 0.98$) samples are compared in Figure 5.8. The data shown was collected with an integration time of 10 s for each trace and shows peaks approximately 20 times greater for the $BaTiO_3$ sample than the urea sample. As a control, samples of water were tested using identical procedures and showed no peaks as seen for the $BaTiO_3$ and urea samples.

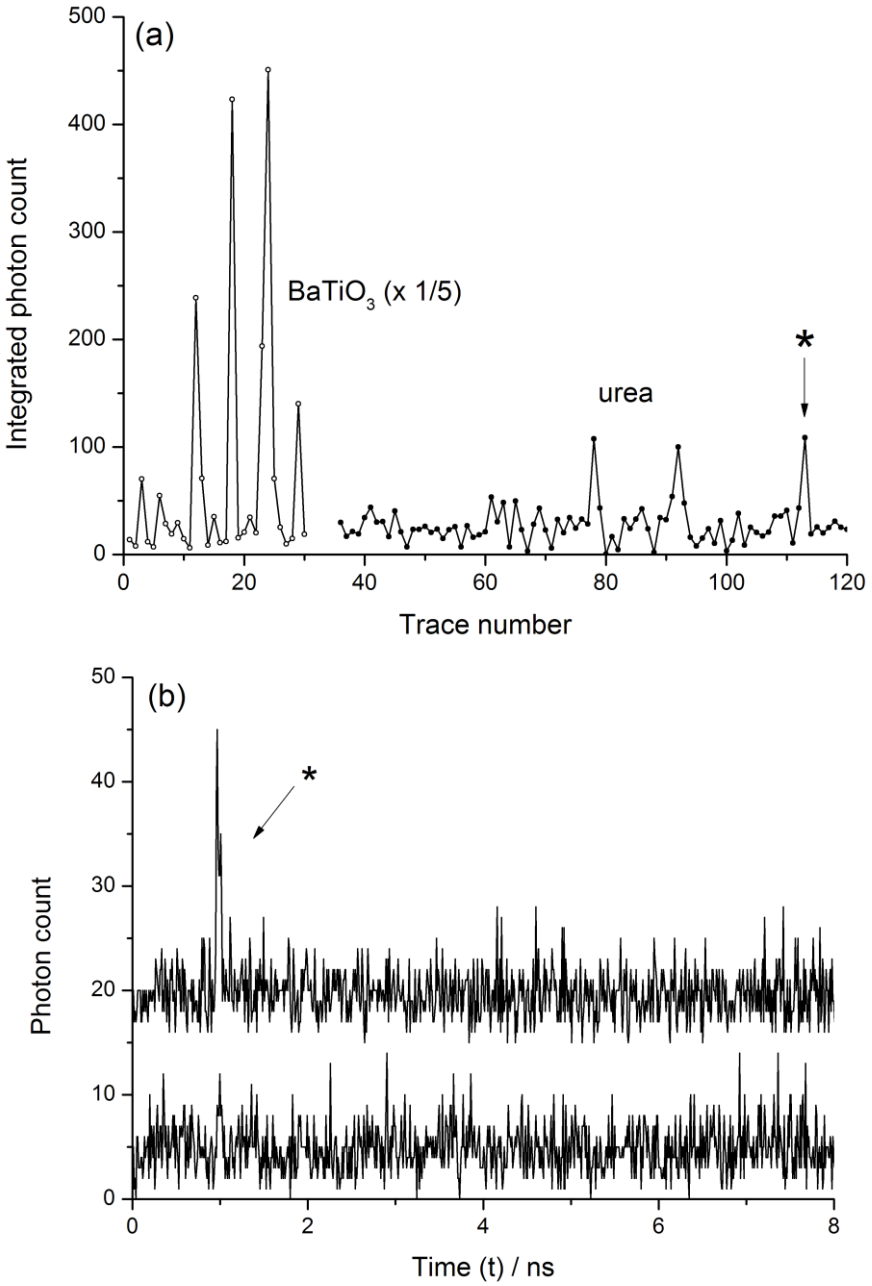

Figure 5.8 (a) Integrated photon counts from a series of consecutive traces taken while scanning through the solutions; these are total counts obtained by integrating under the peak for each trace, as described in Figure 5.5. The integration time for each time was 10 s. The first set of 30 points (open circles) were obtained using a dispersion of $BaTiO_3$ nanoparticles with diameters $d < 200$ nm; laser power $P = 3.8$ mW. The integrated photon counts recorded for $BaTiO_3$ have been multiplied by a factor of 1/5 to plot on the same scale. The second set of points (closed circles) from 36-120 were taken using urea solutions ($S = 0.98$); laser power $P = 3.4$ mW. In (b) individual traces are shown, numbers 113 (marked with an asterisk *) and 114; the top trace has been offset (by 15 counts) to aid comparison.

5.4 Discussion

5.4.1 Solute clustering

The results presented in Section 5.3 indicate that the source of SHS in the aqueous urea system is the native population of free clusters present in solution. Direct evidence of prenucleation clusters in solution is limited, however,both classical and two-step nucleation schemes predict their existence. Studies of NPLIN have shown that samples higher in solute concentration are more labile to nucleation (see Section 2.3 and ref. 55 & 93). It is thought that in more-concentrated solutions, the competition between solute–solute and solute–solvent interactions leads to formation of larger, more labile solute clusters. Considering the concentration of urea solutions used in this work it is seen that even at saturation (S = 1.0), the mole fraction of urea is x = 0.33; at the highest supersaturation of S = 1.86, x = 0.61, i.e., approximately 60% of the molecules present are urea. At such high levels of solute concentration, clustering is expected to be common; however, the likely resulting cluster size distribution remains uncertain, i.e., whether a sample is likely to produce few large clusters or many small clusters.

5.4.2 Mechanism for SHS and particle structure

Although the results presented here indicate that the identified particles in solution are responsible for the SHS, the data do not allow the precise nature of the particles to be deduced. If urea clusters have a crystalline structure, then the dominant mechanism for SHS would be bulk SHG. The bulk SHG efficiency (η) of urea relative to quartz (η = 400) is similar to that for $BaTiO_3$ (η = 130)[141]. However, the experiments show that samples of $BaTiO_3$ nanoparticles (d < 220 nm) provide signals which are a factor of 60 times greater than urea samples. If the urea clusters are crystalline in structure, then this factor may indicate that they are smaller than the $BaTiO_3$ particles. For bulk SHG, considering the dependence of SHG conversion efficiency on the interaction length (L), and taking in to account the cross-sectional area of the particles illuminated (σ), the following relationship is obtained; $\eta_{2\omega}^{(\mathrm{SHG})} \propto L^2\sigma$. [153] For a particle of diameter d the relationship becomes, $\eta_{2\omega}^{(\mathrm{SHG})} \sim d^4$, and we

estimate that particles of urea would be ~ 2.8 times smaller than the equivalent $BaTiO_3$ particles. This is a very crude estimate, however.

Because the expected cluster sizes (d ~100 nm) in urea solution are smaller than the wavelength of light, the mechanism for second harmonic generation is analogous to HRS, in contrast to a bulk SHG process. The incident electric field induces dipoles and (multi-poles) in and on the surface of the particle. The contributions from the induced dipoles combine coherently to produce the resulting SHG.[154]

It is not possible to distinguish between bulk and surface SHG processes from the experimental data collected in this work. Both processes result in emission of light with similar characteristics. If the particles are assumed to be native clusters of urea then two possible mechanisms for frequency doubling are possible; bulk and surface SHG.

Bulk SHG

Bulk SHG for nanoparticles has been shown to be highly efficient for crystalline materials that form non-centrosymmetric structures.[141,155] The peak signals obtained for urea samples in this work are only 1–2 orders of magnitude lower than for $BaTiO_3$ nanoparticles. As discussed earlier in Section 5.4.2 this difference may be due to urea clusters with non-centrosymmetric ordering that are smaller than the $BaTiO_3$ particles (d < 200 nm). However, it is important to highlight that complete crystal ordering is not required for bulk SHG. A mostly disordered collection of urea molecules with discrete regions of non-centrosymmetric ordering would be sufficient to allow SHG.[154] In this scenario, the SHG intensity would be lower than for a fully crystalline particle of identical size. Electronic structure calculations for small urea clusters (up to the 7-mer) have shown a near-linear increase of hyperpolarizability with monomer number.[156] The study also showed that intermolecular interactions, such as hydrogen-bonding for the urea system, significantly affect the hyperpolarizabilities, increasing the non-linear optical response. The concentration relationship of SHS intensity shown in Figure 5.5 may originate from changes in the internal structures or number densities of semi-ordered solute clusters.

Surface SHG

Another possibility to consider is that the urea clusters may have centrosymmetric ordering, that is to say are completely disordered. In this situation, symmetry arguments reduce the second order susceptibility tensor $\chi^{(2)}$ to zero, therefore bulk SHG is not possible. However, SHG is still possible due to the absence of inversion symmetry at the surface of the particle, though for a spherical cluster, the integrated surface contribution vanishes. For surface SHG to account for the measurements made during this study, this would imply that the clusters in question are non-spherical. In the case of the aqueous glycine system it is believed that the objects identified in concentrated solution are liquid-like in structure and aspherical in shape.[24,23] Another possibility is that the clusters are spherical in shape, however a layer of solute molecules at the surface, with some degree of orientational order, allows for SHG to occur.[157]

5.4.3 Possible role of impurity particles

Due to the nature of the data collected here, the possibility of solid impurities in the sample causing the observed SHG signal cannot be ruled out. Solid impurity particles could exhibit SHG following either bulk or surface SHG mechanisms, analogous to the case outlined for urea clusters in the previous section. It is possible that the impurity particles are solid, crystalline particles which are SHG active. Alternatively, the impurity particle may act as a substrate upon which solute molecules are absorbed. It is then plausible that the adsorbed layer would assume some sort of orientational order, to facilitate second harmonic emission, even from a centrosymmetric impurity particle.[157] Due to the sample concentrations used in experiment, even at the lowest supersaturation of $S = 0.15$ it is expected that the surface of such impurity particles would be saturated with solute. During the course of experiments, several water samples were prepared using the same methods as the urea samples, and showed no scattering particles in solution. The most probable source of impurities is then from the solid solute (see also discussion on filtering, Section 4.3.8). If the solute was the source of particles observed during experiment,

then a linear relationship between SHS signal and sample concentration (or supersaturation) would be expected, contrary to the results obtained (Figure 5.5).

5.4.4 Concentration dependence

It is clear that for both considerations, urea clusters or impurities, the details of the distributions (size and number) of objects in solution would influence the intensity of SHS signal measured in experiment. For solid impurities, the distribution of particle size in sample solutions would not be expected to vary significantly with solute concentration. On the contrary, distributions describing the population of solute clusters in solution are expected to be intimately dependent on solute concentration.

At the present time, it is not obvious why the data presented in Figure 5.5 show local minima around the point of $S = 1.0$ and $S = 1.7$. One explanation is that the changes in signal represent significant changes in the structure of the sample solutions. At the point of saturation ($S = 1.0$) a large number of small clusters might be expected. Although small in size, these clusters would be encountered frequently during the scanning process, resulting in a higher measured SHS signal. As the supersaturation is increased, larger clusters would form which would be encountered less frequently during scanning. Measurements of diffusion in concentrated systems, including the aqueous urea system,[118,158] have identified a sharp drop of the diffusion coefficient above the point of saturation with the behaviour attributed to formation of large solute aggregates in solution.[47,117] In other words, the features at $S = 1.0$ and 1.7 may indicate the emergence of a distinct metastable thermodynamic phase that occurs due to the increasing proportion of solute in the system.

Further work is required to support the preliminary results presented here. This could include combining SHS with Rayleigh scattering measurements to demonstrate directly that the SHS signal originates from long-lived particles in solution. A more challenging approach would be to investigate the nature of the SHS signal. An angle-resolved measurement would allow separation of the coherent SHG signal from the incoherent HRS emission,[159] which may provide more information about the structure of the scattering objects.

5.5 Conclusions

In conclusion, measurements of second-harmonic scattering (SHS) from aqueous solutions of urea have been performed using scanning microscopy. The SHS signal was recorded as a function of concentration ranging from $S = 0.15$ (undersaturated) to $S = 1.86$ (supersaturated). The results show a general trend of increasing signal with concentration; however, the data show local maxima around the points of $S = 0.95$ and 1.75, suggesting a significant change in the solution structure at these points. Rayleigh scattering measurements identify a population of long-lived particles in solution. Time-dependent SHS measurements show a series of discrete peaks obtained whilst scanning through the sample solution. Comparative results achieved when using aqueous dispersions of $BaTiO_3$ nanoparticles (SHG active) confirm that the urea results are consistent with SHG from individual particles. The results suggest that urea solution contains a population of semi-ordered solute clusters, the internal structures, number densities and sizes of which are dependent on concentration.

Chapter 6: Final conclusions

The desire to control crystallization processes has been the driving force behind much research in the field of crystallization for many years. Without a detailed knowledge of the step of crystal nucleation, new methods of crystallization are often a consequence of trial and error. The discovery of NPLIN has since provided a technique that allows nucleation to be confined spatially (~10^{-1} mL) and temporally (~10^{-9} s). As discussed in Chapter 2, NPLIN of KCl and KBr have been demonstrated. The results of this work led to improvement of the IP model of NPLIN. To date this model has only been applied to crystal systems which cannot undergo the OKE mechanism due to symmetry considerations. It would be interesting to see how the IP model performs when applied to the other systems previously reported to undergo NPLIN by the OKE mechanism e.g., glycine and urea. It is also apparent that in order for advances to be made in the field, a greater theoretical understanding of the nucleation process is required. Another key outcome of this work is the generation of experimental data that may be used to help test and improve current models of NPLIN as well as stimulate much needed theoretical studies in the future.

Due to the typical volume of solution probed during NPLIN, the outcome of the experiment is only observation of whether nucleation has occurred or not. In order to experimentally probe nucleation directly and *in situ* it will be required to significantly increase spatial control of the nucleation event. Current techniques involve tightly focussing the laser beam which typically leads to undesirable photochemical and photomechanical effects. In this Thesis, as detailed in Chapter 3, nucleation was successfully induced by use of an evanescent wave generated by total internal reflection (ew-NPLIN). This novel technique confines nucleation to a volume ~5 orders of magnitude less than that of a typical NPLIN experiment. Aside to providing a technique more compatible with direct and *in situ* studies of the nucleation event the very nature of the technique would allow incorporation of optical analytical techniques such as TIR-Raman or SERS. The results of such work may help to unravel the details behind the mechanism of NPLIN and nucleation in general.

As evidence in support of the two-step model of nucleation increases, it is key that experimental work is aimed towards investigation of the structure of concentrated, pre-nucleated solutions. In the work outlined in Chapter 4 a range of sample solutions prepared to have supersaturation $S = 0.95$ were tested using Rayleigh laser scattering. In almost all solutions populations of long-lived scattering particles were identified. This technique only allows the observation of particles in solution; it does not allow information of the particle structure or composition to be obtained. Nanoparticle tracking analysis was used to estimate the size distribution of particles in concentrated solution. The scattering strength of such particles was compared to the scattering seen for polystyrene beads of known size. The results suggest a small difference in refractive index between the particles and surrounding solution in concentrated solutions. Furthermore analysis of the scattering observed from particles in concentrated solutions provides evidence that the scattering objects are not necessarily spherical. These observations contrast with the behaviour expected if solid impurities or nanobubbles were the origin of the scattering particles identified by laser scattering.

The work outlined in Chapter 4 does not allow impurities or the presence of nanobubbles to be completely ruled out as the origin of scattering objects in solution. Therefore, it is important that future work aims to verify the hypothesis that the particles observed in this work is evidence of pre-nucleated clusters in solution. Furthermore, regardless of the precise nature of the particles observed in experiment (solute clusters or something else), it is important that the possible role of the particles in the mechanism of NPLIN and nucleation in general is investigated. A key experiment to consider is a combined laser scattering/NPLIN investigation in which the scattering objects and their interaction with a probe (nucleating) laser pulse could be directly viewed. This would allow identification of nuclei formed by direct interaction with a particle seen by Rayleigh scattering.

It is likely that the mechanism of nucleation of solute clusters is dictated by the internal structure, or lack thereof, of the cluster. A highly sensitive technique that has been used to monitor the nucleation and growth of second harmonic active materials is second harmonic scattering (SHS). Following from the results of laser

scattering work (Chapter 4), the aqueous urea system, for which the solid is a second-harmonic active material, was identified for further investigation using SHS.

As shown in Chapter 5, the second harmonic response was measured as a function of solute supersaturation ($S = 0.15–1.86$). The results show a nonlinear increase in SHS signal with supersaturation with local maxima near $S = 0.95$ and 1.75 suggesting a change in solution structure near these points. The measured intensity was shown to exceed the expected contribution of hyper-Rayleigh scattering from solution for all data points. Comparison with a dispersion of characterised second-harmonic active particles showed that the measured signal in urea solution is consistent with SHS from individual particles encountered during scanning. As the very nature of the particles found in solution remains unknown, it is not clear the precise process that causes SHS in urea solution. The data collected in this work is not sufficient to assign whether the measured SHS results from solute clusters or an unknown impurity.

However, assuming that any impurities come from the urea, a measured signal increasing linearly with solute concentration would be expected if impurity particles were responsible, in contrast to the experimental observations. The results suggest that a population of semi-ordered clusters exist in aqueous urea solution, and that the structures and number densities of these clusters change with concentration. Further work is required to support these initial findings and it is expected that different types of ordering of solute clusters would give rise to different scattering signatures. It is thought that angle resolved measurement of SHS could be used to distinguish between, for example, coherent SHG and incoherent HRS, and thereby to determine more details of the structure of the scattering particles.

Due to the challenging nature of direct experimental investigation of the nucleation event it is becoming evident that computational simulation and theoretical studies may be the most effective way of making advances in this area. Not only could such theoretical studies help to guide future experimental work, but it may also allow the formulation of new models of nucleation which can then be tested with existing experimental data; such as that contained within this Thesis. This point has particular relevance when considering revision of current models, which are typically

based on CNT, to operate purely in the framework of the 2SM for which there is not yet a formal theoretical description.

In spite of a lack of a full understanding of the mechanism of NPLIN, the technique can still be employed as a reliable method of nuclei generation in solution. Once the required parameters of solution conditions and of the incident laser source for NPLIN have been established the formation of a known mean number of nuclei per laser pulse is possible. This has applications in research as a way to study crystal growth where NPLIN could be used to produce a single crystal at a known location, or as a way to introduce a known number of nuclei within a certain volume to seed a solution in a closed system; e.g., sterile seeding of a continuous crystallization process.

References

1 Kind, M. & Mersmann, A. On supersaturation during mass crystallization from solution. *Chemical Engineering & Technology* **13**, 50-62, doi:10.1002/ceat.270130108 (1990).

2 Mullin, J. W. *Crystallization*, 4th ed.; Butterworth-Heinemann: Oxford (2001).

3 Alexander, A. J. & Ward, M. R. unpublished work. *unpublished work* (2013).

4 Miers, H. A. & Isaac, F. XLVII.-The refractive indices of crystallising solutions, with especial reference to the passage from the metastable to the labile condition. *Journal of the Chemical Society, Transactions* **89**, 413-454, doi:10.1039/ct9068900413 (1906).

5 Erdemir, D., Lee, A. Y. & Myerson, A. S. Nucleation of Crystals from Solution: Classical and Two-Step Models. *Accounts of Chemical Research* **42**, 621-629, doi:10.1021/ar800217x (2009).

6 Kashchiev, D. *Nucleation*, 1st ed.; Butterworth-Heinemann: Oxford (2000).

7 Sear, R. P. The non-classical nucleation of crystals: microscopic mechanisms and applications to molecular crystals, ice and calcium carbonate. *International Materials Reviews* **57**, 328-356, doi:10.1179/1743280411Y (2012).

8 Vekilov, P. G. The two-step mechanism of nucleation of crystals in solution. *Nanoscale* **2**, 2346-2357, doi:10.1039/c0nr00628a (2010).

9 Vekilov, P. G. Two-step mechanism for the nucleation of crystals from solution. *Journal of Crystal Growth* **275**, 65-76 (2005).

10 Wolde, P. R. t. & Frenkel, D. Enhancement of Protein Crystal Nucleation by Critical Density Fluctuations. *Science* **277**, 1975-1978, doi:10.1126/science.277.5334.1975 (1997).

11 Gibbs, J. W. *The collected works of J. Willard Gibbs : Vol I*. 2 edn, (Yale University Press, 1948).

12 Volmer, M. *Kinetics of Phase Formation: (Kinetik Der Phasenbildung)*. (Air Force Cambridge Reasarch Center, Geophysics Research Division, Atmospheric Physics Laboratory, 1939).

13 Becker, R. & Döring, W. Kinetische Behandlung der Keimbildung in übersättigten Dämpfen. *Annalen der Physik* **416**, 719-752, doi:10.1002/andp.19354160806 (1935).

14 Kathmann, S. M., Sellner, B., Alexander, A. J. & Valiev, M. Beyond classical theories. *AIP Conference Proceedings* **1527**, 109-112, doi:10.1063/1.4803215 (2013).

15 Hickey, J. & L'Heureux, I. Classical nucleation theory with a radius-dependent surface tension: A two-dimensional lattice-gas automata model. *Physical Review E* **87**, 022406 (2013).

16 Merikanto, J., Zapadinsky, E., Lauri, A. & Vehkamäki, H. Origin of the Failure of Classical Nucleation Theory: Incorrect Description of the Smallest Clusters. *Physical Review Letters* **98**, 145702 (2007).

17 Merikanto, J., Lauri, A., Zapadinsky, E. & Vehkamäki, H. in *Nucleation and Atmospheric Aerosols* (eds ColinD O'Dowd & PaulE Wagner) Ch. 24, 121-125 (Springer Netherlands, 2007).
18 Gránásy, L. & Iglói, F. Comparison of experiments and modern theories of crystal nucleation. *The Journal of Chemical Physics* **107**, 3634-3644, doi:10.1063/1.474721 (1997).
19 Horsch, M., Vrabec, J. & Hasse, H. Modification of the classical nucleation theory based on molecular simulation data for the surface tension, critical nucleus size, and nucleation rate. *Physical Review E* **78**, 011603 (2008).
20 Jayaraaman, D., Subramanian, C. & Ramasamy, P. Effect of curvature-dependent surface tension on nucleation. *J Mater Sci Lett* **8**, 1399-1404 (1989).
21 Dhanasekaran, R. & Ramasamy, P. On the dependence of interfacial tension on the size of two-dimensional nucleation. *Indian journal of physics A* **59**, 408-416 (1985).
22 Oxtoby, D. W. Nucleation of First-Order Phase Transitions. *Accounts of Chemical Research* **31**, 91-97, doi:10.1021/ar9702278 (1998).
23 Jawor-Baczynska, A., Moore, B. D., Lee, H. S., McCormick, A. V. & Sefcik, J. Population and size distribution of solute-rich mesospecies within mesostructured aqueous amino acid solutions. *Faraday Discussions*, doi:10.1039/c3fd00066d (2013).
24 Jawor-Baczynska, A., Sefcik, J. & Moore, B. D. 250 nm Glycine-Rich Nanodroplets Are Formed on Dissolution of Glycine Crystals But Are Too Small To Provide Productive Nucleation Sites. *Crystal Growth & Design* **13**, 470-478, doi:10.1021/cg300150u (2012).
25 Tolman, R. C. The Effect of Droplet Size on Surface Tension. *The Journal of Chemical Physics* **17**, 333-337, doi:10.1063/1.1747247 (1949).
26 Kumar, F. J., Jayaraman, D., Subramanian, C. & Ramasamy, P. Curvature dependence of surface free energy and nucleation kinetics of CCl4 and C2H2Cl4 vapours. *J Mater Sci Lett* **10**, 608-610, doi:10.1007/bf00724454 (1991).
27 Katz, J. L., Mirabel, P., Scoppa II, C. J. & Virkler, T. L. Condensation of a supersaturated vapor. III. The homogeneous nucleation of CCl4, CHCl3, CCl3F, and C2H2Cl4. *The Journal of Chemical Physics* **65**, 382-392, doi:10.1063/1.432778 (1976).
28 Napari, I., Julin, J. & Vehkamäki, H. Performance of some nucleation theories with a nonsharp droplet-vapor interface. *Journal of Chemical Physics* **133**, 154503, doi:10.1063/1.3502643 (2010).
29 Vekilov, P. G. Dense Liquid Precursor for the Nucleation of Ordered Solid Phases from Solution. *Crystal Growth & Design* **4**, 671-685, doi:10.1021/cg049977w (2004).
30 Nicolis, G. & Nicolis, C. Enhancement of the nucleation of protein crystals by the presence of an intermediate phase: a kinetic model. *Physica A: Statistical Mechanics and its Applications* **323**, 139-154, doi:10.1016/S0378-4371(03)00060-8 (2003).
31 Bonnett, P. E., Carpenter, K. J., Dawson, S. & Davey, R. J. Solution crystallisation via a submerged liquid-liquid phase boundary: oiling out. *Chemical Communications*, 698-699, doi:10.1039/b212062c (2003).

32 Shore, J. D., Perchak, D. & Shnidman, Y. Simulations of the nucleation of AgBr from solution. *Journal of Chemical Physics* **113**, 6276, doi:10.1063/1.1308517 (2000).
33 Ginde, R. M. & Myerson, A. S. Cluster size estimation in binary supersaturated solutions. *Journal of Crystal Growth* **116**, 41-47, doi:10.1016/0022-0248(92)90112-V (1992).
34 Myerson, A. S. & Lo, P. Y. Cluster formation and diffusion in supersaturated binary and ternary amino acid solutions. *Journal of Crystal Growth* **110**, 26-33, doi:10.1016/0022-0248(91)90862-Y (1991).
35 Myerson, A. S. & Lo, P. Y. Diffusion and cluster formation in supersaturated solutions. *Journal of Crystal Growth* **99**, 1048-1052, doi:10.1016/S0022-0248(08)80079-6 (1990).
36 Larson, M. A. & Garside, J. Solute clustering in supersaturated solutions. *Chemical Engineering Science* **41**, 1285-1289, doi:10.1016/0009-2509(86)87101-9 (1986).
37 Larson, M. A. & Garside, J. Solute clustering and interfacial tension. *Journal of Crystal Growth* **76**, 88-92, doi:10.1016/0022-0248(86)90013-8 (1986).
38 Prouty, M. S., Schechter, A. N. & Parsegian, V. A. Chemical potential measurements of deoxyhemoglobin S polymerization: Determination of the phase diagram of an assembling protein. *Journal of Molecular Biology* **184**, 517-528, doi:10.1016/0022-2836(85)90298-0 (1985).
39 Zhang, T. H. & Liu, X. Y. How Does a Transient Amorphous Precursor Template Crystallization. *Journal of the American Chemical Society* **129**, 13520-13526, doi:10.1021/ja073598k (2007).
40 Stradner, A. *et al.* Equilibrium cluster formation in concentrated protein solutions and colloids. *Nature* **432**, 492-495 (2004).
41 Savage, J. R. & Dinsmore, A. D. Experimental Evidence for Two-Step Nucleation in Colloidal Crystallization. *Physical Review Letters* **102**, 198302 (2009).
42 Gránásy, L. & Toth, G. I. Crystallization: Colloidal suspense. *Nat Phys* **10**, 12-13, doi:10.1038/nphys2849 (2014).
43 Kashchiev, D., Vekilov, P. G. & Kolomeisky, A. B. Kinetics of two-step nucleation of crystals. *The Journal of Chemical Physics* **122**, doi:10.1063/1.1943389 (2005).
44 Lutsko, J. F. & Nicolis, G. Theoretical Evidence for a Dense Fluid Precursor to Crystallization. *Physical Review Letters* **96**, 046102 (2006).
45 Li, Y., Lubchenko, V., Vorontsova, M. A., Filobelo, L. & Vekilov, P. G. Ostwald-Like Ripening of the Anomalous Mesoscopic Clusters in Protein Solutions. *The Journal of Physical Chemistry B* **116**, 10657-10664, doi:10.1021/jp303316s (2012).
46 Hagmeyer, D. *et al.* Direct experimental observation of the aggregation of a-amino acids into 100-200 nm clusters in aqueous solution. *RSC Advances* **2**, 4690-4696, doi:10.1039/c2ra01352e (2012).
47 Kim, Y.-C. b. & Myerson, A. Diffusivity of protein in aqueous solutions. *Korean J. Chem. Eng.* **13**, 288-293, doi:10.1007/bf02705952 (1996).
48 Georgalis, Y., Kierzek, A. M. & Saenger, W. Cluster Formation in Aqueous Electrolyte Solutions Observed by Dynamic Light Scattering. *The Journal of Physical Chemistry B* **104**, 3405-3406, doi:10.1021/jp000132e (2000).

49 Li, L. & Ogawa, T. Clusters and their properties in aqueous solutions of KDP, KCl and sugar. *Journal of Crystal Growth* **211**, 286-289, doi:10.1016/S0022-0248(99)00862-3 (2000).
50 Lian, L., Taijing, L., Zaizu, Y. & Ogawa, T. Size distribution of ultrafine particles in KDP aqueous solutions. *Journal of Materials Research* **11**, 387-390, doi:10.1557/JMR.1996.0047 (1996).
51 Lian, L., Taijing, L., Sakai, K. & Ogawa, T. *In situ* observation of subcritical crystalline particles and their behavior on growth of KDP crystals from aqueous solution by light-scattering technique. *Journal of Materials Research* **7**, 3275-3279, doi:10.1557/JMR.1992.3275 (1992).
52 Garetz, B. A., Aber, J. E., Goddard, N. L., Young, R. G. & Myerson, A. S. Nonphotochemical, polarization-dependent, laser-induced nucleation in supersaturated aqueous urea solutions. *Physical Review letters* **77**, 3475-3476 (1996).
53 Ward, M. R., Ballingall, I., Costen, M. L., McKendrick, K. G. & Alexander, A. J. Nanosecond pulse width dependence of nonphotochemical laser-induced nucleation of potassium chloride. *Chemical Physics Letters* **481**, 25-28 (2009).
54 Duffus, C., Camp, P. J. & Alexander, A. J. Spatial Control of Crystal Nucleation in Agarose Gel. *Journal of the American Chemical Society* **131**, 11676-11677 (2009).
55 Alexander, A. J. & Camp, P. J. Single Pulse, Single Crystal Laser-Induced Nucleation of Potassium Chloride. *Crystal Growth & Design* **9**, 958-963 (2009).
56 Lee, I. S., Evans, J. M. B., Erdemir, D., Lee, A. Y. & Garetz, B. A. Nonphotochemical Laser Induced Nucleation of Hen Egg White Lysozyme Crystals. *Crystal Growth & Design* **8**, 4255-4261 (2008).
57 Matic, J., Sun, X. & Garetz, B. A. Intensity, Wavelength and Polarization Dependence of Nonphotochemical Laser-Induced Nucleation in Supersaturated Aqueous Urea Solutions. *Crystal Growth & Design* **5**, 1565-1567 (2005).
58 Sun, X., Garetz, B. A. & Myerson, A. S. Polarization Switching of Crystal Structure in the Nonphotochemical Laser-Induced Nucleation of Supersaturated Aqueous L-Histidine. *Crystal Growth & Design* **8**, 1720-1722 (2008).
59 Garetz, B. A., Matic, J. & Myerson, A. S. Polarization Switching of Crystal Structure in the Nonphotochemical Light-Induced Nucleation of Supersaturated Aqueous Glycine Solutions. *Physical Review letters* **89**, 175501 (2002).
60 Sun, X. & Garetz, B. A. Supersaturation and polarization Dependence of Polymorph Control in the Nonphotochemical Laser-Induced Nucleation (NPLIN) of Aqueous Glycine Solutions. *Crystal Growth & Design* **6**, 684-689 (2006).
61 Zaccaro, J., Matic, J., Myerson, A. S. & Garetz, B. A. Nonphotochemical, Laser-Induced nucleation of Supersaturated aqueous Glycine Produces Unexpected γ-Polymorph. *Crystal Growth & Design* **1**, 5-8 (2001).

62 Boldyreva, E. *et al.* Polymorphism of glycine, Part I. *Journal of Thermal Analysis and Calorimetry* **73**, 409-418, doi:10.1023/a:1025405508035 (2003).
63 Srinivasan, K. Crystal growth of α and γ glycine polymorphs and their polymorphic phase transformations. *Journal of Crystal Growth* **311**, 156-162, doi:10.1016/j.jcrysgro.2008.10.084 (2008).
64 Perlovich, G. L., Hansen, L. K. & Bauer-Brandl, A. The Polymorphism of Glycine. Thermochemical and structural aspects. *Journal of Thermal Analysis and Calorimetry* **66**, 699-715, doi:10.1023/a:1013179702730 (2001).
65 Yuyama, K.-i., Rungsimanon, T., Sugiyama, T. & Masuhara, H. Selective Fabrication of α- and γ-Polymorphs of Glycine by Intense Polarized Continuous Wave Laser Beams. *Crystal Growth & Design* **12**, 2427-2434, doi:10.1021/cg300065x (2012).
66 Rungsimanon, T. *et al.* Control of Crystal Polymorph of Glycine by Photon Pressure of a Focused Continuous Wave Near-Infrared Laser Beam. *The Journal of Physical Chemistry Letters* **1**, 599-603, doi:10.1021/jz900370x (2010).
67 Chattopadhyay, S. *et al.* SAXS Study of the Nucleation of Glycine Crystals from a Supersaturated Solution. *Crystal Growth & Design* **5**, 523-527, doi:10.1021/cg0497344 (2005).
68 Huang, J., Stringfellow, T. C. & Yu, L. Glycine Exists Mainly as Monomers, Not Dimers, in Supersaturated Aqueous Solutions: Implications for Understanding Its Crystallization and Polymorphism. *Journal of the American Chemical Society* **130**, 13973-13980 (2008).
69 Hamad, S., Hughes, C. E., Catlow, C. R. A. & Harris, K. D. M. Clustering of Glycine Molecules in Aqueous Solution Studied by Molecular Dynamics Simulation. *The Journal of Physical Chemistry B* **112**, 7280-7288, doi:10.1021/jp711271z (2008).
70 Burton, R. C. *et al.* The Structure of a Supersaturated Solution: A Neutron Scattering Study of Aqueous Urea. *Crystal Growth & Design* **8**, 1559-1565, doi:10.1021/cg700829r (2008).
71 Matsuoka, H., Schwahn, D. & Ise, N. Observation of cluster formation in polyelectrolyte solutions by small-angle neutron scattering. 1. A steep upturn of the scattering curves from solutions of sodium poly(styrenesulfonate) at scattering vectors below 0.01 .ANG.-1. *Macromolecules* **24**, 4227-4228, doi:10.1021/ma00014a047 (1991).
72 Sorensen, T. J., Sontum, P. C., Samseth, J., Thorsen, G. & Malthe-Sorenssen, D. Cluster Formation in Precrystalline Solutions. *Chemical Engineering & Technology* **26**, 307-312, doi:10.1002/ceat.200390047 (2003).
73 Kellermeier, M. *et al.* Colloidal Stabilization of Calcium Carbonate Prenucleation Clusters with Silica. *Advanced Functional Materials* **22**, 4301-4311, doi:10.1002/adfm.201200953 (2012).
74 Fulton, J. L. & Pfund, D. M. Small angle X-ray scattering studies of aggregation in supercritical fluid solutions. Report No. PNL-SA--24552; CONF-9410114--4; Other: ON: DE95004576;; TRN: AHC29505%%9 United States10.2172/10107265Other: ON: DE95004576;; TRN: AHC29505%%9Fri Dec 11 07:33:15 EST 2009OSTI; NTIS; GPO

Dep.PNNL; SCA: 400201; PA: EDB-95:030256; SN: 95001300054English, Medium: ED; Size: 7 p. (1994).
75 Knott, B. C., Doherty, M. F. & Peters, B. A simulation test of the optical Kerr mechanism for laser-induced nucleation. *The Journal of Chemical Physics* **134**, 154501 (2011).
76 Nardone, M. & Karpov, V. G. Nucleation of metals by strong electric fields. *Applied Physics Letters* **100**, doi:10.1063/1.3703611 (2012).
77 Karpov, V. G. & Nardone, M. Comment on "Threshold switching via electric field induced crystallization in phase change memory devices" [Appl. Phys. Lett. 100, 253105 (2012)]. *Applied Physics Letters* **102**, doi:10.1063/1.4809720 (2013).
78 Nardone, M. & Karpov, V. G. A phenomenological theory of nonphotochemical laser induced nucleation. *Physical Chemistry Chemical Physics* **14**, 13601-13611, doi:10.1039/c2cp41880k (2012).
79 Knott, B. C., LaRue, J. L., Wodtke, A. M., Doherty, M. F. & Peters, B. Communication: Bubbles, crystals, and laser-induced nucleation. *The Journal of Chemical Physics* **134**, 171102-171104 (2011).
80 Vogel, A., Noack, J., Hüttman, G. & Paltauf, G. Mechanisms of femtosecond laser nanosurgery of cells and tissues. *Appl. Phys. B* **81**, 1015-1047, doi:10.1007/s00340-005-2036-6 (2005).
81 Aber, J. E., Arnold, S. & Garetz, B. A. Strong dc electric field applied to supersaturated aqueous glycine solution induces nucleation of the γ polymorph. *Physical Review Letters* **94**, 145503 (2005).
82 Sun, X., Garetz, B. A., Moreira, M. F. & Palffy-Muhoray, P. Nonphotochemical laser-induced nucleation of nematic phase and alignment of nematic director from a supercooled thermotropic liquid crystal. *Physical Review E* **79**, 021701 (2009).
83 Isard, J. O. Calculation of the influence of an electric field on the free energy of formation of a nucleus. *Philosophical Magazine* **35**, 817-819, doi:10.1080/14786437708236010 (1977).
84 Ward, M. R., McHugh, S. & Alexander, A. J. Non-photochemical laser-induced nucleation of supercooled glacial acetic acid. *Physical Chemistry Chemical Physics* **14**, 90-93 (2012).
85 Brown, L. D., Cai, T. T. & DasGupta, A. Interval Estimation for a Binomial Proportion. 101-133, doi:10.1214/ss/1009213286 (2001).
86 Digilov, R. M. Semi-empirical model for prediction of crystal–melt interfacial tension. *Surface Science* **555**, 68-74, doi:10.1016/j.susc.2004.02.024 (2004).
87 Gavezzotti, A. A molecular dynamics view of some kinetic and structural aspects of melting in the acetic acid crystal. *Journal of Molecular Structure* **485–486**, 485-499, doi:10.1016/S0022-2860(99)00056-3 (1999).
88 Ward, M. R., Copeland, G. W. & Alexander, A. J. Enantiomorphic symmetry breaking in crystallization of molten sodium chlorate. *Chemical Communications* **46**, 7634-7636, doi:10.1039/c0cc02563a (2010).
89 Ward, M. R., Copeland, G. W. & Alexander, A. J. Chiral hide-and-seek: Retention of enantiomorphism in laser-induced nucleation of molten sodium chlorate. *Journal of Chemical Physics* **135**, 114508-114508-114508, doi:10.1063/1.3637946 (2011).

90 Begg, I. D. *et al.* X-Ray Topographic Investigations of Solid State Reactions. I. Changes in Surface and Bulk Substructure During Incipient Thermal Decomposition in Sodium Chlorate Monocrystals. *Proceedings of the Royal Society of London. A. Mathematical and Physical Sciences* **386**, 431-442, doi:10.1098/rspa.1983.0044 (1983).
91 Volmer, M. Particle formation and particle action as a special case of heterogeneous catalysis. *Zeitschrift für Elektrochemie und angewandte physikalische Chemie* **35**, 555-561 (1929).
92 Turnbull, D. Kinetics of Heterogeneous Nucleation. *The Journal of Chemical Physics* **18**, 198-203, doi:10.1063/1.1747588 (1950).
93 Ward, M. R. & Alexander, A. J. Nonphotochemical Laser-Induced Nucleation of Potassium Halides: Effects of Wavelength and Temperature. *Crystal Growth & Design* **12**, 4554-4561, doi:10.1021/cg300750c (2012).
94 Haynes, W. M. *CRC handbook of chemistry and physics*. (Boca Raton, Fla. : CRC ; London : Taylor & Francis [distributor], 2012.
93rd edition, 2012-2013 / editor-in-chief, W.M. Haynes., 2012).
95 Vosel, S. V., Onischuk, A. A., Purtov, P. A. & Tolstikova, T. G. in *Aerosols Handbook* 503-528 (CRC Press, 2012).
96 Baidakov, V. G. & Tipeev, A. O. Crystal nucleation and the solid-liquid interfacial free energy. *Journal of Chemical Physics* **136**, 074510, doi:10.1063/1.3678214 (2012).
97 Tolman, R. C. The effect of droplet size on surface tension. *Journal of Chemical Physics* **17**, 333 (1949).
98 Mersmann, A. Calculation of interfacial tensions. *Journal of Crystal Growth* **102**, 841-847, doi:10.1016/0022-0248(90)90850-K (1990).
99 Nielsen, A. E. & Söhnel, O. Interfacial tensions electrolyte crystal-aqueous solution, from nucleation data. *Journal of Crystal Growth* **11**, 233-242, doi:10.1016/0022-0248(71)90090-X (1971).
100 Cohen, M. D., Flagan, R. C. & Seinfeld, J. H. Studies of concentrated electrolyte solutions using the electrodynamic balance. 3. Solute nucleation. *The Journal of Physical Chemistry* **91**, 4583-4590, doi:10.1021/j100301a031 (1987).
101 Chatterji, A. C. & Singh, R. N. Nucleation from Quiet Supersaturated Solution of Alkali Halides. Part I. Chlorides, Bromides, Iodides of Potassium and Ammonium. *The Journal of Physical Chemistry* **62**, 1408-1411, doi:10.1021/j150569a014 (1958).
102 Kashchiev, D. & van Rosmalen, G. M. Review: Nucleation in solutions revisited. *Crystal Research and Technology* **38**, 555-574, doi:10.1002/crat.200310070 (2003).
103 Savage, J. R. & Dinsmore, A. D. Experimental Evidence for Two-Step Nucleation in Colloidal Crystallization. *Physical Review Letters* **102**, 198302 (2009).
104 Abelson, J. R. *et al.* Observation of the Role of Subcritical Nuclei in Crystallization of a Glassy Solid. *Science* **326**, 980-984 (2009).
105 Chakraborty, D. & Patey, G. N. How Crystals Nucleate and Grow in Aqueous NaCl Solution. *The Journal of Physical Chemistry Letters* **4**, 573-578, doi:10.1021/jz302065w (2013).

106 Zahn, D. Atomistic Mechanism of NaCl Nucleation from an Aqueous Solution. *Physical Review Letters* **92**, 040801 (2004).
107 Chowdhuri, S. & Chandra, A. Molecular dynamics simulations of aqueous NaCl and KCl solutions: Effects of ion concentration on the single-particle, pair, and collective dynamical properties of ions and water molecules. *The Journal of Chemical Physics* **115**, 3732-3741, doi:10.1063/1.1387447 (2001).
108 Garten, V. A. & Head, R. B. Crystalloluminescence and the nature of the critical nucleus. *Philosophical Magazine* **8**, 1793-1803, doi:10.1080/14786436308209074 (1963).
109 Garten, V. A. & Head, R. B. Homogeneous nucleation and the phenomenon of crystalloluminescence. *Philosophical Magazine* **14**, 1243-1253, doi:10.1080/14786436608224289 (1966).
110 Lindinger, B., Mettin, R., Chow, R. & Lauterborn, W. Ice Crystallization Induced by Optical Breakdown. *Physical Review Letters* **99**, 045701 (2007).
111 Soare, A. *et al.* Crystal Nucleation by Laser-Induced Cavitation. *Crystal Growth & Design* **11**, 2311-2316, doi:10.1021/cg2000014 (2011).
112 Guasto, J., Huang, P. & Breuer, K. in *Encyclopedia of Microfluidics and Nanofluidics* (ed Dongqing Li) Ch. 513, 638-644 (Springer US, 2008).
113 Smith, F. G., King, T. A. & Wilkins, D. *Optics and Photonics: An Introduction*. (Wiley, 2007).
114 Rieger, B., Dietrich, H. R. C., Doel, L. R. V. D. & Vliet, L. J. V. Diffusion of microspheres in sealed and open microarrays. *Microscopy Research and Technique* **65**, 218-225, doi:10.1002/jemt.20128 (2004).
115 Buscall, R. & White, L. R. The consolidation of concentrated suspensions. Part 1.-The theory of sedimentation. *Journal of the Chemical Society, Faraday Transactions 1: Physical Chemistry in Condensed Phases* **83**, 873-891, doi:10.1039/f19878300873 (1987).
116 Sedlák, M. & Rak, D. Large-Scale Inhomogeneities in Solutions of Low Molar Mass Compounds and Mixtures of Liquids: Supramolecular Structures or Nanobubbles? *The Journal of Physical Chemistry B* **117**, 2495-2504, doi:10.1021/jp4002093 (2013).
117 Chang, Y. C. & Myerson, A. S. The diffusivity of potassium chloride and sodium chloride in concentrated, saturated, and supersaturated aqueous solutions. *AIChE Journal* **31**, 890-894, doi:10.1002/aic.690310603 (1985).
118 Sorell, L. S. & Myerson, A. S. Diffusivity of urea in concentrated, saturated and supersaturated solutions. *AIChE Journal* **28**, 772-779, doi:10.1002/aic.690280511 (1982).
119 Frost, R. L. & James, D. W. Ion-ion-solvent interactions in solution. Part 3.-Aqueous solutions of sodium nitrate. *Journal of the Chemical Society, Faraday Transactions 1: Physical Chemistry in Condensed Phases* **78**, 3223-3234, doi:10.1039/f19827803223 (1982).
120 Vol. E2834 (ASTM International, West Conshohocken, PA, 2012).
121 Wagner, T., Wiemann, M., Schmitz, I. & Lipinski, H. A cluster-based method for improving analysis of polydisperse particle size distributions obtained by nanoparticle tracking. *Journal of Nanoparticles* **2013**, doi:10.1155/2013/936150 (2013).

122 Michalet, X. Mean square displacement analysis of single-particle trajectories with localization error: Brownian motion in an isotropic medium. *Physical Review E* **82**, 041914 (2010).
123 Walker, J. G. Improved nano-particle tracking analysis. *Measurement Science and Technology* **23**, 065605 (2012).
124 Saveyn, H. *et al.* Accurate particle size distribution determination by nanoparticle tracking analysis based on 2-D Brownian dynamics simulation. *Journal of Colloid and Interface Science* **352**, 593-600, doi:10.1016/j.jcis.2010.09.006 (2010).
125 Murphy, D. B. & Davidson, M. W. in *Fundamentals of Light Microscopy and Electronic Imaging* 389-413 (John Wiley & Sons, Inc., 2012).
126 Abade, G. C., Cichocki, B., Ekiel-Jeżewska, M. L., Nägele, G. & Wajnryb, E. Rotational and translational self-diffusion in concentrated suspensions of permeable particles. *Journal of Chemical Physics* **134**, 244903, doi:10.1063/1.3604813 (2011).
127 Liu, G., Hou, Y., Zhang, G. & Craig, V. S. J. Inhibition of Bubble Coalescence by Electrolytes in Binary Mixtures of Dimethyl Sulfoxide and Propylene Carbonate. *Langmuir* **25**, 10495-10500, doi:10.1021/la901199h (2009).
128 Craig, V. S. J. Bubble coalescence and specific-ion effects. *Current Opinion in Colloid & Interface Science* **9**, 178-184, doi:10.1016/j.cocis.2004.06.002 (2004).
129 Aguilera, M. E., Ojeda, A., RondÓN, C. & LÓPez De Ramos, A. Effect of Electrolytes on Bubble Coalescence in Columns Observed with Visualization Techniques. *Annals of the New York Academy of Sciences* **972**, 242-246, doi:10.1111/j.1749-6632.2002.tb04579.x (2002).
130 Liendo, L. *Estudio de la coalescencia de burbujas en sistemas electroliticos*, Universidad Simón Bolívar, (1998).
131 Henry, C. L. & Craig, V. S. J. The Link between Ion Specific Bubble Coalescence and Hofmeister Effects Is the Partitioning of Ions within the Interface. *Langmuir* **26**, 6478-6483, doi:10.1021/la9039495 (2010).
132 Henry, C. L. & Craig, V. S. J. Inhibition of Bubble Coalescence by Osmolytes: Sucrose, Other Sugars, and Urea. *Langmuir* **25**, 11406-11412, doi:10.1021/la9015355 (2009).
133 Pashley, R. & Karaman, M. *Applied Colloid and Surface Chemistry*. (Wiley, 2005).
134 Bunkin, N. F. *et al.* Nanobubble clusters of dissolved gas in aqueous solutions of electrolyte. I. Experimental proof. *The Journal of Chemical Physics* **137**, -, doi:10.1063/1.4739528 (2012).
135 Ohgaki, K., Khanh, N. Q., Joden, Y., Tsuji, A. & Nakagawa, T. Physicochemical approach to nanobubble solutions. *Chemical Engineering Science* **65**, 1296-1300, doi:10.1016/j.ces.2009.10.003 (2010).
136 Sette, D. & Wanderlingh, F. Nucleation by Cosmic Rays in Ultrasonic Cavitation. *Physical Review* **125**, 409-417 (1962).
137 Mitsuhiro, M. & Kotaro, T. Nano bubble—Size dependence of surface tension and inside pressure. *Fluid Dynamics Research* **40**, 546 (2008).
138 Ljunggren, S. & Eriksson, J. C. The lifetime of a colloid-sized gas bubble in water and the cause of the hydrophobic attraction. *Colloids and Surfaces A:*

Physicochemical and Engineering Aspects **129–130**, 151-155, doi:10.1016/S0927-7757(97)00033-2 (1997).
139 Sedlák, M. Large-Scale Supramolecular Structure in Solutions of Low Molar Mass Compounds and Mixtures of Liquids: II. Kinetics of the Formation and Long-Time Stability. *The Journal of Physical Chemistry B* **110**, 4339-4345, doi:10.1021/jp056934x (2006).
140 Newell, A. & Moloney, J. *Nonlinear Optics*. (Westview Press, 2003).
141 Kurtz, S. K. & Perry, T. T. A Powder Technique for the Evaluation of Nonlinear Optical Materials. *Journal of Applied Physics* **39**, 3798-3813, doi:10.1063/1.1656857 (1968).
142 Terhune, R. W., Maker, P. D. & Savage, C. M. Measurements of Nonlinear Light Scattering. *Physical Review Letters* **14**, 681-684 (1965).
143 Maker, P. D. Spectral Broadening of Elastic Second-Harmonic Light Scattering in Liquids. *Physical Review A* **1**, 923-951 (1970).
144 Bridgman, P. W. *Proc. Amer. Acad. Arts & Sci.* **52**, 91-187 (1916).
145 Swaminathan, S., Craven, B. M. & McMullan, R. K. The crystal structure and molecular thermal motion of urea at 12, 60 and 123 K from neutron diffraction. *Acta Crystallographica Section B* **40**, 300-306, doi:doi:10.1107/S0108768184002135 (1984).
146 Ward, M. R., Botchway, S. W., Ward, A. D. & Alexander, A. J. Second-harmonic scattering in aqueous urea solutions: evidence for solute clusters? *Faraday Discussions* **167**, 441-454, doi:10.1039/c3fd00089c (2013).
147 Botchway, S. W., Parker, A. W., Bisby, R. H. & Crisostomo, A. G. Real-time cellular uptake of serotonin using fluorescence lifetime imaging with two-photon excitation. *Microscopy Research and Technique* **71**, 267-273, doi:10.1002/jemt.20548 (2008).
148 Maul, R., Preuss, M., Ortmann, F., Hannewald, K. & Bechstedt, F. Electronic Excitations of Glycine, Alanine, and Cysteine Conformers from First-Principles Calculations. *The Journal of Physical Chemistry A* **111**, 4370-4377, doi:10.1021/jp068294j (2007).
149 Clays, K. & Persoons, A. Hyper-Rayleigh scattering in solution. *Physical Review Letters* **66**, 2980-2983 (1991).
150 Cyvin, S. J., Rauch, J. E. & Decius, J. C. Theory of Hyper-Raman Effects (Nonlinear Inelastic Light Scattering): Selection Rules and Depolarization Ratios for the Second-Order Polarizability. *The Journal of Chemical Physics* **43**, 4083-4095, doi:10.1063/1.1696646 (1965).
151 Gubskaya, A. V. & Kusalik, P. G. The multipole polarizabilities and hyperpolarizabilities of the water molecule in liquid state: an ab initio study. *Molecular Physics* **99**, 1107-1120, doi:10.1080/00268970110041218 (2001).
152 Pluta, T. & Sadlej, A. J. Electric properties of urea and thiourea. *The Journal of Chemical Physics* **114**, 136-146, doi:10.1063/1.1328398 (2001).
153 Saleh, B. E. A. & Teich, M. C. *Fundamentals of Photonics*. (Wiley, 2007).
154 Wunderlich, S., Schürer, B., Sauerbeck, C., Peukert, W. & Peschel, U. Molecular Mie model for second harmonic generation and sum frequency generation. *Physical Review B* **84**, 235403 (2011).
155 Kim, E. *et al.* Second-Harmonic Generation of Single BaTiO3 Nanoparticles down to 22 nm Diameter. *ACS Nano* **7**, 5343-5349, doi:10.1021/nn401198g (2013).

156 Wu, K., Snijders, J. G. & Lin, C. Reinvestigation of Hydrogen Bond Effects on the Polarizability and Hyperpolarizability of Urea Molecular Clusters. *The Journal of Physical Chemistry B* **106**, 8954-8958, doi:10.1021/jp014181i (2002).
157 Jen, S.-H., Gonella, G. & Dai, H.-L. The Effect of Particle Size in Second Harmonic Generation from the Surface of Spherical Colloidal Particles. I: Experimental Observations†. *The Journal of Physical Chemistry A* **113**, 4758-4762, doi:10.1021/jp9009959 (2009).
158 Gosting, L. J. & Akeley, D. F. A Study of the Diffusion of Urea in Water at 25 °C with the Gouy Interference Method. *Journal of the American Chemical Society* **74**, 2058-2060, doi:10.1021/ja01128a060 (1952).
159 Hollis, D. B. Review of hyper-Rayleigh and second-harmonic scattering in minerals and other inorganic solids. *Amer. Mineral.* **73**, 701-706 (1988).

Appendix A: Details of IP model

From the modified classical model of nucleation (Equation 1.10), the critical radius of a cluster, the size where it becomes a nucleus, is given by[1]

$$r_c(E) = \frac{2\gamma}{A \ln S + aE^2} \tag{A1}$$

with $A = \rho_s RT/M$, where ρ_s is the density of the solid, R is the gas constant, T is absolute temperature, and M is the molar mass. The electric field (E) is related to the peak laser power density by the following equation

$$E = \sqrt{\frac{2j_{\text{peak}}}{c\varepsilon_0}} \tag{A2}$$

where c is the speed of light in vacuum and ε_0 is the permittivity of free space. The electrostatic contribution to the free energy profile to nucleation is given by

$$aE^2 = \frac{3j_{\text{peak}}\varepsilon_L}{c}\left(\frac{\varepsilon_S - \varepsilon_L}{\varepsilon_S + 2\varepsilon_L}\right) \tag{A3}$$

where ε_L is the permittivity of the liquid solvent (water) and ε_S is the permittivity of the solid. The modified classical model can be used to calculate the number of nuclei (N_{nuc}) produced in the sample volume irradiated by the laser for an aqueous solute.

$$N_{\text{nuc}} = N_{\text{molec}} \frac{3M}{4\pi N_A \rho_S} \frac{I_1}{I_2} \tag{A4}$$

where N_A is the Avogadro constant. The integrals I_1 and I_2 are given as follows:

$$I_1 = \int_{r_c(E)}^{r_c(0)} e^{-\beta \Delta G(r,0)}\, dr \tag{A5}$$

$$I_2 = \int_{0}^{r_c(0)} r^3\, e^{-\beta \Delta G(r,0)}\, dr \tag{A6}$$

where $\beta = 1/(k_B T)$, k_B is Boltzmann's constant, and $\Delta G(r, E)$ is given by Equation 1.10 (Section 1.4.5). N_{molec} is the number of potassium halide (KX = KCl or KBr) ion pairs in the volume illuminated by the laser (V, which is estimated by a simple ray-tracing procedure). Equation A4 can be re-written in terms of the mass fraction of solute, $w = m_{KX}/(m_{KX} + m_{H_2O})$, to give

$$N_{\text{nuc}} = \frac{3wV\rho_L}{4\pi\rho_S} \frac{I_1}{I_2} \tag{A7}$$

Equation A7 is evaluated by numerical integration of the integrals I_1 and I_2, using the physical parameters for KCl and KBr which are summarized in Table 2.2. We identify N_{nuc} as the model value of the Poisson parameter (λ). From the limits of the

integral in Equation A4, we see that $N_{\mathrm{nuc}} = 0$ at $E = j_{\mathrm{peak}} = 0$, so the model labilities (m) can be calculated as $m = N_{\mathrm{nuc}}/j_{\mathrm{peak}}$; the results of model calculations are given in Table 2.3 in the main text.

It can be shown that the model described here reproduces the expected linear dependence of N_{nuc} on peak laser power density as follows. The only dependence of N_{nuc} on E is contained entirely in integral I_1, since I_2 does not depend on E. To first order in E^2, the lower limit of the integral can be written

$$r_{\mathrm{c}}(E) \approx r_{\mathrm{c}}(0)\left[1 - \frac{aE^2}{A \ln S}\right] = r_c(0) - \delta r \tag{A8}$$

where $\delta r = 2\gamma a E^2/(A \ln S^2)$ (with $A \gg a$). For the integral I_1,

$$I_1 = \int_{r_{\mathrm{c}}(0)-\delta r}^{r_{\mathrm{c}}(0)} f(r)\ \mathrm{d}r = f(r)\delta r \tag{A9}$$

Then we have

$$N_{\mathrm{nuc}} = \frac{3w\mathrm{V}\rho_L}{4\pi\rho_S}\frac{\mathrm{e}^{-\beta\Delta G(r_{\mathrm{c}}(0),0)}}{I_2}\frac{2\gamma a E^2}{(A \ln S)^2} \propto E^2 \tag{A10}$$

The expression A10 shows that the value of $N_{\mathrm{nuc}} \propto E^2$, which is in turn directly proportional to j_{peak}.

Appendix B: Calculation of image spatial resolution

The resulting spatial resolution of the imaging system employed in Rayleigh laser scattering experiments was obtained by knowledge of the output video resolution (e.g., 720×576 pixels) and the dimensions of the recorded image.

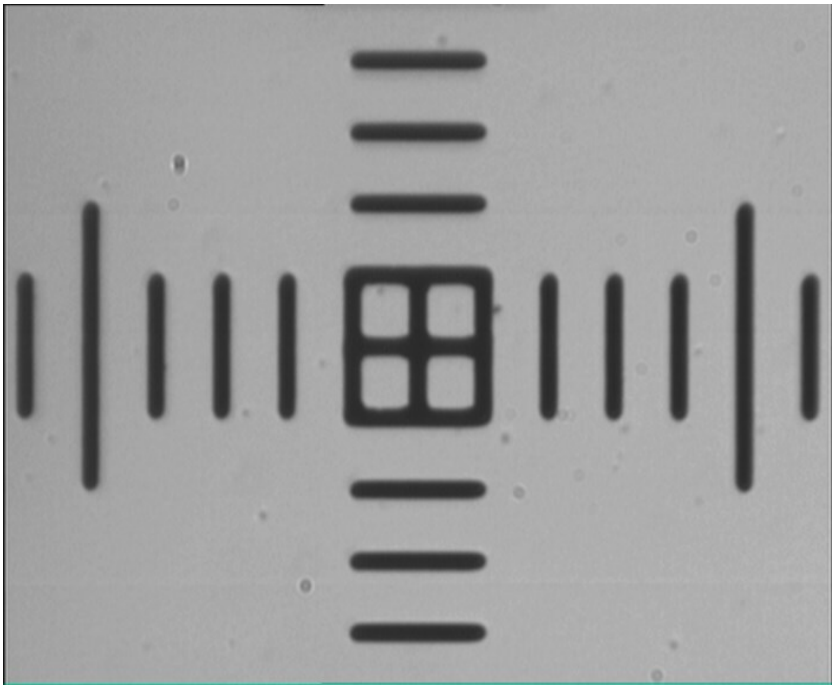

Figure B.1 Figure of the graticule (10 μm spacing) imaged using the ×50 objective (0.55 NA). The scale provides a horizontal length of 130.1 μm and therefore a spatial resolution of 181 nm pixel^{-1}.

The width of the image is obtained by comparison to the graticule spacing (10 μm), to give a width of 130 μm. The graticule image has a resolution of 720×576 pixels, therefore the spatial resolution is given by $130\ \mu\text{m}/720\ \text{pixels} = 181\ \text{nm pixel}^{-1}$. This process was carried out for all levels of magnification used during experiments; the spatial resolution achieved is shown in Table B.1.

Objective	Spatial resolution / nm pixel^{-1}
× 10	1029
× 50	181
× 100	89

Table B.1 Summary of the spatial resolution achieved for the different objectives used in Rayleigh laser scattering experiments.

Appendix C: Nanoparticle tracking analysis

C.1 Initialization

Particle tracking analysis was performed using the NanoTrackJ plugin for the ImageJ software package (http://imagej.nih.gov/ij/). The plugin requires an image stack for analysis (generated in ImageJ) using a series of individual images or a video file.

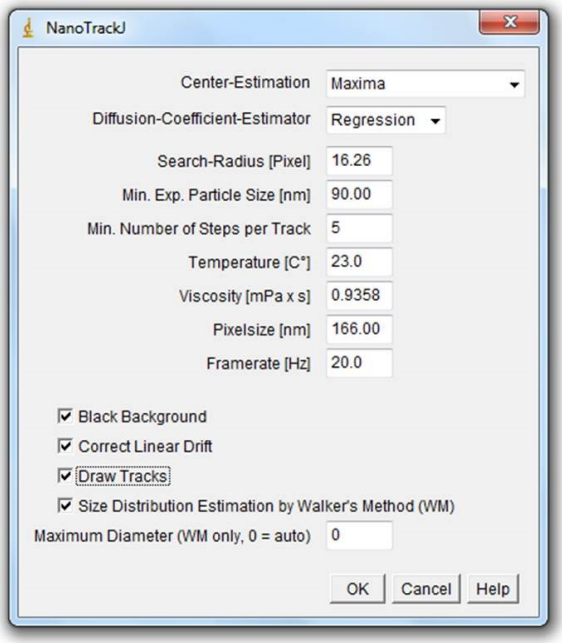

Figure C.1 Initialization screen shown during NanoTrackJ analysis of simulated data with particles of 100 nm diameter. The required parameters for analysis and those of experiment are input. The value of pixel size required in this window is that of the video image (spatial resolution), and not the physical pixel size of the CCD camera. The search radius is the maximum distance a particle could have travelled from its location in the previous frame to be tracked as the same particle. This value is updated automatically based on the expected particle size; however, it can also be adjusted manually.

The method of centre estimation used in this Thesis was the Maxima method which uses the in-built "*Find Maxima*" method on ImageJ. Similarly, the regression method was used to calculate diffusion coefficients. This method is most used in literature reports and evaluates the mean-squared-displacement for different time lags. A regression line is then fitted to the data points, the slope of which is proportional to the diffusion coefficient.

NanoTrackJ incorporates a "*Spot Assistant*" that helps the user to process the images appropriately using a mean filter size and tolerance level; the effect of the spot assistant values is visible in real time to the user.

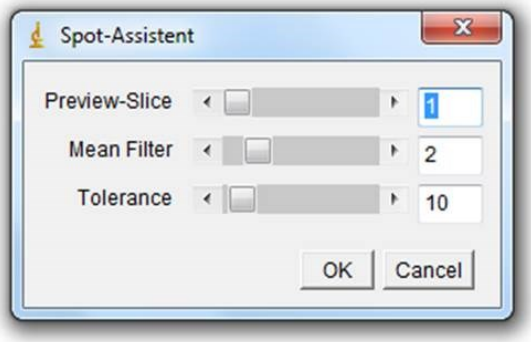

Figure C.2 Spot assistant window in NanoTrackJ. The tolerance value dictates an intensity threshold that can be varied to occlude background signals from the image and retain only those of particles. The mean filter value is modified to obtain the optimal image for analysis.

C.2 Results

After analysis has completed a histogram of the particle size distribution is displayed. In addition, results tables are also displayed to allow exporting of the tracking data to other graphing and analysis packages.

In this Thesis, peaks were identified manually and fitted using a non-linear, least-squares Gaussian peak fit to obtain the peak centre which was then later reported as the estimate of the mean particle diameter. A fit of the data shown in Figure C.3 is given in Figure C.4 where an estimate of 101.6 ± 0.2 nm diameter is obtained. The distributions provided by the particle tracking analysis are typically not symmetrical, however a Gaussian fitting scheme was employed to provide an estimate of the central point of the main peak. Especially in the case of the distributions obtained for sample solutions it is unclear if the tail of a given peak is due to a skewed distribution or to a number of smaller peaks. Therefore to provide an unbiased estimate of the central position of the main peak, fitting with a symmetrical function (Gaussian) was employed.

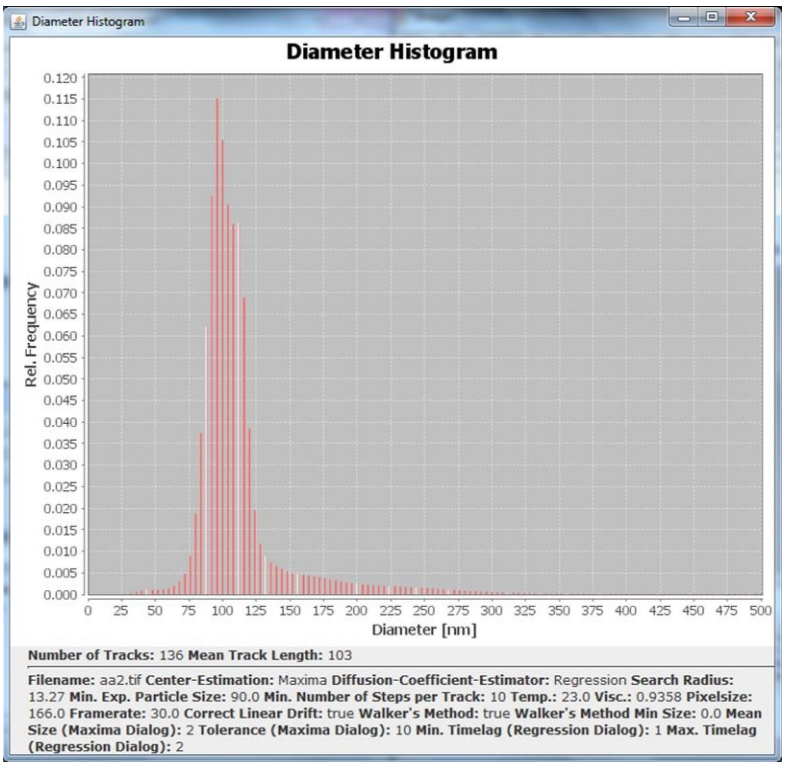

Figure C.3 Example results histogram of particle size distribution. Analysis was carried out on simulated data with particle size of 100 nm and the Walker method was employed. Details of the analysis are shown at the bottom of the histogram.

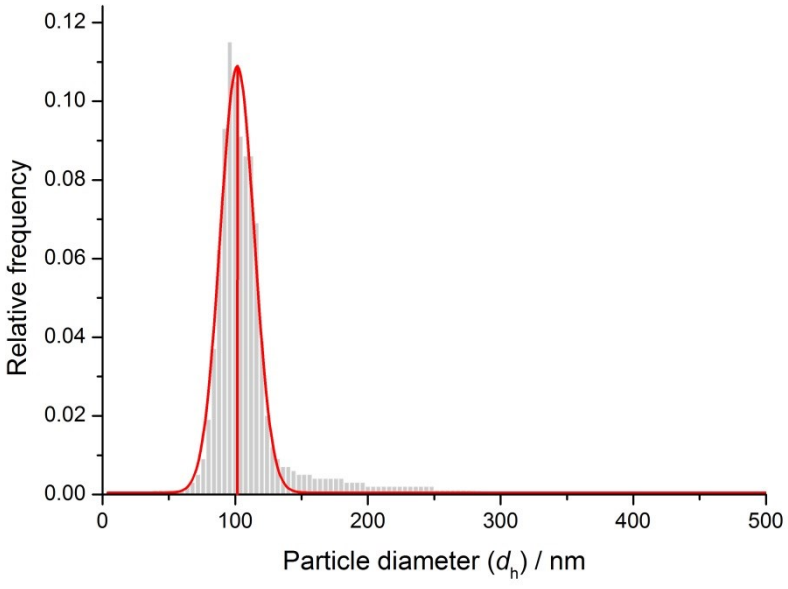

Figure C.4 Plot of the results data shown in Figure C.3. Data is fitted with a non-linear, least-squares Gaussian fit and an estimate of mean particle diameter $d_h = 101.6 \pm 0.2$ nm is obtained. The analysed data was that simulated to be 100 nm particles.